ACTIVE CONTROL OF PERIODIC NOISE

Proefschrift
ter verkrijging van de graad van doctor aan
de Technische Universiteit Delft,
op gezag van de Rector Magnificus,
prof. ir. K.F. Wakker,
in het openbaar te verdedigen ten overstaan van een commissie,
aangewezen door het College van Dekanen
op donderdag 2 december 1993 te 10.00 uur door

MICHIEL WILBERT ROMBOUT MARIA VAN OVERBEEK

geboren te Eindhoven

natuurkundig ingenieur

BIBLIOTHEEK TECHNISCHE UNIVERSITEIT
Prometheusplein 1
2628 ZC
DELFT

Gebotekst Zoetermeer / 1993

Dit proefschrift is goedgekeurd door de promotor

prof.dr.ir. A.J. Berkhout

Copyright © 1993, by TNO Institute of Applied Physics, Delft, The Netherlands.
All rights reserved. No part of this publication may be reproduced, stored in a retrieval system or transmitted in any form or by any means, electronic, mechanical, photocopying, recording or otherwise, without the prior written permission of the author, M.W.R.M. van Overbeek, TNO Industrial Research, TNO Institute of Applied Physics, P.O. Box 155, 2600 AD Delft, The Netherlands.

CIP-DATA KONINKLIJKE BIBLIOTHEEK, DEN HAAG
Overbeek, Michiel Wilbert Rombout Maria van

Active control of periodic noise / Michiel van Overbeek
[S.l. : s.n.] (Zoetermeer: Gebotekst)
Thesis Technische Universiteit Delft. – With ref.
ISBN 90–9006732–9
Subject headings: active noise control

cover design: H. van Ham

printed in The Netherlands by: N.K.B. Offset bv, Bleiswijk

Preface

The research described in this thesis has been carried out while I was working at the department of Acoustics of the Institute of Applied Physics of TNO (TPD-TNO), and the research is completely financed by TPD. Scientific support in writing the manuscript was given by prof.Berkhout and dr. Wapenaar of the Laboratory of Seismics and Acoustics of the Delft University of Technology.

Contents

1. INTRODUCTION

1.1 Active Noise Control

The elimination of acoustic noise with the aid of anti-noise is based on the principle of linear superposition of waves. This principle implies that at any point in a medium where several acoustic waves are present, the resultant acoustic pressure equals the sum of the pressures due to each wave individually. The consequence of this superposition principle is that the addition of two acoustic waves may result in a zero acoustic pressure (silence) at certain positions in the medium. Lord Rayleigh already observed these 'points of silence'. In 'The Theory of Sound' [1] he derives the geometrical position of the cancellation positions, given two sources having the same 'pitch' as he calls it. He notices that it is difficult to set up an experiment in which points of silence are realised and then writes:

'Perhaps the most satisfactory form of the experiment is that described in the Philosophical Magazine for June 1877 by myself.
"An intermittent electric current, obtained from a fork interrupter making 128 vibrations per second, excited by means of electro-magnets two other forks, whose frequency was 256. These latter forks were placed at a distance of about ten yards apart, and were provided with suitably tuned resonators, by which their sounds were reinforced. The pitch of the forks was necessarily identical, since the vibrations were forced by electromagnetic forces of absolutely the same period. With one ear closed it was found possible to define the places of silence with considerable accuracy, a motion of about an inch being sufficient to produce a marked revival of sound. At a point of silence, from which the line joining the forks subtended an angle of about 60^{o}, the apparent striking up of one fork, when the other was stopped, had a very peculiar effect".

If the acoustic pressure at a point of silence $\mathbf{x}_1 = (x_1, y_1, z_1)$ due to one of the forks equals $p_p(\mathbf{x}_1, t)$, then the resultant pressure at $\mathbf{x}_1$ is equal to zero if the second fork generates an acoustic pressure at $\mathbf{x}_1$ equal to

$$p_s(\mathbf{x}_1, t) = -p_p(\mathbf{x}_1, t).$$

This simple principle can be used to eliminate unwanted, primary noise emitted by machinery, exhausts or whatever sources: a loudspeaker sends out the 'anti-noise' and the result is silence. This way of reducing noise is called Active Noise Control (ANC) because the original, primary wave field is influenced actively. It is contrary to the passive ways to control noise for which mufflers, barriers and absorbing materials are used.
Effective active noise control is in practice not simple. There are three major problems in

reducing noise with anti-noise; they represent the three principal fields of research in ANC.

The first problem is an *acoustic* problem. Using anti-noise, the acoustic pressure is cancelled *locally* at one (or a few) positions in the *volume*. The primary wave field at other positions in the volume will be affected too, and there is no guarantee that the acoustic pressure will be reduced *globally*. At some positions the pressure may even increase.

In addition to the acoustic problem there is a *control* problem. The primary pressure $p_p(\mathbf{x}_1,t)$ is a *time function* and the secondary pressure $p_s(\mathbf{x}_1,t)$ due to the anti-noise source must have the same time dependency. Since the anti-noise signal has to be calculated before it can be fed to the anti-noise source, the controller must be able to predict $p_p(\mathbf{x}_1,t)$. In order to do so a controller model is needed which contains prior information. Furthermore, since the anti-noise source generally is not situated at the cancellation position $\mathbf{x}_1$, the acoustic transfer function between the source position and the location $\mathbf{x}_1$ must be taken into account.

Finally there is also the *hardware* problem: generally the complex control problem mentioned above cannot be solved with an analog controller; a control algorithm has to be executed real time on a digital computer. Since the computational effort can be considerable, the costs of the hardware can be so high that from an economic point of view it is not realistic to use ANC in noise abatement.

Recently hardware costs have come within an acceptable range for the simplest applications. At the moment ANC systems are commercially available for the reduction of the noise in ventilation ducts and the 'booming noise' in cars (second order engine harmonic).

This thesis comprises the results of a research on the first two problems: the acoustic problem and the control problem. It is the aim of the research to design complete active noise control systems to be used in practice. Therefore much attention is paid to laboratory experiments and the use of anti-noise in practical applications. The theoretical derivations in the chapters 2,3 and 4 are illustrated with the laboratory experiments and in the last chapter some results of active noise reduction in practice will be given.

1.2 The acoustics of anti-noise

1.2.1 The acoustic problem

The acoustic problem in ANC was stated in the previous section: local cancellation does not guarantee a global reduction. With the help of a simple example the acoustic problem can be illustrated. Assume there are two monopole sources, a primary source at $\mathbf{x}_p$ and a secondary source at $\mathbf{x}_s$ injecting mass into an unbounded three dimensional medium. The sources generate a spherical wave. The mass flux per unit time at $\mathbf{x}_p$ due to the source at $\mathbf{x}_p$ is represented by the source function $s_p(t)$ and the mass flux per unit time at $\mathbf{x}_s$ due

the to source at $\mathbf{x}_s$ is represented by the source function $s_s(t)$. The pressure amplitude at a location $\mathbf{x}$ due to a monopole is *inversely proportional* to the distance to the source while the time lag at $\mathbf{x}$ is *proportional* to this distance. At position $\mathbf{x}$ the distance to $\mathbf{x}_p$ is $r_p = |\mathbf{x} - \mathbf{x}_p|$ and the distance to $\mathbf{x}_s$ equals $r_s = |\mathbf{x} - \mathbf{x}_s|$. The total pressure at $\mathbf{x}$ due to the two spherical waves is

$$p(\mathbf{x},t) = \frac{s_p(t-\frac{r_p}{c})}{4\pi r_p} + \frac{s_s(t-\frac{r_s}{c})}{4\pi r_s}, \tag{1.1}$$

c being the propagation velocity of the acoustic waves.
Now assume a point of silence has to be realised at a pre-specified position $\mathbf{x}_1$. The 'retarded' secondary source function generating perfect anti-noise at $\mathbf{x}_1$ is

$$s_s(t-\frac{r_{s,1}}{c}) = -\frac{r_{s,1}}{r_{p,1}} s_p(t-\frac{r_{p,1}}{c}), \tag{1.2}$$

in which $r_{p,1} = |\mathbf{x}_1 - \mathbf{x}_p|$ and $r_{s,1} = |\mathbf{x}_1 - \mathbf{x}_s|$.
As a consequence the secondary source function is

$$s_s(t) = -\frac{r_{s,1}}{r_{p,1}} s_p(t-\frac{r_{p,1}}{c}+\frac{r_{s,1}}{c}). \tag{1.3}$$

Equation (1.3) shows that if there is no *prior* information available on the primary source function $s_p(t)$, anti-noise can only be realised if

$$r_{p,1} \geq r_{s,1}. \tag{1.4}$$

The local cancellation at $\mathbf{x}_1$ will have consequences for the wave field at other positions. It will be obvious that the cancellation is not global. There are however more positions $\mathbf{x}$ at which the primary pressure is cancelled if the secondary source function satisfies (1.3).
The difference in time-lag at the locations where the pressure is cancelled must be

$$\frac{1}{c}(r_p - r_s) = \frac{1}{c}(r_{p,1} - r_{s,1}). \tag{1.5}$$

In a geometric presentation all locations where the difference of the distances r_p and r_s is equal to $(r_{p,1} - r_{s,1})$ are found on a hyperboloid with focus points at $\mathbf{x}_p$ and $\mathbf{x}_s$.In figure 1.1 the hyperboloid is depicted for a situation in which (1.5) is fulfilled.

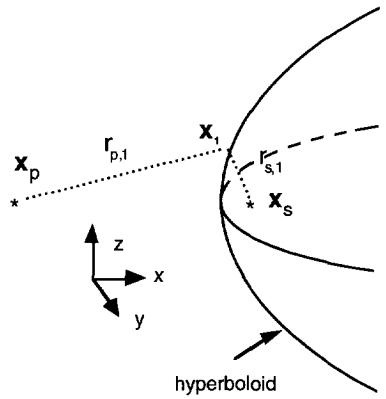

Figure 1.1 ; *The positions where the difference in distance to* $\mathbf{x}_p$ *and* $\mathbf{x}_s$ *is equal to* $(r_{p,1} - r_{s,1})$ *are found on a hyperboloid.*

Furthermore, on all cancellation positions the ratio of the primary pressure amplitude to the secondary pressure amplitude has to be

$$\frac{r_s}{r_p} = \frac{r_{s,1}}{r_{p,1}}. \tag{1.6}$$

In a geometric presentation the locations on which equation (1.6) holds are found on the sphere

$$|\mathbf{x} - \mathbf{x}_c|^2 = \frac{\alpha_1^2}{(1-\alpha_1^2)^2}|\mathbf{x}_s - \mathbf{x}_p|^2 = \frac{\alpha_1^2}{(1-\alpha_1^2)^2} r_{s,p}^2, \tag{1.7}$$

in which the amplitude ratio $\alpha_1 = \frac{r_{s,1}}{r_{p,1}}$. The centre $\mathbf{x}_c$ is given by

$$\mathbf{x}_c = \mathbf{x}_s + \frac{\alpha_1^2}{1-\alpha_1^2}(\mathbf{x}_s - \mathbf{x}_p). \tag{1.8}$$

Note that due to restriction (1.4) $\alpha_1 \leq 1$.
In figure 1.2 the sphere is shown ($\alpha_1 = 0.25$).

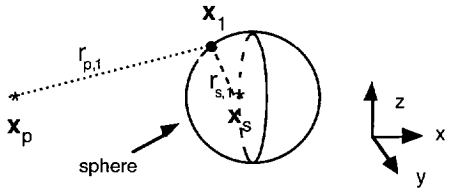

Figure 1.2 ; *The positions where the ratio of the distance to* $\mathbf{x}_s$ *and the distance to* $\mathbf{x}_p$ *is equal to* $\frac{r_{s,1}}{r_{p,1}}$ *are found on a sphere.*

The intersection of the hyperboloid and the sphere is a circle of positions $\mathbf{x}$ in a plane perpendicular to the line which connects the two sources. Note that if $r_{p,1} = r_{s,1}$ both the hyperboloid and the sphere degenerate to a plane halfway the two sources.
Now assume that the primary source function $s_p(t)$ is periodic with period T_0, than

$$s_p(t + nT_0) = s_p(t), \tag{1.9}$$

in which $n = -\infty, \ldots, -1, 0, 1, \ldots, \infty$, and the restriction (1.4) no longer holds. There are more possible values for the difference in time lag:

$$\frac{1}{c}(r_p - r_s) = \Delta t_{lag} + nT_0. \tag{1.10}$$

in which $\Delta t_{lag} = \frac{1}{c}(r_{p,1} - r_{s,1})$. So, there are more hyperboloids on which the difference in time lag is optimal for anti-noise and, as Lord Rayleigh [1] puts it,

"The intersections of this sphere with the system of hyperboloids will thus mark out in most cases several circles of absolute silence."

In figure 1.3 the intersections are drawn for periodic noise with a period $T_0 = \frac{1}{3}\Delta t_{lag}$, and an amplitude ratio $\alpha_1 = 0.25$. In addition to the circle through $\mathbf{x}_1$ there is one extra circle of cancellation positions.

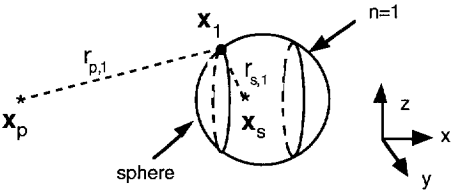

Figure 1.3 ; *A geometric presentation of anti-noise at* $\mathbf{x}_1$. *On the sphere equation (1.6) holds, on the circle also equation (1.5) is fulfilled. On the second circle equation (1.10) holds for* $n=1$.

Using the set-up depicted in figure 1.3, global cancellation is not possible. The acoustic pressure is only cancelled on a number of circles. However, the pressure at other positions is affected too. The total acoustic pressure is only reduced on locations where the sign of the primary acoustic pressure and the sign of the secondary acoustic pressure are opposite. The total wave field is amplified on positions where the primary wave field and the secondary wave field have the same sign. The maxima are found on positions where the two wave fields have the same *phase*. If $s_p(t)$ and $s_s(t)$ are sinusoidal time functions and the minima are given by (1.10), than the difference in time lag at maxima is

$$\frac{1}{c}\left(r_p - r_s\right) = \Delta t_{lag} + (n + \tfrac{1}{2})T_0.$$

The phase lag of a wave front at $\mathbf{x}$ is determined by the distance to the source but also depends on the frequency.
The acoustic pressure as a function of the frequency is found applying the Fourier transform on the acoustic pressure as a function of time. The Fourier transform performed on the total pressure (1.1) yields

$$P(\mathbf{x}, f) = P_p(\mathbf{x}, f) + P_s(\mathbf{x}, f), \tag{1.12}$$

where

$$P_p(\mathbf{x}, f) = S_p(f)\frac{\exp(-jkr_p)}{4\pi r_p},$$

and

$$P_s(\mathbf{x}, f) = S_s(f)\frac{\exp(-jkr_s)}{4\pi r_s}.$$

The wave number is $k = \frac{2\pi f}{c}$. The wave length is inversely proportional to the wave number: $\lambda = \frac{2\pi}{k}$. The functions $S_p(f)$ and $S_s(f)$ are the Fourier transforms of the primary and secondary source functions $s_p(t)$ and $s_s(t)$ respectively.
Assuming again that anti-noise is optimal at $\mathbf{x}_1$, the Fourier transform of the secondary source function is

$$S_s(f) = -\frac{r_{s,1}}{r_{p,1}} S_p(f) \exp\left(-jk(r_{p,1} - r_{s,1})\right). \tag{1.13}$$

The total pressure at an arbitrary position $\mathbf{x}$ is found substituting (1.13) in (1.12). The addition of the secondary wave field will give a minimum of zero acoustic pressure at the cancellation positions and a pattern of reduced and amplified acoustic pressures at other positions in space. The pattern of destructive and constructive interference strongly depends on the wave number. To give an impression of these interference patterns the

reduction of the primary pressure in the set-up illustrated in figure 1.3 is calculated in the plane y=0. The reduction of the primary pressure is given by the ratio of the primary wave field to the residual wave field (1.12) and is expressed in dB:

$$20\mathrm{Log}\frac{|P_p(\mathbf{x},f)|}{|P(\mathbf{x},f)|}.$$

In figure 1.4 the reduction is plotted. The primary source is situated at $\mathbf{x}_p = (0,0,0)$ and the secondary source at $\mathbf{x}_s = (1.5,0,0)$ (distances are in meters). In the figure the sources and the cancellation position are indicated and the intersection of the sphere (1.5) with the plane y=0 (a circle) is drawn with a solid line. In figure 1.4 the difference in the distances $r_{p,1} - r_{s,1} \approx 1\mathrm{m}.$, so the time lag $\Delta t_{lag} \approx \frac{1}{c}$ s.. Since the period $T_0 = \frac{1}{3}\Delta t_{lag}$, the wave length is $\lambda \approx \frac{1}{3}$ m.

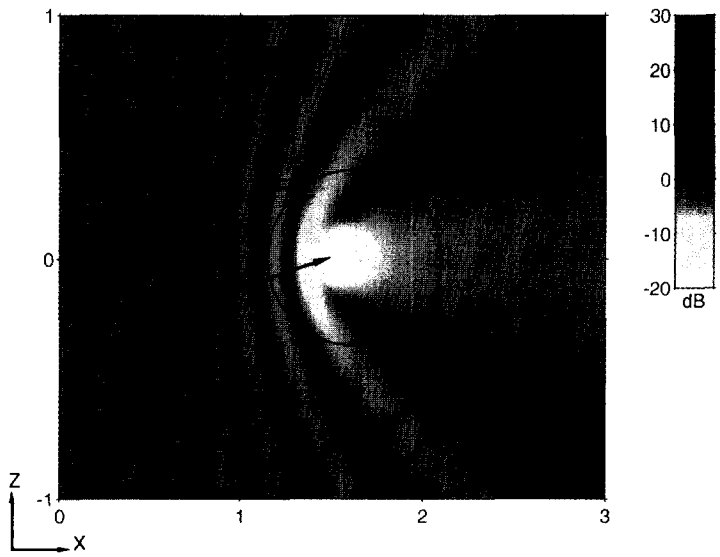

Figure 1.4 ; *The reduction in dB of the primary wave field in the plane y=0. The primary source is positioned at P, given by* $x_p = (0,0,0)$ *and the secondary source at S given by* $x_s = (1.5,0,0)$. *Note that the dark spots indicate the points of silence.*

The wave field is cancelled on the intersections of two hyperboloids and a sphere, giving in the plane z=0 two sets of points where the reduction is high. In figure 1.4 these points of silence are indicated with dark spots, the cancellation position $\mathbf{x}_1$ being one of them. The figure makes clear that, except for the area close to the secondary source, the interference pattern is determined by the hyperboloids, so by the difference between the

actual phase $k(r_p - r_s)$ and the proper phase for anti-noise $k(r_{p,1} - r_{s,1})$. Note that the wave field has a large amplitude near the anti-noise source where $\frac{1}{r_s}$ is small.

1.2.2 Anti-noise in the free field

From the foregoing it follows that global cancellation can take place if $\mathbf{x}_s = \mathbf{x}_p$. However, in practice it is not feasible to position an acoustic anti-noise source at exactly the noise source position. Theoretically it is possible to generate a secondary wave front in the propagation direction of the primary wave front with the help of sources somewhere else. The theory is based on the principle of Huygens, stating that each point of a wave front may be considered to be a secondary source generating a wave field in the propagation direction of the primary wave field. This principle implies that any wave front can be reproduced with the aid of a suitable distribution of sources. In order to fulfill the (spatial) Nyquist criterion the mutual source distance must be smaller than $\frac{1}{2}\lambda$.

Now assume that a number of secondary sources is placed on a part of the spherical wave front at some distance r_n of the primary source. The sources are volume sources all with the same amplitude and phase. The source strengths are chosen as to generate a spherical wave front at a distance r_{n+1} having the same amplitude as the primary wave front, generated by the primary source at $\mathbf{x}_p$. The phase of the secondary wave front however is shifted π radian. Destructive interference will take place and the amplitude of the resulting wave front in the propagation direction is smaller than the amplitude of the primary wave front. In figure 1.5 the primary and secondary wave front at a distance r_{n+1} from $\mathbf{x}_p$ are depicted.

Assuming that the secondary sources are able to reproduce the primary wave front exactly π radian out of phase in the indicated area, the pressure in this area at a distance $r \geq r_n$ from the primary source equals

$$\left|p_p(\mathbf{x},t) + p_s(\mathbf{x},t)\right| = 0, \tag{1.14}$$

for all t; $\mathbf{x}$ is a position within the indicated area at a distance r from the primary source. Equation (1.14) implies that the surface of secondary volume sources acts as a reflector with a pressure reflection coefficient -1.

The inward travelling wave field, opposite to the propagation direction, will be affected too. The interference is not destructive in this direction because the primary wave field and the anti-noise wave field have opposite propagation directions. In figure 1.5 the secondary wave front at a distance r_{n-1} is drawn as well.

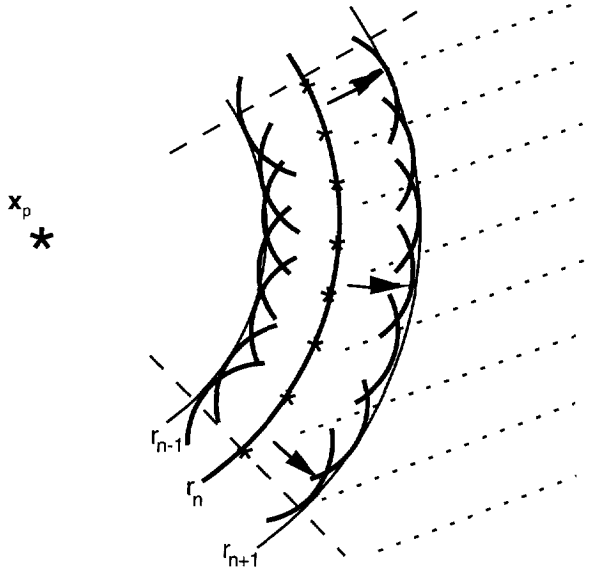

Figure 1.5 *; The superposition of the actual primary wave front and the anti noise wave front in the outward direction will result in a new wave front with a reduced amplitude. The propagation direction of the primary wave field is indicated with arrows.*

1.2.3 Anti-noise in an enclosed space, the one dimensional situation

In a one dimensional wave field the generation of a secondary wave front in the propagation direction of a primary wave front can be realised with one source. One dimensional wave fields are found for instance in ventilation ducts or exhausts. If a wave field is generated in a duct at frequencies below the cut-off frequency of the duct, the cross modes disappear resulting in plane waves propagating in the length direction of the duct. Similar to the derivations for spherical wave fields it can be derived that in an infinitely long duct where a primary source generates plane waves travelling in the positive x-direction, the acoustic pressure is cancelled 'downstream' while a standing wave pattern is formed 'upstream' (see figure 1.6).
In chapter 2 the acoustical implications of one dimensional anti-noise will be discussed. It will be shown that in the ideal situation the anti-noise source (a loudspeaker) also acts as a reflector having a pressure reflection coefficient equal to -1. In chapter 5 an example will be given for duct noise caused by a vacuum pump in a chemical plant.

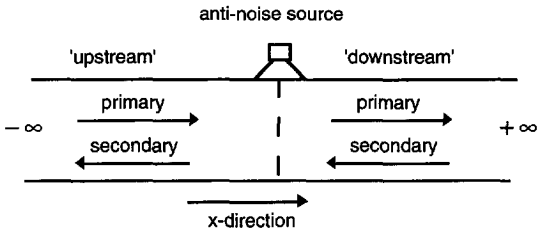

Figure 1.6 ; *The propagation directions of the primary and secondary plane waves in a one dimensional wave field.*

1.2.4 Anti-noise in an enclosed space, the three dimensional situation

If the primary source is placed in an enclosure, the wave field due to this source is not only determined by the outgoing spherical wave front, but also by the multiple reflections at the walls of the enclosure. In enclosures where there is only little damping these multiple reflections largely determine the wave field. In these circumstances it is more convenient to describe the wave field with the help of *eigenfunctions*. In case an acoustic wave field is analysed with eigenfunctions, it means that functions are chosen that describe the wave field at natural frequencies. The natural frequency itself is in that case the *eigenvalue*. The wave pattern at a natural frequency is usually called an eigenmode of the system. A mathematical proof can be given that not only the discrete states at the eigenvalues, but also the states in between two eigenvalues can be described with a weighted superposition of the complete set of eigenfunctions. In unbounded media the use of eigenfunctions does not have any practical meaning. In enclosed wave fields eigenfrequencies arise at frequencies which are linked with the dimensions of the enclosure. The wave field in a reverberant enclosure at a natural frequency is described with one eigenfunction, the wave field at frequencies between two natural frequencies can only be fully described with an infinite number of eigenfunctions. If the wave length of the wave field has the same order of magnitude as the dimensions of the enclosure, the number of eigenfrequencies per frequency interval *(modal density)* is small. At low modal densities the influence of eigenmodes with a high eigenfrequency is negligible and the wave field between two natural frequencies can be described accurately with a restricted number of eigenfunctions. The important implication for ANC is that it can be shown that a wave field, which can be described with N eigenmodes, can be cancelled in the whole enclosure with N properly positioned anti-noise sources [2].
In chapter 3 the acoustic implications of anti-noise for three dimensional wave fields with a small modal density will be discussed. In practical situations there is always some absorption at the boundaries of the enclosed wave field, so the derivations are more complicated than in a non absorbing enclosure. Using a few assumptions, a simple model can be applied which gives a clear insight in the possibilities of anti-noise in enclosures. In chapter 5 an example of the application of three dimensional anti-noise in a cabin of a

small truck (a delivery van) will be given.

1.3 Adaptive control in anti-noise

1.3.1 The control problem

In section 1.1 three aspects of the control problem were mentioned: the controller must have a *model* to calculate the anti-noise signal, the controller needs some *prior source information* and the controller has to take into account the (partly) acoustic *secondary process* between the controller output and the cancellation position. In figure 1.7 the anti-noise set-up is drawn.

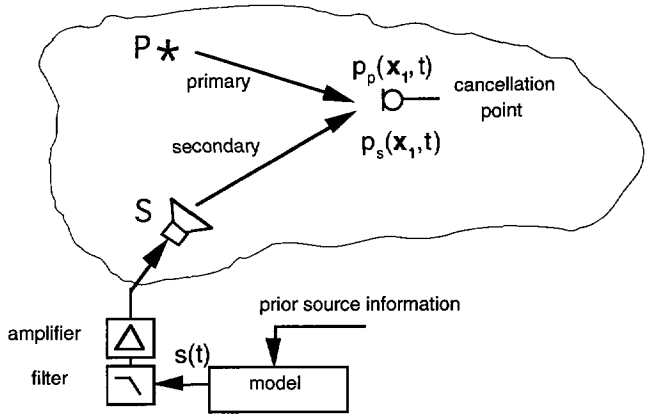

Figure 1.7 *; The typical control problem in ANC: the controller must have prior information on the primary pressure* $p_p(x_1,t)$ *and must know the transfer function between* s(t) *and* $p_s(x_1,t)$.

In this thesis only feed forward models are considered. In a feed forward model the input contains prior information of the primary pressure $p_p(x_1,t)$ at the cancellation position. The relation between the controller output signal $s(t)$ and the pressure $p_s(x_1,t)$ must be taken into account. It is defined by the transfer functions of the reconstruction filters, amplifiers and the acoustic environment. In chapter 4 the incorporation of the secondary process in ANC will be discussed.

1.3.2 The controller model

The controller model must be able to predict the primary pressure $p_p(x_1,t)$ at the cancellation position based on prior source information. For that situation the model describes the relation between the prior source information and the primary pressure. Note

that besides the modelling of the primary pressure $p_p(\mathbf{x}_1, t)$, the controller must take the secondary process into account. The parameters of the model are often the coefficients of a polynomial. However in case the primary noise is periodic, it is advantageous to use Fourier coefficients as controller parameters.

The most common way to collect the prior information is a sensor 'upstream'. This sensor gets information of the primary signal before it arrives at the cancellation position. In a feed forward configuration this sensor signal is used as an input of the controller. In the figures 1.8 and 1.9 two examples of a feed forward configuration are shown. In figure 1.8 the prior information is gathered using an 'upstream' detection microphone, measuring the incoming primary wave front. In this case the controller model comprises the transfer function between the position of the detection microphone and the cancellation point. The acoustic delay caused by the time it takes for the wave fronts to travel from this detection microphone to the cancellation position is used by the controller to calculate the anti-noise signal $s(t)$. The major complication of this method is the fact that generally the detection microphone will not only receive the primary wave front, but also the (delayed) secondary wave field and its reflections to the boundaries (the anti-noise feed back, see figure 1.8). The primary and secondary wave field are correlated, and instability problems are likely to occur. To overcome these complications a complex controller model is needed. Therefore this method is only used if there is no other possibility to get prior source information. It is applied for example in ANC systems for the reduction of stochastic fan noise in ventilation ducts.

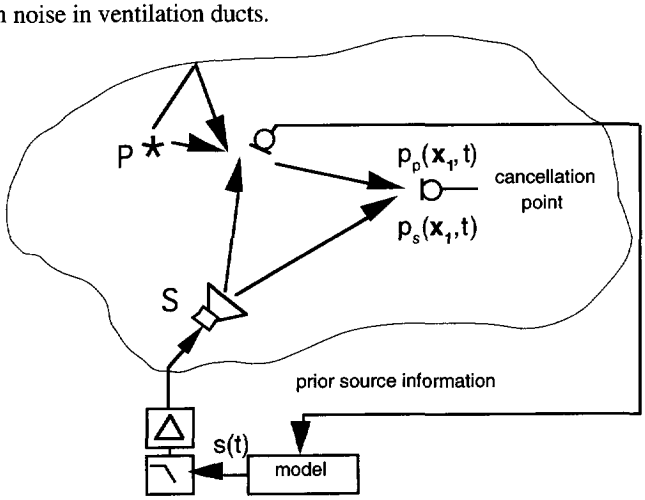

Figure 1.8 ; *Feed forward configuration for broadband noise.*

Especially in the case that the primary noise is excited by rotating machinery like the engine of a vehicle, there is a simple way to overcome anti-noise feed back. For rotating machinery the noise to be reduced is periodic and comprises the revolution frequency of the main shaft and a number of harmonics. Using a sensor mounted on the engine the

momentary revolution frequency (and of course the harmonics) are available and can serve as prior information. The model contains the relation between this sensor and the primary pressure at the cancellation position. It can be assumed that there is no anti-noise feed back on this sensor, and therefore a simple controller model suffices. In most cases this model only comprises the relation between the sensor and the primary pressure for the revolution frequency and a number of harmonics, and not the relation for broad band noise. Obviously the method can only be used to reduce the frequency components related to the revolution frequency of the engine. In figure 1.9 a feed forward configuration for rotating machinery is depicted.

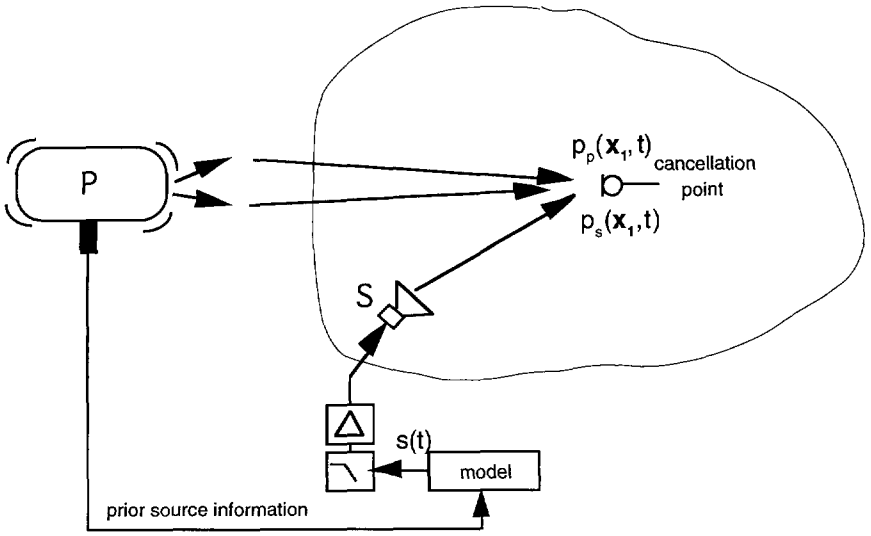

Figure 1.9 ; *Feed forward configuration for periodic noise.*

1.3.3 Adaptive control in a closed loop

In practical situations the controller model parameters and the secondary process are not known exactly. Furthermore, the signals and acoustic processes are time variant. For those reasons the controller must be adaptive: the controller must be able to adjust its parameters continuously to the optimal values. In order to do so the controller must have information on the performance, i.e. the residual noise level at the cancellation position. In the open loop feed forward configuration shown in the figures in the previous section the residual noise level is not available to the controller. In figure 1.10 the closed loop feed forward configuration for periodic noise is drawn. In this configuration the residual signal is incorporated. Obviously the residual signal in anti-noise is generally measured with a microphone.
In chapter 4 the use of adaptive control in ANC is discussed, and a comparison is made between a controller the parameters of which are the coefficients of a polynomial model and a controller the parameters of which are Fourier coefficients. Two types of 'Fourier'

controllers are discussed: the well known block oriented controller in which (fast) Fourier transforms are performed on blocks of data and a myopic controller in which the Fourier coefficients are updated sample by sample.
The two practical examples are described in chapter 5. Both have Fourier controllers: the duct noise caused by a pump is reduced with a one-dimensional block oriented Fourier controller and the interior noise in the delivery van is reduced with a multi dimensional myopic Fourier controller.

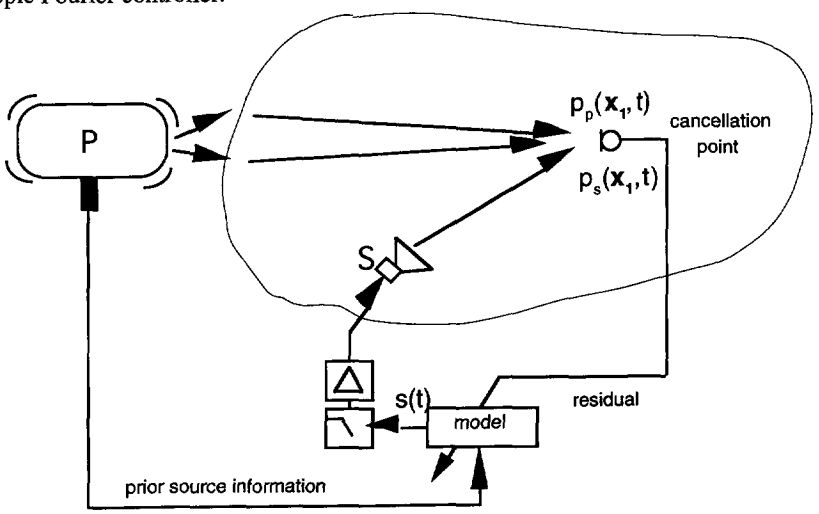

Figure 1.10 ; *The feed forward closed loop configuration for periodic noise.*

2 THE ACOUSTICS OF ANTI NOISE IN A ONE DIMENSIONAL SITUATION

Introduction

Active noise control (ANC) is based on two main theoretical fields: Acoustics and Adaptive minimization techniques. In this chapter the acoustics underlying anti noise will be reviewed and a one-dimensional system (a duct) will be considered. Theoretical implications will be illustrated with results of measurements in the laboratory.

2.1 The basic equations

2.1.1 The wave equation

The derivation of the acoustic wave equation is based on momentum conservation and mass conservation and is described extensively in literature, Berkhout [3] and Skudrzyk [4] for example. In the derivation resulting in the equations given in this section the following assumptions are made. Shear forces and viscosity are neglected. The basic equations of mass conservation and momentum conservation are linearized. The differential relation between the density and the pressure is taken to be linear (only the linear term of the Taylor series) and it is assumed that the adiabatic equation of state for a perfect gas may be used. The following symbols are used:
p is the acoustic pressure, it is a function of time t and position $\mathbf{x} = (x,y,z)$,
p_s is the static pressure, it is constant in time and position,
ρ_s is the static volume density of mass, it is constant in time and position,
$\vec{v} = (v_x\ v_y\ v_z)^T$ is the acoustic particle velocity (a vector),
q is the volume density of the injection rate and
$\vec{f} = (f_x\ f_y\ f_z)^T$ is the volume density of the external force (a vector).
The ratio of the specific heat at constant pressure and the specific heat at constant volume is $\kappa = \frac{c_p}{c_v}$.
The equation of momentum conservation is

$$\nabla p + \rho_s \frac{\partial \vec{v}}{\partial t} = \vec{f}, \qquad (2.1.1)$$

whereas the equation of mass conservation reads

$$\frac{1}{\kappa p_s}\frac{\partial p}{\partial t} + \nabla.\vec{v} = q. \qquad (2.1.2)$$

From these equations the wave equation is derived

$$\nabla^2 p - \frac{1}{c^2}\frac{\partial^2 p}{\partial t^2} = -\rho_s \frac{\partial q}{\partial t} + \nabla.\vec{f}, \qquad (2.1.3)$$

in which c^2 is the squared propagation velocity of the acoustic waves

$$c^2 = \frac{\kappa p_s}{\rho_s}.$$

With the help of the Fourier transformation the equations can be written in spectral components. In the following equations f is the frequency and the wave number k is defined as

$$k = \frac{2\pi f}{c}.$$

Replacing lower case symbols for quantities in the time domain by upper case symbols for quantities in the frequency domain, the equation of momentum conservation

$$\nabla P(\mathbf{x},f) + jk\rho_s c\vec{V}(\mathbf{x},f) = \vec{F}(\mathbf{x},f), \qquad (2.1.4)$$

and the equation of mass conservation

$$\nabla.\vec{V}(\mathbf{x},f) + \frac{jk}{\rho_s c}P(\mathbf{x},f) = Q(\mathbf{x},f), \qquad (2.1.5)$$

yield together the (inhomogeneous) Helmholtz equation

$$\nabla^2 P(\mathbf{x},f) + k^2 P(\mathbf{x},f) = -jk\rho_s c Q(\mathbf{x},f) + \nabla.\vec{F}(\mathbf{x},f). \qquad (2.1.6)$$

2.1.2 Boundary conditions

Since the equation (2.1.6) has to be solved in a bounded medium the boundary conditions must be known. The boundary conditions can be found if the conservation equations (2.1.4) and (2.1.5) are integrated from a point just left of the boundary to a point just right of the boundary (figure 2.1.1). The positions $\mathbf{x}_b^+$ and $\mathbf{x}_b^-$ around the boundary at $\mathbf{x}_b = (x_b, y, z)$ are defined as

$$\mathbf{x}_b^+ = (x_b^+, y, z) \quad \text{and} \quad \mathbf{x}_b^- = (x_b^-, y, z), \qquad (2.1.7)$$

in which

$$x_b^+ = \lim_{\Delta x \to 0}\left(x_b + \tfrac{1}{2}\Delta x\right) \quad \text{and} \quad x_b^- = \lim_{\Delta x \to 0}\left(x_b - \tfrac{1}{2}\Delta x\right). \qquad (2.1.8)$$

Integration of the x-component of momentum conservation gives the equation

$$\int_{x_b^-}^{x_b^+} \frac{\partial P(\mathbf{x},f)}{\partial x} dx + \int_{x_b^-}^{x_b^+} jk\rho_s c V_x(\mathbf{x},f) dx = \int_{x_b^-}^{x_b^+} F_x(\mathbf{x},f) dx, \qquad (2.1.9)$$

while integration of mass conservation yields

$$\int_{x_b^-}^{x_b^+} \frac{\partial V_x(\mathbf{x},f)}{\partial x} dx + \int_{x_b^-}^{x_b^+} \left[\frac{\partial V_y(\mathbf{x},f)}{\partial y} + \frac{\partial V_z(\mathbf{x},f)}{\partial z} \right] dx + \int_{x_b^-}^{x_b^+} \frac{jk}{\rho_s c} P(\mathbf{x},f) dx = \int_{x_b^-}^{x_b^+} Q(\mathbf{x},f) dx. \qquad (2.1.10)$$

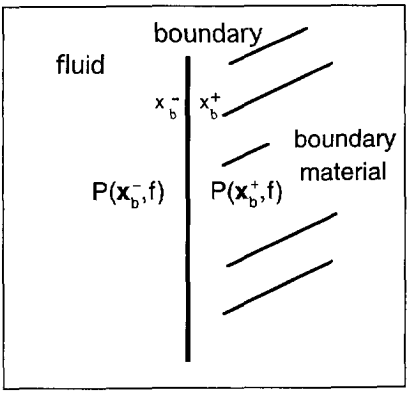

Figure 2.1.1 ; *The positions* $\mathbf{x}_b^+$ *and* $\mathbf{x}_b^-$ *around the boundary.*

Using (2.1.8), equation (2.1.9) reduces to

$$P(\mathbf{x}_b^+,f) - P(\mathbf{x}_b^-,f) = \int_{x_b^-}^{x_b^+} F_x(\mathbf{x},f) dx \qquad (2.1.11)$$

whereas equation (2.1.10) becomes

$$V_x(\mathbf{x}_b^+,f) - V_x(\mathbf{x}_b^-,f) = \int_{x_b^-}^{x_b^+} Q(\mathbf{x},f) dx. \qquad (2.1.12)$$

If there are no sources in the layer the boundary conditions simply are

$$\begin{aligned} P(\mathbf{x}_b^+,f) - P(\mathbf{x}_b^-,f) &= 0, \\ V_x(\mathbf{x}_b^+,f) - V_x(\mathbf{x}_b^-,f) &= 0. \end{aligned} \qquad (2.2.13)$$

Often the boundary conditions are expressed in terms off the normal specific acoustic impedance of the boundary material. The normal specific acoustic impedance is defined as the ratio between the normal velocity and the pressure, giving here

$$Z(\mathbf{x}_b^+,f) = \frac{P(\mathbf{x}_b^+,f)}{V_x(\mathbf{x}_b^+,f)} = \frac{P(\mathbf{x}_b^-,f)}{V_x(\mathbf{x}_b^-,f)}, \tag{2.1.14}$$

again assuming that there are no sources in the layer around $\mathbf{x}_b$.

2.1.3 The potential energy

The power flow of a wave field through a surface is:

$$w=\int_S p\vec{v}.\vec{n}dS, \tag{2.1.15}$$

in which the direction of $\vec{n}$ is perpendicular to the surface S. To find the power flow through a closed surface S, Green's first theorem and equations (2.1.1) and (2.1.2) are applied to a volume V, enclosed by a surface S (there are no sources inside V, appendix A, 2.1: Potential energy):

$$w=\oint_S p\vec{v}.\vec{n}dS = -\frac{\partial}{\partial t}\int_V\left[\frac{p^2}{2\rho_s c^2}+\frac{1}{2}\rho_s\vec{v}.\vec{v}\right]dV. \tag{2.1.16}$$

The net power flow (out of the volume) is equal to the decrease of potential and kinetic energy of the volume element. So the instantaneous potential energy density is

$$e_{pot} = \frac{p^2}{2\rho_s c^2}, \tag{2.1.17}$$

while the time averaged potential energy density equals

$$\tilde{e}_{pot} = \frac{1}{T}\int_0^T \frac{p^2}{2\rho_s c^2}dt. \tag{2.1.18}$$

For a periodic time function with period T this may be rewritten as (appendix A)

$$\tilde{e}_{pot} \approx \frac{\sum_{n=-\infty}^{+\infty}|P(\mathbf{x}_v,n\Delta f)|^2}{2\rho_s c^2 T^2}, \tag{2.1.19}$$

in which $\mathbf{x}_v$ is the position of the volume element and $\Delta f=\frac{1}{T}$, or

$$\tilde{e}_{pot} \approx \frac{\sum_{n=-\infty}^{+\infty} |P_n(\mathbf{x}_v)|^2}{2\rho_s c^2}, \qquad (2.1.20)$$

in which $P_n(\mathbf{x}_v) = \Delta f P(\mathbf{x}_v, n\Delta f)$ are the Fourier coefficients.

2.2 One dimensional situation

2.2.1 The extrapolation matrix

Consider a one dimensional wave field propagating in the x-direction like noise in a rigid walled duct at frequencies below the cutoff frequency (appendix A, 2.2). The conservation equations (2.1.4) and (2.1.5) for plane waves in the x-direction can be written in a compact form using a vector

$$\vec{B}(x,f) = \begin{pmatrix} P(x,f) \\ V_x(x,f) \end{pmatrix},$$

so

$$\frac{\partial \vec{B}(x,f)}{\partial x} = \mathbf{A}\vec{B}(x,f) + \vec{S}(x,f), \qquad (2.2.1)$$

in which $\mathbf{A} = \begin{pmatrix} 0 & -jk\rho_s c \\ \frac{-jk}{\rho_s c} & 0 \end{pmatrix}$ and $\vec{S}(x,f) = \begin{pmatrix} F_x(x,f) \\ Q(x,f) \end{pmatrix}$.

The derivation of the solution of the differential equation can be found in Wapenaar and Berkhout [5]. The solution is

$$\vec{B}(x,f) = \mathbf{M}(x - x_o, f)\vec{B}(x_o,f) + \int_{x_o}^{x} \mathbf{M}(x - x', f)\vec{S}(x',f)dx', \qquad (2.2.2)$$

where $\mathbf{M}(x - x_o, f)$ is the extrapolation matrix (appendix A, 2.2 extrapolation matrix)

$$\mathbf{M}(x - x_o, f) = \begin{bmatrix} \cos(k(x - x_o)) & -j\rho_s c \sin(k(x - x_o)) \\ \frac{-j}{\rho_s c}\sin(k(x - x_o)) & \cos(k(x - x_o)) \end{bmatrix}. \qquad (2.2.3)$$

The pressure and velocity at a position x in a one dimensional wave field can thus be found by extrapolating the pressure and velocity at a position x_0 and adding to it the wave field caused by the sources between the two positions.

2.2.2 Wave-field in a duct with a volume source

In figure 2.2.1 a one dimensional system with a source in the duct wall at position x_p is schematically drawn. The surface of the cross section of the duct is A_d. The length of the duct between the boundaries is L. A variable position in region I of the duct (figure 2.2.1) is denoted with x_I whereas a variable position in region II is denoted with x_{II}. The source is a small surface (A_s) moving with a velocity $V_s(f)$. The inner acoustic impedance of the surface is infinitely high. The volume injection rate of the source thus is

$$U_s(f) = A_s V_s(f).$$

There are no other sources present in the duct, so $F_x(x,f) = 0$ everywhere.
It is assumed that the volume injection rate density in a layer of thickness Δx at the position of the source ($x = x_p$ see figure 2.2.1) is uniform, so the particle velocity in the x-direction in the layer is

$$V_d(f) = \frac{U_s(f)}{A_d},$$

so

$$Q(x_p,f) = \frac{V_d(f)}{\Delta x}. \qquad (2.2.4)$$

Hence for $x_I < x_p < x_{II}$ and $k\Delta x << 1$

$$\int_{x_I}^{x_{II}} \mathbf{M}(x_{II} - x',f)\vec{S}(x',f)dx' \approx \mathbf{M}(x_{II} - x_p,f)\begin{pmatrix} 0 \\ V_d(f) \end{pmatrix}. \qquad (2.2.5)$$

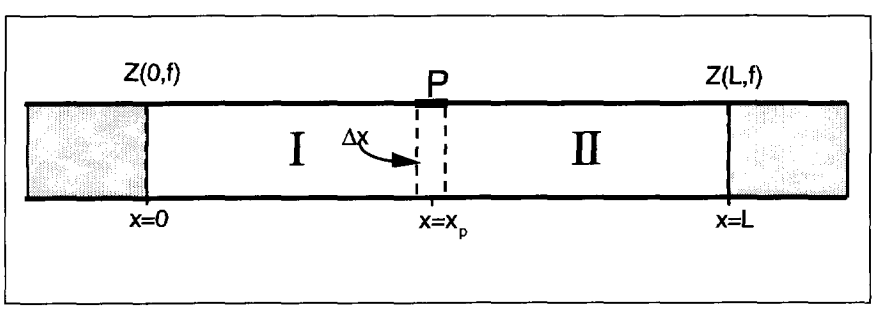

Figure 2.2.1 *A duct with a source at position and boundaries at x=0 and x=L*

The boundary conditions are determined by the boundary-material (and what is behind the material). The boundary conditions at x=0 and at x=L can be expressed in the specific acoustic impedance of the boundary material seen by a wave field in the fluid (figure 2.2.1). Without concerning about the actual values, we will assume that we know the

specific acoustic impedance at the boundaries at x=0 and x=L, so

$$\frac{P(0,f)}{V(0,f)} = Z(0,f) \quad \text{and} \quad \frac{P(L,f)}{V(L,f)} = Z(L,f). \tag{2.2.6}$$

The wave field in the duct is completely described with two vector equations and the boundary conditions. For the wave field at a position in region II the equations are

$$\vec{B}(x_{II},f) = \mathbf{M}(x_{II},f)\vec{B}(0,f) + \mathbf{M}(x_{II}-x_p,f)\begin{pmatrix} 0 \\ V_d(f) \end{pmatrix},$$

and (2.2.7)

$$\vec{B}(x_{II},f) = \mathbf{M}(x_{II}-L,f)\vec{B}(L,f).$$

Note that the acoustic pressure at the source position is continuous, whereas the acoustic particle velocity is not continuous:

$$\vec{B}(x_p^+,f) - \vec{B}(x_p^-,f) = \begin{pmatrix} 0 \\ V_d(f) \end{pmatrix} \quad \text{for} \quad x_p^+ - x_p^- \to 0.$$

Similar equations hold for the wave field in region I.
Often in a source free region of the one dimensional wave field the impedance transformation formula is used. It is found with the extrapolation matrix:

$$Z_{x_o}(x,f) = \frac{Z(x_o,f)\cos(k(x-x_o)) - j\rho_s c\sin(k(x-x_o))}{\cos(k(x-x_o)) - \frac{Z(x_o,f)}{j\rho_s c}\sin(k(x-x_o))}, \tag{2.2.8}$$

in which $Z_{x_o}(x,f)$ denotes the specific acoustic impedance at position x, extrapolated from x_0.

2.2.3 The power flow in the duct

In section 2.1 the power flow through a surface is given (equation (2.1.15)).
The time averaged power flow through a surface of cross section A_d is

$$w = \frac{A_d}{T}\int_0^T pv_x dt. \tag{2.2.9}$$

Similar to the potential energy (appendix A) this can be rewritten for a real periodic time function with period T to

$$w = \frac{2A_d}{T^2}\sum_{n=0}^{\infty} Re\left[P^*(x,n\Delta f)V(x,n\Delta f)\right]. \qquad (2.2.10)$$

Considering only frequency component $f=n\Delta f$, the time averaged power flow at a position x is found

$$W(x,f) = \frac{2A_d}{T^2} Re\left[P^*(x,f)V(x,f)\right]. \qquad (2.2.11)$$

With the help of the extrapolation equation (2.2.2) it can be derived that, if there are only volume sources present between x and x_o (appendix A,2.2 Power flow),

$$Re\left[P^*(x,f)V(x,f)\right] = Re\left[P^*(x_o,f)V(x_o,f)\right] + \int_{x_o}^{x} Re\left[P^*(x',f)Q(x',f)\right]dx', \qquad (2.2.12)$$

so, in the duct described in the previous section, the time averaged power flow is

$$W(x_I,f) = \frac{2A_d}{T^2} Re\left[P^*(x_{II},f)V(x_{II},f)\right] + \frac{2A_s}{T^2} Re\left[P^*(x_p,f)V_s(f)\right], \qquad (2.2.13)$$

or, using Fourier coefficients

$$W_n(x_I) = 2A_d Re\left[P_n^*(x_{II})V_n(x_{II})\right] + 2A_s Re\left[P_n^*(x_p)V_{s,n}\right], \qquad (2.2.14)$$

for $x_I < x_p < x_{II}$. Obviously, if there are no sources between x_I and x_{II}

$$W(x_I,f) = W(x_{II},f).$$

2.3 Anti noise in the duct

2.3.1 The experimental set-up

In this section the wave field in a duct in anti noise conditions will be derived. The theoretical derivations will be illustrated with the results of experiments.
There are two volume sources in the duct: a primary source P at position x_p having a volume velocity $U_{ps}(f) = A_d V_{pd}(f)$ (see equation 2.2.4) and a secondary source S at position x_s having a volume velocity $U_{ss}(f) = A_d V_{sd}(f)$ (figure 2.3.1). A variable position in region I of the duct is denoted with x_I, a variable position in region II is denoted with x_{II} and a variable position in region III is denoted with x_{III}.
The objective is to minimize the potential energy in a part (or region) of the duct. This is

done by minimizing the quadratic pressure on a sensor at position M (the error sensor) by adapting the source strength of S. As a result the potential energy in the duct regions will change (and not necessarily decrease).
The (complex) impedances at the boundaries are $Z(0,f)$ and $Z(L,f)$.
In the experiments a circular duct is used with a diameter of 0.15 meter and a signal frequency of 240 Hz, this is well below the cutoff frequency of the first higher order cross mode (approximately 1100 Hz). The total length of the duct is 3.53 m, in figure 2.3.1 the duct is schematically drawn. The primary source position x_p is 0.62 m., the secondary source position x_s is 2.91 m.. The left and right termination of the duct were closed with damping material. The Standing Wave Ratio (SWR, the ratio of the maximum pressure to that of the minimum pressure) due to the reflection at one of the boundaries is approximately 2 (in decibels : 6 dB). The anti noise source signal is computed with help of an active noise controller for periodic noise ('HADAP UNIT'). The adaptive algorithm used in the controller minimizes the quadratic pressure measured by a so called *error* sensor at position x_m. The adaptive algorithm will be discussed in chapter 3. The pressure in the duct was measured with an array of microphones with a spacing of 0.1 m. The pressure sensor which is part of the ANC system is also part of the measurement array. The microphones were placed through holes in the duct wall to avoid excessive wiring inside the duct.

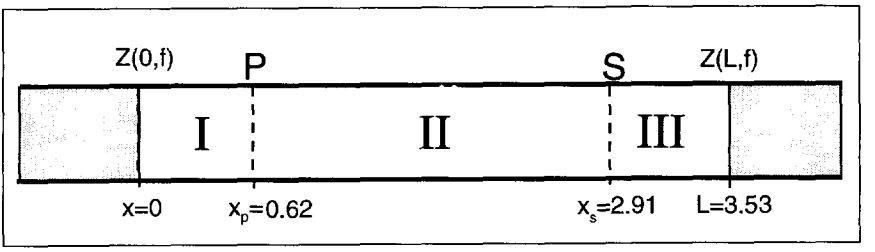

Figure 2.3.1 ; *The three regions and the two sources in ANC*

2.3.2 Anti noise downstream the secondary source: $\mathbf{x_m}$ *in region III*

The anti noise condition in region III is $P(x_{III},f)=0$, which implies that $V(x_{III},f)=0$, since the SWR is not infinite.
Hence, the wave field in the duct during anti noise can be described with

$$\begin{pmatrix} P(x_{III},f) \\ V_x(x_{III},f) \end{pmatrix} = \vec{0} = \mathbf{M}(x_{III}-x,f)\vec{B}(x,f) + \int_x^{x_{III}} \mathbf{M}(x_{III}-x',f)\vec{S}(x',f)dx' \quad (2.3.1)$$

Since the boundary condition at $x=0$ is known, the source strength of the anti noise source (or secondary source) related to the source strength of the noise source (or primary source) can be found with the impedance extrapolation formula and

$$\begin{pmatrix} P(x_{III},f) \\ V_x(x_{III},f) \end{pmatrix} = \vec{0} = \mathbf{M}(x_{III},f)\vec{B}(0,f) +$$
$$+ \mathbf{M}(x_{III}-x_p,f)\begin{pmatrix} 0 \\ V_{pd}(f) \end{pmatrix} + \mathbf{M}(x_{III}-x_s,f)\begin{pmatrix} 0 \\ V_{sd}(f) \end{pmatrix} \qquad (2.3.2)$$

This equation can be solved simply if both sides are multiplied with $\mathbf{M}(x_p - x_{III},f)$, and then rearranging the equation to

$$-\mathbf{M}(x_p,f)\vec{B}(0,f) = \begin{pmatrix} 0 \\ V_{pd}(f) \end{pmatrix} + \mathbf{M}(x_p - x_s,f)\begin{pmatrix} 0 \\ V_{sd}(f) \end{pmatrix}. \qquad (2.3.3)$$

The relation between the velocities of the sources is

$$U_s(f) = -\frac{U_p(f)}{\cos(k(x_p - x_s)) + \frac{j\rho_s c}{Z_0(x_p^-,f)}\sin(k(x_p - x_s))}. \qquad (2.3.4)$$

The acoustic pressure in region III, and so the acoustic pressure at the secondary source position is zero. As a consequence there is no power flow in region II and III (see equation 2.2.11), and no acoustic energy is generated or absorbed by the secondary source. During anti noise the secondary source acts as an acoustic reflector with a pressure reflection coefficient of -1.
Furthermore the standing wave ratio (SWR) in region II will be infinite.
The wave field in region II is determined by

$$\vec{B}(x_{II},f) = -\mathbf{M}(x_{II} - x_s,f)\begin{pmatrix} 0 \\ V_{sd}(f) \end{pmatrix}. \qquad (2.3.5)$$

An interesting situation arises if $\sin(k(x_p - x_s)) = 0$, and so $P(x_p,f) = 0$.
In this case neither of the sources radiates energy into the duct, the amplitudes of the volume velocities of the sources are equal and there is only a standing wave between the sources.
The cancelation of the sound pressure in region III can have a negative as well as a positive effect on the power radiated by the primary source.
In an experiment the set up as described above is used (see figure 2.3.1). The error sensor is placed in region III at x_{III}=3.32 m.. In the figures the amplitude of the pressure (SPL) has been drawn as a function of the position x in the duct. Three wave fields are depicted : the primary wave field ($U_s(f) = 0$), the secondary wave field ($U_p(f) = 0$) and the total wave field during ANC.
In figure 2.3.2 the pressure amplitude of the primary wave field (solid line) and the

pressure amplitude of the secondary wave field (dashed line) as *measured* by the microphones are plotted in one figure. The secondary wave field is the acoustic field the secondary source radiates during the generation of anti noise. This pressure can be measured by computing first the anti noise (or secondary) signal which cancels the primary noise on the error microphone (we need the primary field for this) and then switch off the primary noise without further adapting the anti noise signal.
The frequency is 240 Hz, so the wavelength is 1.43 m.. There is a shift of the interference pattern in the solid line at the primary source and in the dotted line at the secondary source. Because of the damping at the duct terminations the ratio of the maximum pressure amplitude to the minimum pressure amplitude (Standing Wave Ratio) is not very large (in decibels: approximately 6 dB).

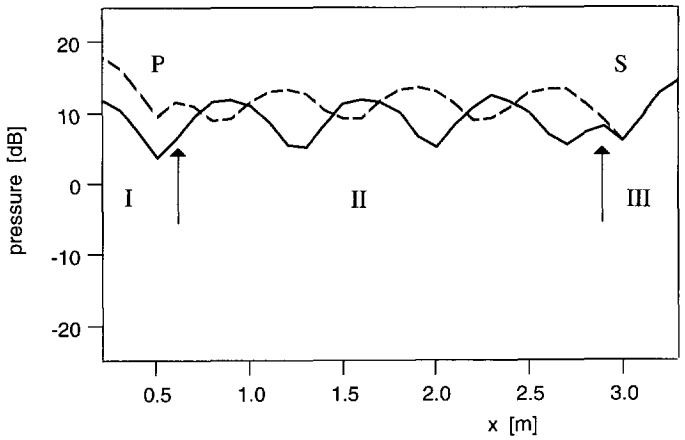

Figure 2.3.2 ; *The pressure amplitude of the primary wave field (solid line) and of the secondary wave field (dashed line).*

In figure 2.3.3 the sum of the total acoustic fields is depicted: it is the actual pressure amplitude *measured* in the duct during the generation of anti noise. In region III the pressure amplitude is almost zero. Due to the near field of the loudspeaker the pressure drop at the secondary source is not very sharp.
The standing wave ratio in region II, between the two sources is approximately 20 dB, so it has increased considerably compared to the SWR in figure 2.3.2.

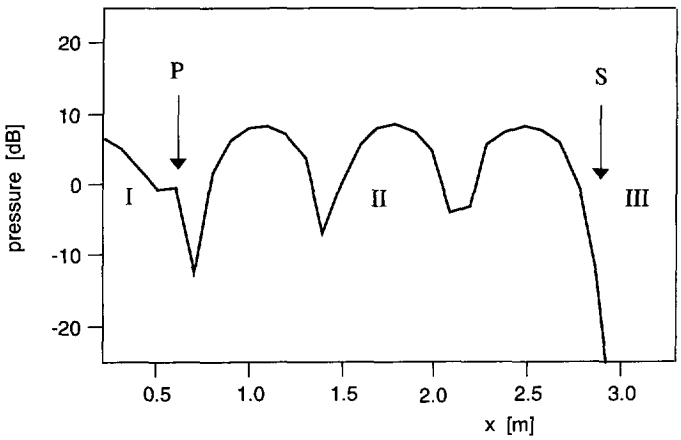

Figure 2.3.3 ; *The amplitude of the total pressure during anti noise in region III.*

2.3.3 Anti noise between the sources : $\mathbf{x_m}$ *in region II*

The anti noise condition in region II is $P(x_{II},f)=0$. However, this does not imply that $V(x_{II},f)=0$, since there is a source between x_{II} and the boundary. Hence, the wave field in the duct during anti noise is described with

$$\vec{B}(x,f) = \mathbf{M}(x-x_{II},f)\begin{pmatrix}0\\V(x_{II},f)\end{pmatrix} + \int_{x_{II}}^{x}\mathbf{M}(x-x',f)\vec{S}(x',f)dx'. \qquad (2.3.6)$$

The relation between the source strength of the secondary source and the source strength of the primary source can only be found using two vector equations (besides the boundary conditions (2.2.6)). For convenience they are written in the form

$$\mathbf{M}(x_p-x_{II},f)\begin{pmatrix}0\\V(x_{II},f)\end{pmatrix} = \mathbf{M}(x_p,f)\vec{B}(0,f) + \begin{pmatrix}0\\V_{pd}(f)\end{pmatrix}, \qquad (2.3.7)$$

and

$$\mathbf{M}(x_p-x_{II},f)\begin{pmatrix}0\\V(x_{II},f)\end{pmatrix} = \mathbf{M}(x_p-L,f)\vec{B}(L,f) - \mathbf{M}(x_p-x_s,f)\begin{pmatrix}0\\V_{sd}(f)\end{pmatrix}. \qquad (2.3.8)$$

With the help of the impedance extrapolation the following relation is found

$$U_s(f) = +\frac{\alpha U_p(f)}{\cos(k(x_p-x_s))+\frac{j\rho_s c}{Z_L(x_p^+,f)}\sin(k(x_p-x_s))}, \qquad (2.3.9)$$

in which $\alpha = \dfrac{\cos\left(k(x_p - x_{II})\right) + \dfrac{j\rho_s c}{Z_L(x_p^+, f)}\sin\left(k(x_p - x_{II})\right)}{\cos\left(k(x_p - x_{II})\right) + \dfrac{j\rho_s c}{Z_0(x_p^-, f)}\sin\left(k(x_p - x_{II})\right)}$.

The reduction of the pressure at a sensor position in region II will cause a standing wave between the sources. In the nodes the pressure is zero, and there is no power flow in region II. As a consequence the Standing Wave Ratio in region II during anti noise will be infinite.

In an experiment the error sensor is placed in section II at x_{II}=0.81 m..

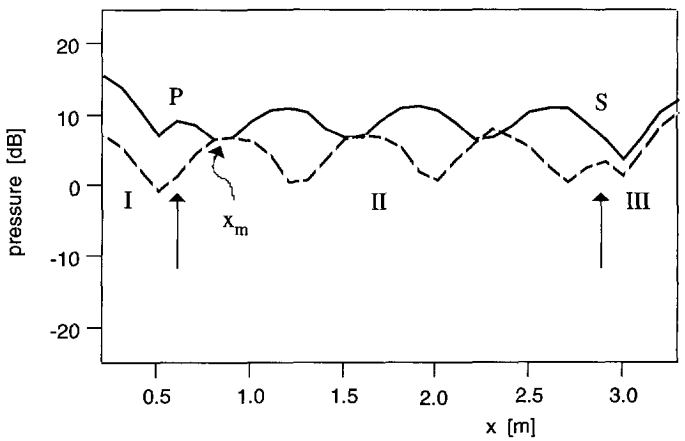

Figure 2.3.4 ; *The pressure amplitude of the primary wave field (solid line) and of the secondary wave field (dashed line)*

In figure 2.3.4 the pressure amplitude of the wave field due to the primary source ($U_s(f) = 0$, solid line) and the pressure amplitude of the wave field due to the secondary source ($U_p(f) = 0$, dashed line) are plotted in one figure.

In figure 2.3.5 the pressure amplitude during anti noise is plotted. There is an extreme pressure minimum at the position of the error sensor. The standing wave ratio is large compared to the primary and secondary wave field, as expected.

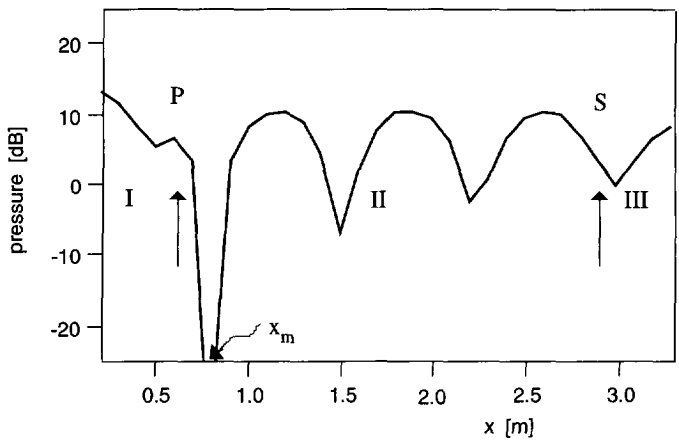

Figure 2.3.5 ; *The amplitude of the total wave field during anti noise in region II (sensor position x=0.81 m.)*

2.3.4 Anti noise 'upstream'

If the controller microphone is placed in region I, to the left of the primary source, the anti noise system is called 'up-stream' .
The anti noise condition in region I is $P(x_I,f) = 0$, which implies again that $V(x_I,f) = 0$.
So the wave field can be described with:

$$\vec{B}(x,f) = \int_{x_I}^{x} \mathbf{M}(x-x',f)\vec{S}(x',f)dx'. \qquad (2.3.10)$$

The relation between the source volume velocities during anti noise in region I is

$$U_s(f) = -U_p(f)\left(\cos(k(x_s-x_p)) + \frac{j\rho_s c}{Z_L(x_s^+,f)}\sin(k(x_s-x_p))\right). \qquad (2.3.11)$$

The pressure in region I and so the pressure at the primary source is zero, which means that the primary source does not generate or absorb energy during anti noise in region I. As a consequence there is no power flow in region I and II and the SWR is infinite.

Again the wave fields are measured. The error sensor is placed in section I near the left termination of the duct (x_I=0.2 m.).

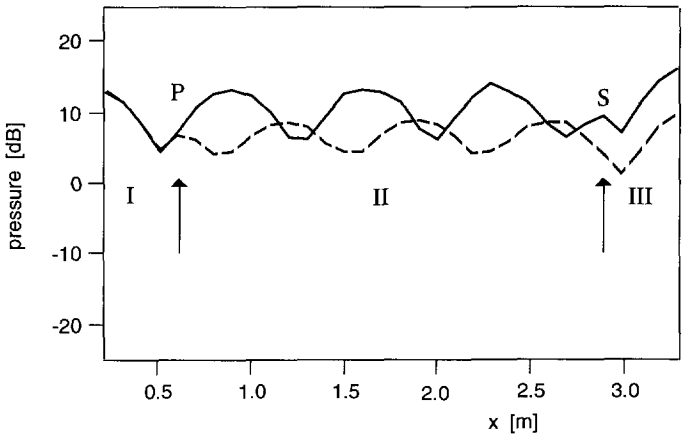

Figure 2.3.6 ; *The pressure amplitude of the primary wave field (solid line) and of the secondary wave field (dashed line).*

In figure 2.3.6 the pressure amplitude of the primary wave field ($U_s(f) = 0$, solid line) and the pressure amplitude of the secondary wave field ($U_p(f) = 0$, dashed line) as measured by the microphones are plotted in one figure.

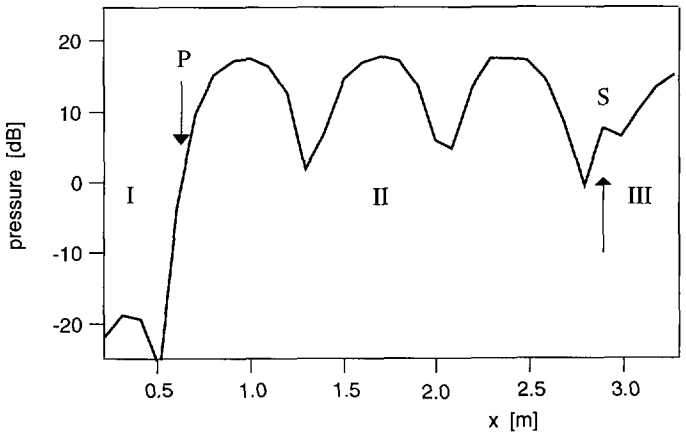

Figure 2.3.7 ; *The amplitude of the total wave field during anti noise in region I.*

In figure 2.3.7 the pressure amplitude *measured* in the duct during the generation of anti noise is depicted. Left of the primary loudspeaker the pressure-level is very low, although there is some influence of the near field of the primary loudspeaker. The SWR in region II is rather large.

2.4 Conclusions

The acoustic pressure and the particle velocity in a multi-source, one-dimensional situation can be found elegantly with the help of the so-called extrapolation matrix (equation 2.2.2, [5]). This equation is very effective to quantify the pressure and the particle velocity in a duct in which anti noise is generated. Derivations and measurements show that with the assumption of perfect anti noise there is no power flow between the (monopole) noise source and (monopole) anti noise source. Furthermore, with the assumption of perfect anti noise, in the 'downstream' configuration the acoustic impedance at the secondary source is zero whereas in the 'upstream' configuration the acoustic impedance at the primary source is zero. This means that in the 'downstream' configuration the secondary source and in the 'upstream' configuration the primary source act as an acoustic reflector having a pressure reflection coefficient of -1.

3 THE ACOUSTICS OF ANTI NOISE IN A THREE DIMENSIONAL SITUATION

Introduction

From a practical point of view active reduction of noise in a three dimensional wave field is much more complicated than active reduction in a one dimensional field. Reflection of a primary wave field by creating a zero impedance, as in a duct, can only be realised using a plane filled with sources having a mutual distance small compared to the wavelength. Furthermore, if we want to isolate a noise source in space, it must be surrounded by a closed surface of sources. In an enclosure however, the sound pressure can be reduced considerably without reflecting the wave field or isolating the noise source if the modal density is low. At low modal densities the wave field is largely determined by only a few eigenmodes. This means that the (opposite) acoustic field generated by the noise source can be reconstructed with a (small) number of anti-noise sources, even if the position of the noise source is unknown. As a consequence the potential energy is not brought to zero but minimized. In most applications the objective is to minimize the *global* potential energy. However, in some applications the pressure level in parts of the enclosure is of no concern and it can be advantageous to minimize the potential energy locally.
A clear review of the mechanisms of anti noise in enclosures at low modal densities can be given by describing the wave field due to a number of sources as a weighed superposition of the eigenfunctions (the eigenmodes) of the enclosure. The description of a (standing) wave field as a superposition of eigenmodes is developed by Morse [6] and is worked out by Nelson c.s. [7-9]. A simple set of eigenfunctions will be used here since the objective is not to describe exactly the wave field in a complicated enclosure, but to make clear why ANC can work in an enclosure at low modal densities.
The theoretical derivations will be illustrated with results of experiments performed in a small enclosure: a box of compressed wood having dimensions 1.00 m. x 0.85 m. x 0.33 m.. The rigid walls of this enclosure have a pressure reflection coefficient close to one. Small loudspeakers excite the wave field which is measured with the help of many microphones.

3.1 The acoustic pressure as a superposition of eigenfunctions

3.1.1 The Greens function in an enclosure

The wave field in an enclosure is largely determined by its (inner) form and dimensions, the boundary conditions, the medium and its non-homogeneities and the acoustic sources present in the enclosure. In most applications the form is irregular, the boundary conditions are complicated and there are many sources. As a consequence the wave field is difficult to model. However, to understand the mechanisms of anti noise in an

enclosure at low modal densities it is not necessary to compute the exact acoustic pressure in a complicated enclosure. Insight in the possibilities of anti noise in enclosures can be given using a model, based on the superposition of eigenfunctions. The medium in this model is considered to be homogeneous, and the sources present have a high internal impedance and there are no external sources.
The three dimensional wave equation is derived in section 2.1.1.:

$$\nabla^2 P(\mathbf{x},f) + k^2 P(\mathbf{x},f) = -jk\rho_s c Q(\mathbf{x},f). \tag{3.1.1}$$

The solution of an inhomogeneous Helmholtz equation can be derived in several ways. For reasons mentioned above the solution is derived assuming that a wave field in an enclosure can be described by a weighed superposition of eigenfunctions: a multiplication of a weighing coefficient depending on the frequency and an eigenfunction depending on the position:

$$P(\mathbf{x},f) = \sum_{n=1}^{\infty} a_n(f)\Psi_n(\mathbf{x}). \tag{3.1.2}$$

In general the wave field may be interpreted as a weighed superposition of a finite number of eigenfunctions rather than a superposition of an infinite number of weighed eigenfunctions. A set of eigenfunctions

$$\Psi_n(\mathbf{x}), \tag{3.1.3}$$

is chosen having the following properties:

$\Psi_n(\mathbf{x})$ satisfies the homogeneous three dimensional Helmholtz equation

$$\nabla^2\Psi_n(\mathbf{x}) + k_n^2\Psi_n(\mathbf{x}) = 0, \tag{3.1.4}$$

and the homogeneous boundary condition

$$\frac{\partial \Psi_n(\mathbf{x}_b)}{\partial n_b} + j\omega\rho_o\beta(\mathbf{x}_b)\Psi_n(\mathbf{x}_b) = 0, \tag{3.1.5}$$

in which n_b is the direction perpendicular into the boundary.
The real part of the *eigenvalue*

$$k_n = (2\pi f_n + j\delta_n)/c,$$

determines the eigenfrequency f_n belonging to it whereas the imaginary part, determined by the modal damping δ_n, stands for the absorption.

Note that $\beta(\mathbf{x}_b)$ does not depend on the order of the eigenfunction n which means that the normal acoustic impedance at the wall, defined as

$$Z_{n_b}(\mathbf{x}_b,f)=\frac{P(\mathbf{x}_b,f)}{V_{n_b}(\mathbf{x}_b,f)}, \tag{3.1.6}$$

does not depend on the frequency.
Since $\beta(\mathbf{x}_b)$ does not depend on the eigenfunction number n the following relation holds (appendix B)

$$\int_{V_{enclosure}}\Psi_n(\mathbf{x})\Psi_m(\mathbf{x})dV=0 \quad \text{if } n\neq m. \tag{3.1.7}$$

The equations (3.1.4) and (3.1.5) applied to an enclosure with given dimensions and boundary conditions yield the chosen eigenfunctions of this enclosure up to an arbitrary (complex) factor. Often the arbitrary factor is chosen so that

$$\int_{V_{enclosure}}\Psi_n(\mathbf{x})\Psi_m(\mathbf{x})dV=1 \quad \text{if } n=m, \tag{3.1.8}$$

yielding *normalized* eigenfunctions.
In the following derivations only normalized eigenfunctions will be used.
The combination of the equations (3.1.1), (3.1.2) and (3.1.4) yields

$$\sum_{n=0}^{\infty}a_n(f)\left(k^2-k_n^2\right)\Psi_n(\mathbf{x})=-jk\rho_s cQ(\mathbf{x},f). \tag{3.1.9}$$

In order to compute a coefficient $a_n(f)$, both sides of equation (3.1.9) are multiplied by $\Psi_m(\mathbf{x})$, and the result is integrated over the volume V of the enclosure giving

$$a_n(f)=\frac{-jk\rho_s c}{\left(k^2-k_n^2\right)}\int_{V_{source}}Q(\mathbf{x},f)\Psi_n(\mathbf{x})dV, \tag{3.1.10}$$

in which (3.1.7) and (3.1.8) have been used.
A simple unit source with a high inner impedance (volume source) at position $\mathbf{x}_l=(x_l,y_l,z_l)$ has a source strength:

$$Q(\mathbf{x}_l,f)=\delta(x-x_l)\delta(y-y_l)\delta(z-z_l). \tag{3.1.11}$$

Using (3.1.2) and (3.1.10), the sound pressure at a position $\mathbf{x}_m=(x_m,y_m,z_m)$ due to a simple source at $\mathbf{x}_l$ can be found. It is called the Greens function of the enclosure:

$$G(\mathbf{x}_m,\mathbf{x}_l,f)=\sum_{n=0}^{\infty}\frac{-jk\rho_s c}{\left(k^2-k_n^2\right)}\Psi_n(\mathbf{x}_l)\Psi_n(\mathbf{x}_m). \qquad (3.1.12)$$

In the following derivations we assume that the sources are velocity sources, having an infinitely high impedance. Consider a source mounted in a wall. The wall is situated in a y-z plane at $x=x_b$. The source has a uniform surface velocity $V_s(f)$ in the x-direction. The source strength is

$$Q(\mathbf{x},f) = V_x(y,z,f)\delta(x-x_b), \qquad (3.1.13)$$

while

$V_x(y,z,f) = V_s(f)$ on the source surface

and

$V_x(y,z,f) = 0$ elsewhere.

The acoustic pressure at a position $\mathbf{x}_m = (x_m, y_m, z_m)$ due to this source can be written as a superposition of the eigenfunctions with the help of (3.1.2) and (3.1.10). Using Green's function (3.1.12) the pressure is:

$$P(\mathbf{x}_m,f) = V_s(f)\int_{S_{source}} G(\mathbf{x}_m,\mathbf{x}_b,f)dydz. \qquad (3.1.14)$$

and $\mathbf{x}_b = (x_b, y, z)$.

As a consequence, the frequency response from the l^{th} velocity source having a uniform surface velocity $V_s(f)$ to a position $\mathbf{x}_m$ is

$$\frac{P(\mathbf{x}_m,f)}{V_s(f)} = H_{m,l}(f) = \int_{S_{source\,l}} G(\mathbf{x}_m,\mathbf{x}_b,f)dydz. \qquad (3.1.15)$$

3.1.2 A simple set of eigenfunctions

An eigenfunction of an enclosure actually describes a standing wave field at an the eigenfrequency. Considering a wave field to be a superposition of plane waves propagating through the enclosure and reflecting on its walls, the wavelength has to 'fit' into the enclosure to create a standing wave (appendix B). The wave number connected to this wavelength (the eigenvalue) strongly depends on the inner form of the enclosure and the boundary conditions. In enclosures having an irregular form, complicated boundary conditions and non-homogeneities, the eigenfunctions and eigenvalues are difficult to find. However, in a rectangular enclosure with rigid walls a very simple set of (normalized) eigenfunctions can be found using the homogeneous Helmholtz equation. The solution of the homogeneous wave equation is derived using a plane wave decomposition and an orthogonal basis (x, y and z) parallel to the walls of the box

(appendix B):

$$\Psi_n(\mathbf{x}) = \sqrt{\varepsilon_{n_x}\varepsilon_{n_y}\varepsilon_{n_z} / V_{enclosure}}\,.\cos(k_{n_x}x)\cos(k_{n_y}y)\cos(k_{n_z}z), \qquad (3.1.16)$$

where in an enclosure with dimensions L_x, L_y, L_z

$$k_{n_x} = \frac{n_x\pi}{L_x}, \qquad k_{n_y} = \frac{n_y\pi}{L_y} \quad \text{and} \quad k_{n_z} = \frac{n_z\pi}{L_z}, \qquad (3.1.17)$$

in which $n_x = 0,1\ldots\infty$, $n_y = 0,1\ldots\infty$ and $n_z = 0,1\ldots\infty$, and
$\varepsilon_{n_x}=1$ if $n_x = 0$ and $\varepsilon_{n_x}=2$ if $n_x > 0$ (and likewise for ε_{n_y} and ε_{n_z}).
The wave number of eigenfunction n (the eigenvalue) is

$$k_n = \sqrt{k_{n_x}^2 + k_{n_y}^2 + k_{n_y}^2}\,. \qquad (3.1.18)$$

The eigenfunctions given by (3.1.16) have a simple form. To illustrate one, the eigenfunction for which $n_x = 1$, $n_y = 1$ and $n_z = 0$ is given by

$$\Psi_{1,1,0}(\mathbf{x}) = \sqrt{4/V_e}\cos(\frac{\pi}{L_x}x)\cos(\frac{\pi}{L_y}y),$$

is plotted in figure 3.1.1 for a rectangular enclosure.

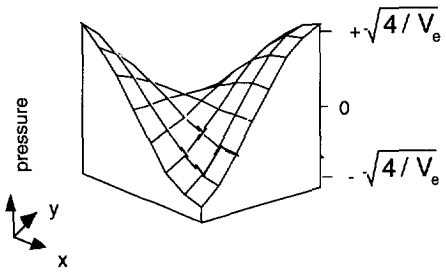

Figure 3.1.1 ; *The eigenfunction of the 1-1-0 mode on a linear scale.*

Obviously, since the eigenfunctions are real in this standing wave field, there exist only a positive and a negative phase (phase difference 180°). The phase distribution of the first six eigenfunctions in the rectangular enclosure of dimensions 1.00 m x 0.85 m x 0.33 m is depicted in figure 3.1.2.

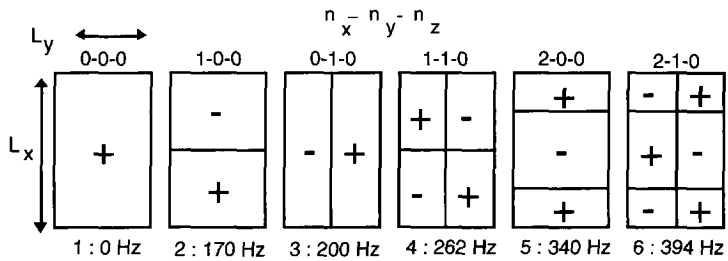

Figure 3.1.2 ; *The phase of the first six eigenfunctions in a rectangular box.*

3.1.3 The number of dominant eigenmodes

The number of eigenmodes that completely determines the wave field is infinite. However, not all eigenmodes contribute to the wave field to the same extent. In general the wave field in an enclosure may be interpreted as a superposition of a limited number of eigenmodes rather than a superposition of an infinite number of eigenmodes. So, using the coefficient-vector $\vec{a}(f) = [a_1(f) \quad \ldots \quad a_N(f)]^T$, and the eigenfunction-vector $\vec{\Psi}(\mathbf{x}) = [\Psi_1(\mathbf{x}) \quad \ldots \quad \Psi_N(\mathbf{x})]^T$, the acoustic pressure (3.1.2) can be written in a vector notation as

$$P(\mathbf{x}, f) \approx \vec{a}(f)^T \vec{\Psi}(\mathbf{x}). \tag{3.1.19}$$

The Green's function (3.1.12) can be written in a matrix notation using a diagonal matrix $\mathbf{A}(f)$ having elements

$$A_{nm}(f) = \begin{cases} \dfrac{-jk\rho_s c}{(k^2 - k_n^2)} & n = m \\ 0 & n \neq m \end{cases}, \tag{3.1.20}$$

yielding

$$G(\mathbf{x}_m, \mathbf{x}_l, f) \approx \vec{\Psi}(\mathbf{x}_m)^T \mathbf{A}(f) \vec{\Psi}(\mathbf{x}_l). \tag{3.1.21}$$

The elements of the matrix $\mathbf{A}(f)$ determine the amplitudes of the eigenmodes and depend on the frequency. Whether eigenmode n is important to the Green's function or not depends on the eigenfunction n at the source- and sensor position.
The eigenmodes contributing substantially to the wave field are called the *dominant* eigenmodes. Considering equation (3.1.20) it will be clear that the number of dominant eigenfunctions strongly depends on the denominator values and so on the excitation frequency. If a source in the enclosure excites a wave field at a frequency near to an eigenfrequency the amplitude of this eigenmode will be large compared to the other eigenmode-amplitudes. As a result the wave field is largely determined by this

eigenmode. Note that the first eigenfunction at $k_1 = 0$ is

$$\Psi_1(\mathbf{x}) = \sqrt{1/V_{enclosure}}.$$

At very low frequencies the first eigenmode is the only dominant eigenmode, and as a consequence the acoustic pressure of the wave field will be close to uniform, as the influence of the other eigenmodes is small.
At excitation frequencies between the eigenfrequencies more eigenmodes contribute substantially to the wave field. In that case the number of dominant eigenmodes strongly depends on the modal density. The modal density is defined as the number of eigenvalues per frequency-interval and can be made visual considering the three dimensional eigenvalue-space (appendix B). The number of dominant eigenmodes strongly increases if the modal density increases.
To give an impression of the influence of the excitation frequency on the number of dominant eigenmodes, the modal amplitudes of the diagonal matrix (3.1.21) of the rectangular enclosure (dimensions 1.00 m x 0.85 m. x 0.33 m.) have been calculated and are depicted for six different eigenfrequencies. In the six figures along the vertical-axis the logarithms of the modal amplitudes are plotted at a position on the horizontal axis which matches with the eigenfrequency.
In figure 3.1.3 the amplitudes are plotted for an excitation frequency of 266 Hz, which is close to the fourth eigenfrequency of 263 Hz. The fourth eigenmode clearly dominates the wave field and is more than 10 times larger compared to the adjacent eigenmode amplitudes. At the excitation frequency of 282 Hz in figure 3.1.4 the amplitude of this eigenmode has diminished, so the relative influence of the adjacent eigenmodes is larger.
At 300 Hz, depicted in figure 3.1.5, the domination of the fourth eigenmode has nearly disappeared and several eigenmodes determine the wave field. In figure 3.1.6 the modal amplitudes at an excitation frequency of 318 Hz are shown. The amplitude of the fifth eigenmode is larger here while at 336 Hz, close to the fifth eigenfrequency of 340 Hz, it dominates the wave field. This is plotted in figure 3.1.7. In the figure 3.1.8 the fifth eigenmode has diminished again.
In the measurements which will be discussed in the next section all sensors are placed in a x-y plane (at z=0.025 m.). The wave field in a plane at $z=z_0$ is determined by the eigenfunctions

$$\Psi_n(\mathbf{x}) = \cos(k_{n_x} x)\cos(k_{n_y} y)\cos(k_{n_z} z_o) \qquad (3.1.22)$$

With the help of the sensors, placed in the x-y plane, the $n_x - n_y - n_z$ mode cannot be distinguished from the $n_x - n_y - 0$ mode. Therefore, the wave field in the x-y plane is described with an alternative set of eigenmode coefficients in which each $n_x - n_y - n_z$ mode (n_x and n_y fixed) is added to the $n_x - n_y - 0$ mode. This new set of amplitudes for an excitation frequency of 300 Hz is also calculated and it is depicted in figure 3.1.10. next to the global set of eigenmodes which are plotted again in figure 3.1.9.

The calculated modal amplitudes in a rectangular enclosure.

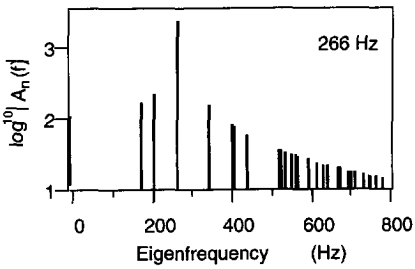

Figure 3.1.3 ; *266 Hz*

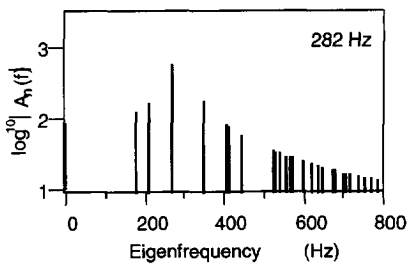

Figure 3.1.4 ; *282 Hz*

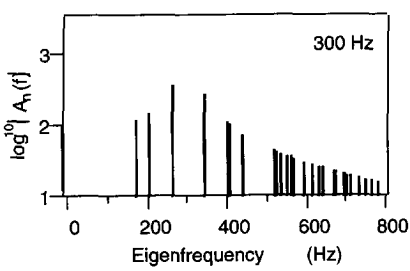

Figure 3.1.5 ; *300 Hz*

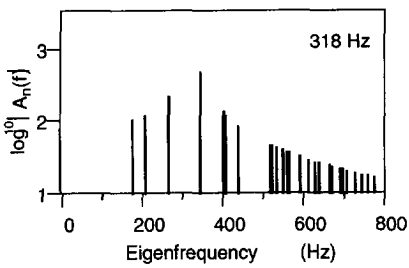

Figure 3.1.6 ; *318 Hz*

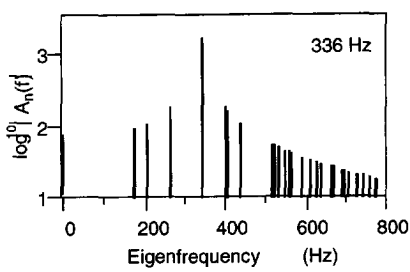

Figure 3.1.7 ; *336Hz*

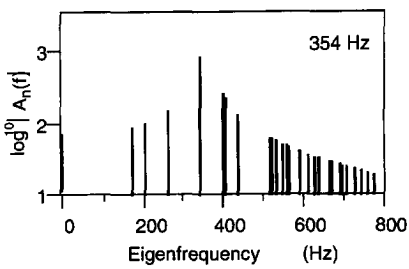

Figure 3.1.8 ; *354 Hz*

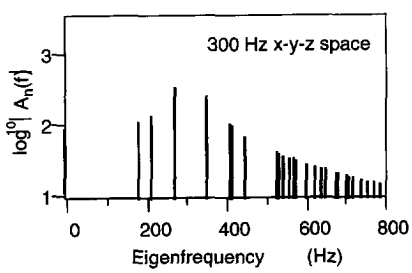

Figure 3.1.9 ; *The modal amplitudes at 300 Hz of the complete enclosure.*

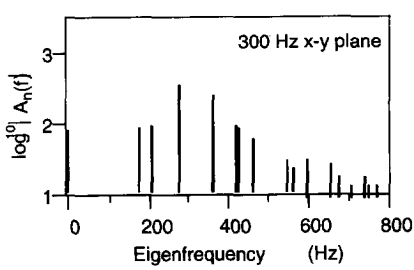

Figure 3.1.10 ; *The modal amplitudes if only the x-y plane is considered.*

There is a slight difference in the amplitudes and there are of course less eigenmodes (approximately 30 eigenmodes up to 1000 Hz). Up to about 300 Hz however, the dominant eigenmodes in the x-y plane are also the dominant eigenmodes of the enclosure (x-y-z space). In active noise control the number of dominant eigenmodes will prove to be very important. A complicated wave field determined by many eigenmodes is difficult to reduce actively.

3.1.4 The eigenmodes in a rectangular box

The number of dominant eigenmodes is studied in the box of compressed wood. In figure 3.1.11 the measurement set-up is drawn schematically. The source is placed near to the ceiling on position $(x_{max}, y_{max}, z_{max})$. The 64 measurement microphones (8x8) are placed on a height of 0.025 m. in a regular grid.

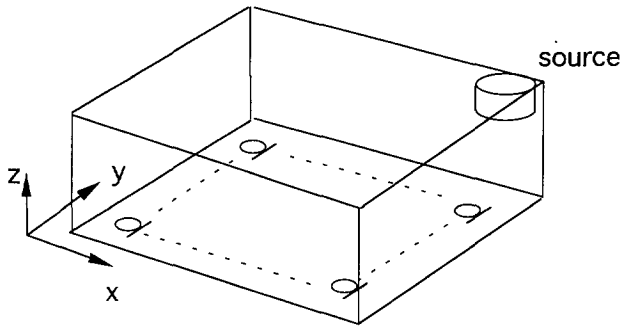

Figure 3.1.11 ; *The measurement set-up, there are 64 microphones.*

The complex eigenvalues are found solving the Helmholtz equation (3.1.1) under the constraint of the boundary conditions. In the box which is used in the experiments the modal damping is small, since the pressure reflection coefficient of the walls is close to one.
The eigenfrequencies of the box can be estimated by measuring frequency responses. A source is placed in one of the corners of the box generating broad band noise while the acoustic pressure is measured with a microphone in an opposite corner. The theoretical values of the wave numbers based on the dimensions of the box (equation 3.1.17) and the measured values are compared. The measured values deviate slightly due to the presence of the source and because the walls are not completely rigid (Table I in appendix B).
Not all dominant eigenmodes contribute to the wave field to the same extent. As derived in the previous sections the wave field can be considered to be a superposition of a limited number of weighed eigenfunctions. The acoustic pressure, measured on a sensor, is in this description data in the space-frequency domain found after a transformation from data in the eigenvalue-frequency domain. The transformation equation is (3.1.2). On the other

hand the amplitudes of the eigenfunctions in a measured wave field are found using the backward transformation. In this way the number of dominant eigenfunctions determining a measured wave field can be measured using many microphones. The equation transforming the (measured) data in the space-frequency domain to the eigenvalue-frequency domain is derived using a least squares solution.
Suppose there are M microphones, placed in the enclosure at positions $\mathbf{x}_1 \cdots \mathbf{x}_M$. The pressures can be put in a pressure vector. The pressure vector can be written as

$$\begin{bmatrix} P(\mathbf{x}_1, f) \\ \vdots \\ P(\mathbf{x}_M, f) \end{bmatrix} = \begin{bmatrix} \vec{\Psi}(\mathbf{x}_1)^T \\ \vdots \\ \vec{\Psi}(\mathbf{x}_M)^T \end{bmatrix} \vec{a}(f) + \vec{\varepsilon} \qquad (3.1.23)$$

where $\vec{\Psi}(\mathbf{x}_m)$ and $\vec{a}(f)$ are N dimensional vectors, N being the number of dominant eigenmodes. The vector $\vec{\varepsilon}$ stands for the errors.
Obviously the vector $\vec{a}(f)$ can be estimated if the eigenfunctions and the values of k_{n_x}, k_{n_y} and k_{n_z} are known (and $M \geq N$). Using a vector and matrix notation the vector $\vec{a}_{est}(f)$ for which the squared error $\vec{\varepsilon}^H \vec{\varepsilon}$ is minimized is (appendix B)

$$\vec{a}_{est}(f) = \left[\boldsymbol{\Psi}^T \boldsymbol{\Psi}\right]^{-1} \boldsymbol{\Psi}^T \vec{P}(f) \qquad (3.1.24)$$

This is the least squares error solution of the (forward) vector equation (3.1.23) and it yields the amplitudes of the eigenmodes (see also section 3.2). Unfortunately the exact eigenfunctions and the exact values of k_{n_x}, k_{n_y} and k_{n_z} are not known, even not in the rectangular enclosure.
In the measurement set up 64 electret microphones are placed in a horizontal plane (z=0.025 m.) in the box, so only the eigenmodes in the x- and y-direction can be measured. In the set-up the largest mutual distance between the microphones is approximately 0.18 m. As a consequence a detectable eigenmode must have a wave length larger than approximately 0.36 m (940 Hz). A loudspeaker is placed in a corner of the box.
The synthetic eigenfunctions

$$\Psi_n(\mathbf{x}) = \cos(k_{n_x} x)\cos(k_{n_y} y)$$

are calculated for 20 eigenvalues (up to 800 Hz) while the values of k_{n_x} and k_{n_y} are computed according to equation (3.1.17). The eigenfunction vector thus is

$$\vec{\Psi}(\mathbf{x})^T = \left[1 \quad \cos(\pi x/L_x) \quad \cos(\pi y/L_y) \quad \ldots \quad \cos(4\pi y/L_y)\right], \qquad (3.1.25)$$

where the last element is the 20th eigenfunction.

The eigenfunction vectors and the measured pressure at the microphones are used in equation (3.1.24). This method to measure the coefficient amplitudes of the x-y plane contains some inaccuracies:

- *for economical reasons 64 microphones of medium quality are used, as a consequence maximum deviations of 25^{o} in phase are found.*
- *spatial aliasing of the eigenfunctions with eigenfrequency above the Nyquist frequency (940 Hz) is inevitable,*
- *the true eigenfunctions and eigenvalues will deviate from the synthetic ones.*

Nevertheless, the method gives the amplitudes of the eigenmodes if the measured wave field in the x-y plane is thought to be built up by the synthetic eigenfunctions, and that will do for the purpose the method is used for: to make an estimation of the number of dominant eigenmodes in the box at a given excitation frequency.

In a first experiment the loudspeaker excites the wave field at 269 Hz, close to the fourth eigenmode (see table I, appendix B). The pressure level found on the microphones is depicted in figure 3.1.12 in a three dimensional plot. The x- and y-axis correspond with

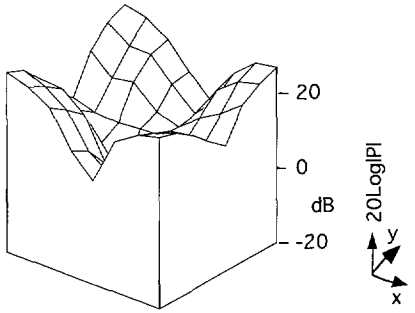

Figure 3.1.12 ; *The pressure level at 269 Hz.*

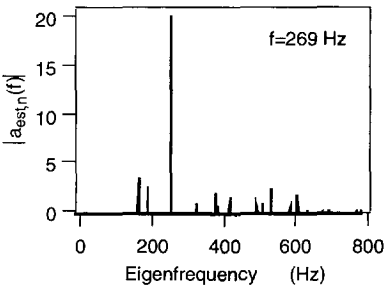

Figure 3.1.13 ; *The estimated amplitude of the coefficient vector.*

the x- and y-axis in the measurement set-up (figure 3.1.11), while on the z-axis the pressure level is depicted in dB. The fourth eigenfunction can clearly be seen in this figure.

The (absolute) mode-coefficient amplitude, calculated with the measured pressures and the synthetic eigenfunctions are depicted in figure 3.1.13. The amplitude of the fourth eigenmode (266 Hz) is much larger than the others.

In a second experiment the wave field is excited at a frequency between two eigenfrequencies (333 Hz). In figure 3.1.14 the pressure level is depicted. The wave field is more complicated and it is determined by more eigenfunctions. In figure 3.1.15 the amplitudes of the eigenmodes are drawn, showing that there are definitely more eigenmodes contributing to the wave field.

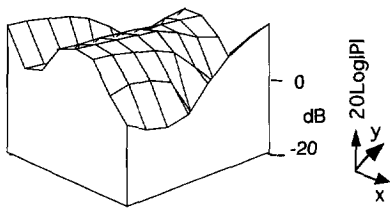

Figure 3.1.14 ; *The pressure level at 333 Hz.*

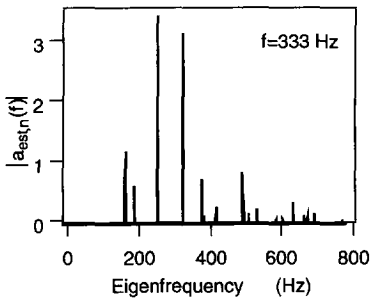

Figure 3.1.15 ; *The estimated amplitude of the coefficient vector.*

In both experiments the number of dominant eigenmodes is limited.
The figures make clear that the measured coefficients depend on the difference in frequency between the excitation frequency and the eigenfrequency.

3.2 Anti noise in an enclosure

The objective in ANC is to minimize the local or global potential energy. However, a ANC system always uses error sensors (microphones) and will in most cases not be capable to measure the global potential energy. In fact the sum of the squares of the pressures on those error sensors is minimized. The implications of this least squares solution for the global and local potential energy can be derived in a simple way using a vector notation. First the least squares solution will be derived.

3.2.1 Least squares solution in anti noise

The pressure on the sensors is determined by the given primary (noise) sources and the controlled secondary (anti-noise) sources. The sum of the squared pressure-amplitude on M sensors due to the primary sources and L secondary sources is

$$\sum_{m=1}^{M}\left|P_{tot}(\mathbf{x}_m,f)\right|^2 = \sum_{m=1}^{M}\left|P_p(\mathbf{x}_m,f)+P_{s,1}(\mathbf{x}_m,f)+\ldots+P_{s,L}(\mathbf{x}_m,f)\right|^2 \qquad (3.2.1)$$

in which $P_p(\mathbf{x}_m,f)$ is the pressure on sensor m due to the primary source configuration, while $P_{s,l}(\mathbf{x}_m,f)$ is the pressure on sensor m due to secondary source l.
Assume that the secondary source l has a (uniform) surface velocity $V_l(f)$ and that $H_{m,l}(f)$ is the frequency response of source l to sensor m. Equation (3.2.1) can be rewritten to

$$\sum_{m=1}^{M}\left|P_{tot}(\mathbf{x}_m,f)\right|^2=\sum_{m=1}^{M}\left|P_p(\mathbf{x}_m,f)+\sum_{l=1}^{L}H_{m,l}(f)V_l(f)\right|^2. \qquad (3.2.2)$$

Using the vector notation $\vec{H}_l(f)=\left[H_{1,l}(f)\ \ \ldots\ \ H_{M,l}(f)\right]^T$, equation (3.2.2) can be rewritten to

$$\left|\vec{P}_{tot}(f)\right|^2=\left|\vec{P}_p(f)+\sum_{l=1}^{L}\vec{H}_l(f)V_l(f)\right|^2. \qquad (3.2.3)$$

The L source-strengths are placed in a vector too, giving

$$\left|\vec{P}_{tot}(f)\right|^2=\left|\vec{P}_p(f)+\mathbf{H}(f)\vec{V}(f)\right|^2, \qquad (3.2.4)$$

in which $\mathbf{H}(f)=\left[\vec{H}_1(f)\ \ \ldots\ \ \vec{H}_L(f)\right]$, a MxL matrix, and $\vec{V}(f)=\left[V_1(f)\ \ \ldots\ \ V_L(f)\right]^T$. The optimal source-strength vector which minimizes the squared vector-length $\left|\vec{P}_{tot}(f)\right|^2$, is the least squares solution of the vector-equation

$$\vec{P}_{tot}(f)=\vec{P}_p(f)+\mathbf{H}(f)\vec{V}(f), \qquad (3.2.5)$$

while $\left|\vec{P}_{tot}(f)\right|^2$ is the least squares error.

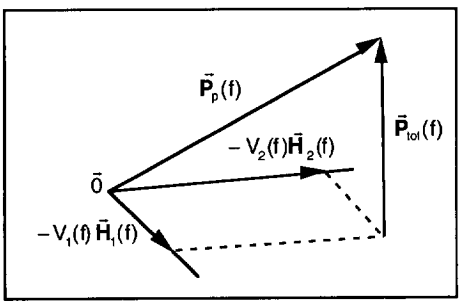

Figure 3.2.1 ; *Geometric interpretation of anti noise on the sensors.* $\vec{V}(f)=[V_1(f)\ \ V_2(f)]^T$, *the dimension is given by the number of sensors.*

This least-squares problem can be interpreted as a geometric problem in M dimensional space. The length of the M dimensional vector $\vec{P}_{tot}(f)$ is minimum if $\vec{P}_{tot}(f)$ is orthogonal to all vectors $\vec{H}_l(f)$ (figure 3.2.1), in other words if the dot product is zero for all l:

$$\vec{H}_l(f) \cdot \vec{P}_{tot}(f) = 0, \text{ all } l. \tag{3.2.6}$$

Developing the dot products we find

$$\mathbf{H}^H(f)\vec{P}_p(f) + \mathbf{H}^H(f)\mathbf{H}(f)\vec{V}_{opt}(f) = \vec{0}, \tag{3.2.7}$$

yielding

$$\vec{V}_{opt}(f) = -\left[\mathbf{H}^H(f)\mathbf{H}(f)\right]^{-1}\mathbf{H}^H(f)\vec{P}_p(f). \tag{3.2.8}$$

The optimum source-strength vector can only be found if the square matrix $\mathbf{H}^H(f)\mathbf{H}(f)$ is not singular. Singularity of this matrix occurs if the vectors $\vec{H}_l(f)$ do not form a independent system, so if

$$\vec{H}_l(f) = \sum_{i=1, i\neq l}^{L} c_i \vec{H}_i(f) \tag{3.2.9}$$

and c_i are complex constants.

Considering the geometric interpretation some important consequences are clear:

1] A unique optimum vector cannot be found if $\vec{H}_l(f) = \vec{0}$ which will happen if all the sensors are placed positions where the acoustic pressure due to source l is zero.

2] A unique optimum vector cannot be found if $L > M$ (more secondary sources than sensors).

3] If $L<M$, adding an independent secondary source will reduce the vector length of the perpendicular $\vec{P}_{tot}(f)$.

4] If $L=M$ the vector length of the perpendicular $\vec{P}_{tot}(f)$ will be zero since the independent vectors $\vec{H}_l(f)$ form a complete base for the M dimensional space. This means that if the number of sources equals the number of sensors, the acoustic pressure on the sensors is cancelled completely.

Using the optimal source vector (3.2.8), the resulting pressure on the sensors is in vector notation

$$\vec{P}_{tot}(f) = \vec{P}_p(f) - \mathbf{H}(f)\left[\mathbf{H}^H(f)\mathbf{H}(f)\right]^{-1}\mathbf{H}^H(f)\vec{P}_p(f). \tag{3.2.10}$$

In a number of experiments the reduction in an enclosure with the help of anti noise will be shown. The (error) sensors are placed along the walls of the enclosure (unless stated otherwise) to avoid that $\vec{H}_l(f) = \vec{0}$. In none of the experiments the number of sources is larger than the number of sensors. The source strengths of the secondary (anti-noise) loudspeakers is calculated (in an adaptive algorithm) with equation 3.2.9.

3.2.2 Global reduction in an enclosure

The optimal source vector giving the least squares solution of the pressure on the sensors will not necessarily minimize the global potential energy. The positions of sources and sensors combined with the values (amplitude and phase) of matrix **A(f)** determine the global result of reduction on the sensors. The number of sources necessary to get a substantial reduction of the global potential energy can be derived simply using a geometric interpretation in N dimensional space, N being the number of dominant eigenmodes.
The unscaled potential energy density due to a frequency component f is derived in section 2.1 and is given by equation (2.1.22). The *unscaled* global potential energy in an enclosure with volume $V_{enclosure}$ is:

$$E'_{pot,acoustic}(f) = \int_{V_{enclosure}} |P(\mathbf{x},f)|^2 dV.$$

Assuming that $\beta(\mathbf{x})$ is small the (normalized) eigenfunctions are real. Using equations (3.1.19), (3.1.7) and (3.1.8) the estimated unscaled global potential energy is

$$E'_{p,est}(f) = \vec{a}(f)^H \vec{a}(f), \tag{3.2.11}$$

in which $\vec{a}(f)$ is a N-dimensional vector. The vector $\vec{a}(f)$ can be written as a superposition of contributions due to the primary source and the secondary sources. These velocity sources are mounted near the walls of the enclosure and have a uniform surface velocity. The source-strength is given by equation (3.1.13). For convenience it is assumed there is only one primary source at a position $\mathbf{x}_p$ having a surface A_p and a velocity $V_p(f)$. There are L secondary sources at positions $\mathbf{x}_l$ having surfaces A_l and surface velocities $V_l(f)$ $(l = 1,..L)$. The elements of the coefficient vector are found with the help of the equations (3.1.10) and (3.1.13)

$$a_n(f) = \frac{-jk\rho_s c}{(k^2 - k_n^2)} \left[V_p(f) \int_{A_p} \Psi_n(\mathbf{x}_p) dS + \sum_{l=1}^{L} V_l(f) \int_{A_l} \Psi_n(\mathbf{x}_l) dS \right]. \tag{3.2.12}$$

In anti noise the source strengths are controlled by the surface velocities of the sources, therefore the coefficient vectors are written as a product of the surface velocity and the coefficient vectors for a **unit** velocity. The coefficient vector of unit velocity for the primary source is

$$\vec{a}_{pu}(f) = \mathbf{A}(f) \int_{A_p} \bar{\Psi}(\mathbf{x}_p) dS, \tag{3.2.13}$$

and the coefficient vector of unit velocity for secondary source l equals

$$\vec{a}_{su,l}(f) = \mathbf{A}(f)\int_{A_l} \vec{\Psi}(\mathbf{x}_l)dS. \tag{3.2.14}$$

The elements of the vector $\vec{a}_{pu}(f)$ are

$$a_{pu,n}(f) = \frac{-jk\rho_s c}{\left(k^2 - k_n^2\right)} \int_{A_p} \Psi_n(\mathbf{x}_p)dS, \tag{3.2.15}$$

and similar for $\vec{a}_{su,l}$. The total vector now can be written in the form

$$\vec{a}(f) = V_p(f)\vec{a}_{pu}(f) + \sum_{l=1}^{L} V_l(f)\vec{a}_{su,l}(f). \tag{3.2.16}$$

The optimum source-strength-vector $\vec{V}(f) = [V_1(f) \quad ... \quad V_L(f)]^T$ minimizing the length of the coefficient vector $\vec{a}(f)$ (and so the global potential energy) is the least squares solution of equation (3.2.13). Similar to the geometric interpretation in M (number of sensors) dimensional space, the optimum vector $\vec{a}(f)$ is orthogonal to all vectors $\vec{a}_{su,l}$ (figure 3.2.2).

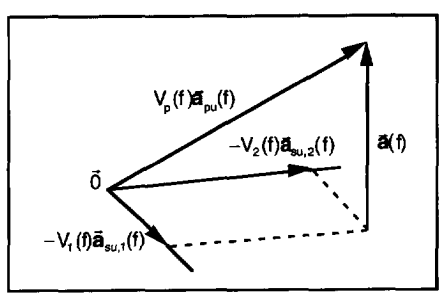

Figure 3.2.2 ; *Geometric interpretation of the least squares solution in N-dimensional space. There are 2 secondary sources.*

In figure 3.2.2 a geometric interpretation of the least squares solution is depicted. A substantial global reduction only can be realised if the secondary source vectors can construct a vector more or less in the direction of the primary source vector. Since the vectors are largely defined by the N dominant eigenmodes, a considerable global reduction is guaranteed if there are N independent secondary source vectors, and so N secondary sources distributed in the enclosure. This means that at low modal densities and at an excitation frequency close to an eigenfrequency the number of secondary sources needed is small.

However, a fair global reduction with less sources is possible if their positions are cleverly chosen. The direction of a source vector in N dimensional space is given by the (dominant) eigenmodes and the eigenfunction values at the source position (3.2.15)., the vector

Obviously the vectors $\vec{a}_{pu}(f)$ and $\vec{a}_{su,l}(f)$ are equal if the positions of primary source and secondary source l are equal. Furthermore, as long as the mutual distance of the two sources is small compared to the wavelength of the highest order dominant mode, the coefficient vectors will be approximately the same which means that only one source is needed.

It is to be noted that the potential energy with or without anti noise is written as a superposition of the squared weighed eigenfunctions. Since the eigenfunctions describe standing waves, there is no power flow in the enclosure. This means that, similar to anti noise in a duct, no (acoustic) power flow to or from the sources is involved in anti noise in an enclosure. The reduction is caused by a destructive interference of the primary and secondary wave fields.

A few experiments in the rectangular box are carried out to study the reduction of the acoustic pressure at the microphones in the x-y plane in the box and to verify the vector presentation of anti-noise. At low frequencies the reduction at the microphones may be considered to be close to the global reduction.

3.2.3 Anti noise in the rectangular box: reduction in the x-y plane

The experiments are carried out in the rectangular box mentioned before. The anti-noise source signals are calculated with the help of a multi channel (8 inputs, 4 outputs) active noise controller for periodic noise ('OCTOPUS'). There are six controller microphones mounted close to the bottom and one to four anti-noise sources mounted near the ceiling. The wave field is measured with 64 measurement microphones (figure 3.1.10). In a first experiment the primary source is placed in a corner of the box (see figure 3.1.10), while an anti-noise source is placed in the corner opposite to it. The controller microphones are placed along the walls (see figure 3.2.3).

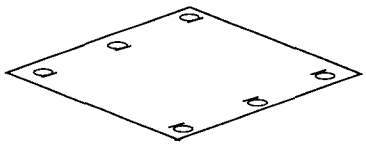

Figure 3.2.3 ; *The positions of the controller microphones close to the bottom of the box.*

The excitation frequency is 333 Hz which is between the fourth and fifth eigenfrequency. In figure 3.2.4 the primary wave field is shown in a three dimensional presentation, while in figure 3.2.4 the estimated modal amplitudes are depicted.

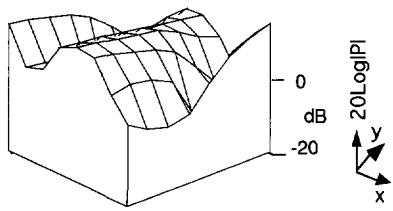

Figure 3.2.4 ; *The pressure level at 333 Hz.*

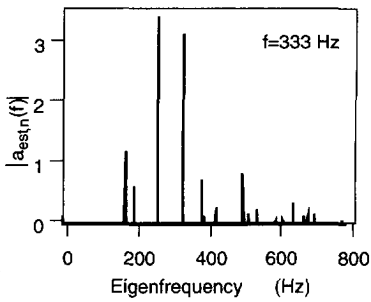

Figure 3.2.5 ; *The estimated amplitude of the coefficient vector (primary field).*

Global reduction with the help of the secondary source is not possible in this situation. At the excitation frequency there are a good deal of dominant eigenmodes. Furthermore, the eigenfunctions at the two source-positions are not consistent in phase (figure 3.1.2) , and as a result the vectors $\vec{a}_{pu}(f)$ and $\vec{a}_{su}(f)$ have completely different directions in the N dimensional coefficient space. In figure 3.2.6 the resulting wave field is shown. Although the form of the wave field is definitely different from the primary field shown in figure 3.2.4, the reduction of the averaged squared acoustic pressure on the 64 microphones is small (approximately 3.2 dB).

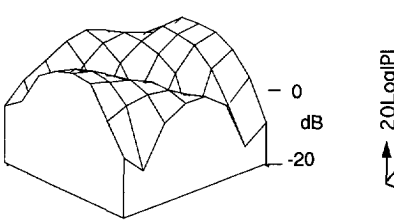

Figure 3.2.6 ; *The pressure level at 333 Hz.*

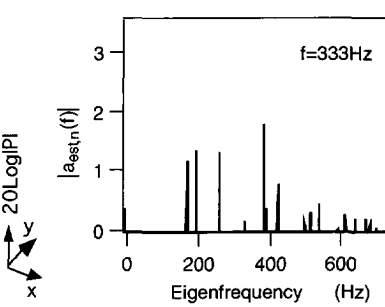

Figure 3.2.7 ; *The estimated amplitude of the coefficient vector (residual field).*

The estimated modal amplitudes are shown in figure 3.2.7. Noticeable is the shift in modal amplitudes due to the anti-noise wave field: the fourth and fifth eigenmode which are consistent in phase on the source positions (figure 3.1.2) are reduced while some other eigenmodes (2, 3 and 6) are enlarged. This experiment shows that due the different directions of the coefficient vectors the anti-noise source cannot reduce the potential energy substantially.

In a second experiment the secondary source is positioned again in the opposite corner,

the controller microphones are placed along the walls. In this experiment the excitation frequency is 269 Hz, which is near to the fourth eigenmode (1-1-0 mode). In figure 3.2.8 the primary wave field and in figure 3.2.9 the estimated coefficient amplitudes are depicted.

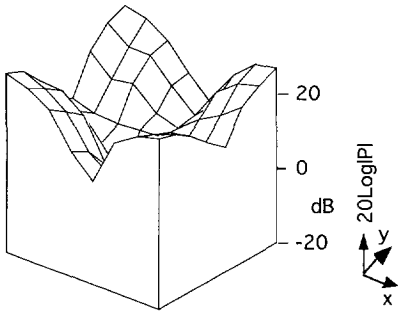

Figure *3.2.8* ; *The pressure level at 269 Hz.*

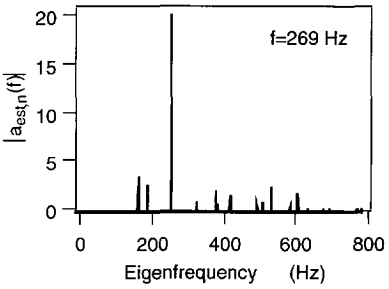

Figure *3.2.9* ; *The estimated amplitude of the coefficient vector (primary field).*

At this frequency the wave field is largely defined by the corresponding eigenfunction. This means that there is only one dominant eigenmode and that, as a result, the coefficient vectors (3.2.14) are pointing more or less in the same direction. In figure 3.2.10 the reduced wave field is shown. In spite of the fact that there is only one secondary source, the reduction of the averaged squared acoustic pressure at the microphones is much larger than in the previous experiment, about 10 dB, due to a considerable reduction of the fourth eigenmode. The estimated mode coefficient amplitudes are depicted in figure 3.2.11. The fourth eigenmode is reduced by approximately 25 dB.

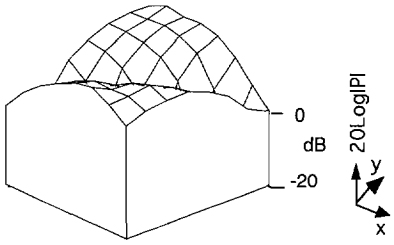

Figure *3.2.10* ; *The pressure level of the residual at 269 Hz (one source)*

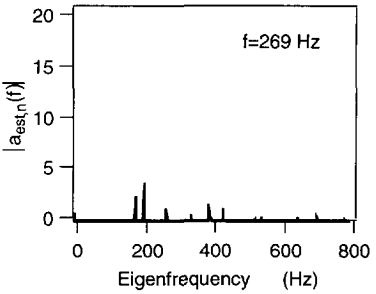

Figure 3.2.11 ; *The estimated amplitudes of the coefficient vector (residual field).*

This experiment shows that good reduction at the microphones is possible with one source if the wave field is largely determined by one dominant eigenmode.
The reduction can be improved by using more anti-noise sources. Three sources are

added to the set-up and the ideal source strength vector (3.2.8) is computed. The reduced field is depicted in figure 3.2.12. The reduction is better, resulting in a reduction of the primary wave field at the microphones of 15 dB.

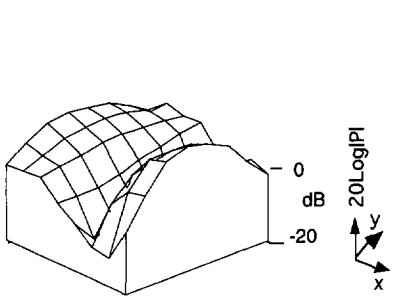

Figure 3.2.12 ; *The pressure level of the residual at 269 Hz (four sources)*

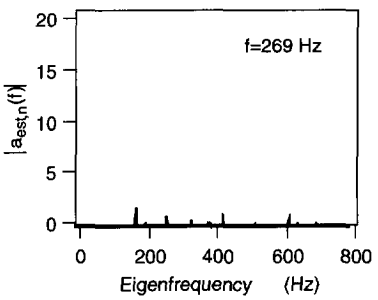

Figure *3.2.13* ; *The estimated amplitudes of the coefficient vector (residual field).*

The 4 coefficient vectors $\vec{a}_{su,l}$ are capable of reproducing the primary coefficient vector $\vec{a}_{pu}(f)$ better, and in particular the first few eigenmodes are reduced (figure 3.2.13).
In a third experiment the secondary source is placed next to the primary source. The cone-centers have the same x- and z-coordinates. The mutual distance of the cone-centers is approximately 0.15 m. The primary source is exciting the wave field at a frequency of 150 Hz, which is below the eigenfrequency of the 1-0-0 mode. In figure 3.2.14 the pressure level of the primary wave field is depicted , while in figure 3.2.15 the estimated amplitudes of the coefficient vector are drawn.

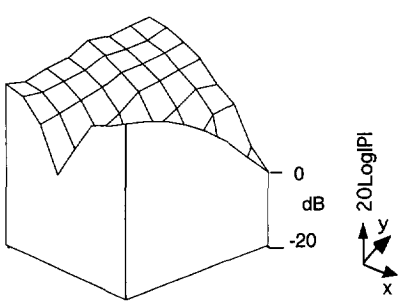

Figure *3.2.14* ; *The pressure level at 150 Hz .*

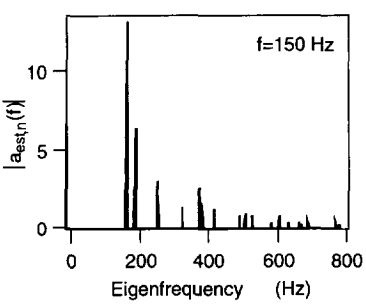

Figure *3.2.15* ; *The estimated amplitude of the coefficient vector (primary field).*

In figure 3.2.16 the pressure level of the reduced wave field is shown. Although there are several dominant eigenmodes in the primary wave field and only one anti-noise source, the reduction at the microphones is considerable (approximately 18 dB).

In figure 3.2.17 the resulting estimated coefficient vector is depicted. The eigenmodes corresponding to frequencies up to approximately 500 Hz are reduced.

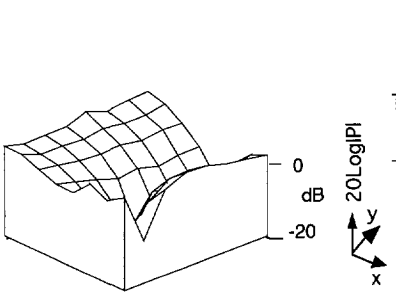

Figure 3.2.16 ; *The pressure level of the residual at 150 Hz (one source next to the primary source).*

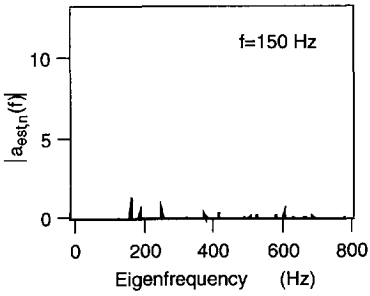

Figure 3.2.17 ; *The estimated amplitudes of the coefficient vector (residual field).*

The results of the experiment show that the anti-noise source next to the primary source is capable of reproducing the (negative) primary source vector quite well at this frequency, thus giving a substantial reduction.
The three experiments show that the reduction of the global potential energy can be described by a reduction of the modal amplitudes of the residual wave field. The results of the experiments match fairly well to the theory.
Global reduction does not always mean that the pressure level at all positions in the enclosure decreases. Locally the pressure level can increase (figures 3.2.4 and 3.2.6). In some cases it is desirable that the noise level is reduced at a particular position in the enclosure.

3.2.4 Local reduction in the box

Local reduction can be accomplished by placing the sensors on particular positions, thus (for instance) forcing the wave field in a desired eigenmode.
In a last experiment two controller sensors are placed close to the middle of the enclosure at a mutual distance of 0.2 m.. There are two loudspeakers in the opposite corners of the box. The excitation frequency is 333 Hz. In figure 3.2.18 the set-up with sources and controller microphones is schematically drawn. Since the number of controller sensors equals the number of anti-noise sources the sound signal on the microphones is reduced to zero. The 2 controller sensors are placed between the 64 measurement sensors. In figure 3.2.19 the residual pressure level of the wave field is shown.

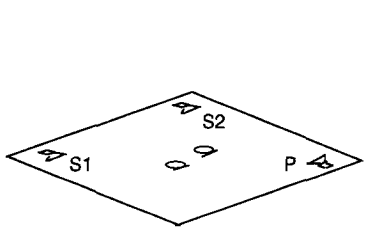

Figure *3.2.18 ; The measurement set -up for local reduction.*

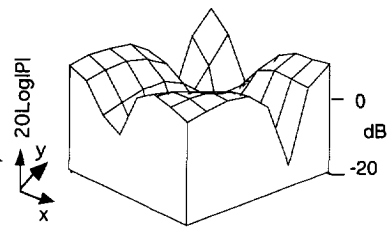

Figure 3.2.19 ; *The pressure level of the residual wave field at 333 Hz.*

Around the microphones the reduction of the pressure level is approximately 30 dB. The reduction of the averaged squared acoustic pressure on the microphones (in the x-y plane) however is small (approximately 4 dB). The wave field looks different compared to the primary wave field (figure 3.2.4). The residual wave field is forced into the 1-1-0 mode. In figure 3.2.20 the estimated modal amplitudes are depicted showing the high level of the fourth eigenmode.

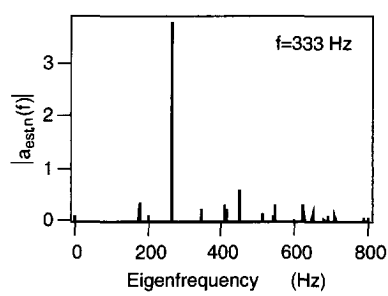

Figure 3.2.20 ; *The estimated amplitudes of the coefficient vector after local reduction.*

The experiment makes clear that locally the reduction is quite large in spite of the fact that there are only two anti noise sources. Furthermore, by forcing the wave field into the 1-1-0 mode the pressure level is low on the nodal lines. Local reduction can be used to give high reductions locally, but it may increase the pressure level on other positions.

3.3 Conclusions

The description of a wave field as a superposition of eigenmodes has been first applied to the anti noise situation by Nelson c.s. [7-9]. In this chapter a geometric interpretation of the anti noise problem with the eigenmode theory is given using vectors comprising the

modal amplitudes of the primary and secondary sources. The modal amplitudes of the eigenmodes of the excited wave field in a given enclosure are not only a function of the frequency, they also depend on the position of the sources. The wave field in the entire enclosure can only be reduced completely if the number of anti noise sources is equal to (or larger than) the number of eigenmodes. However, a substantial reduction is achieved if the number of sources is equal to the number of *dominant* eigenmodes.

In a number of experiments the amplitudes of the eigenmodes of a rectangular box of reinforced compressed wood are estimated in the situations with and without anti noise at several frequencies. The estimation is based on pre-calculated eigenfunctions and the measured pressure in a horizontal plane of the box. The results agree well with the theory. They show that at an eigenfrequency, where there is only one dominant eigenmode, a substantial reduction can be achieved with only one anti noise source. Furthermore, if the noise source and the anti noise source are positioned very close to each other, and so their modal amplitude vectors are more or less the same, a considerable global reduction can be achieved with one source, even if there are several dominant eigenmodes.

4. THE USE OF ADAPTIVE CONTROL IN ANTI NOISE

Introduction

In the previous two chapters the implications of anti-noise for acoustic wave fields in one and three dimensional situations were discussed and the optimal source strengths of the anti-noise sources were derived. The source strengths are determined by the primary signals, as they are measured on the error sensors, and depend on the transfer functions from anti-noise sources to sensors. In this thesis it is assumed that the primary signals to be reduced are excited by rotating machinery, like an electric driven fan or the engine of a car. Rotating machines give rise to a periodic primary signal comprising the fundamental frequency, being the revolution frequency of the main shaft, and a number of harmonics and sub harmonics. The transfer functions from anti-noise sources to sensors are partly acoustic, for example the inside of a duct and the interior of a car. Due to alterations in the revolution frequency and due to changes in the acoustic environment, the characteristics of the primary signal are not completely time invariant. Furthermore, the transfer functions from anti-noise sources to sensors may not be fully stationary. As a result the optimal source strengths vary in time and adaptive control methods are needed to adjust the source strengths of the anti-noise sources.

There is a variety of methods for the control of periodic noise: the controller can be analog or discrete, it can have a feedforward or a feedback structure and a time domain or a frequency domain approach. Already in 1975 Widrow e.a. describe a feed forward controller applied to estimate periodic noise corrupted by additional noise [10]. Glover [11] used the principles to construct an adaptive notch filter. Most control algorithms for periodic noise are based on these papers. Elliott e.a. [12] introduced the multiple error algorithm and applied it to a MIMO system comprising multiple inputs (microphones) and multiple outputs (loudspeakers). An up to date comparison of control methods for periodic noise is made by Sievers [13].

The signals discussed in this chapter are continuous time functions that are sampled. The sampling interval is Δt, and the first sample is taken at $t=\Delta t$. For convenience the notation $y(k)$ is used instead of the more proper notation $y(k\Delta t)$ for the value of the signal at $t=k\Delta t$. Unless stated otherwise k has a value ranging from 1 to n.

In most cases a sensor can be mounted on the rotating equipment giving within a certain accuracy the momentary angular phase of the main shaft. Based on this sensor signal, wave form generators can construct complex periodic time functions of unit amplitude. If the revolution frequency of the main shaft is stationary, each of the time functions comprises only one frequency component:

$$\exp(j2\pi f_\nu k\Delta t), \qquad \nu = 1,\ldots N, \tag{4.0.1}$$

in which f_ν is one of the harmonics of f_1, the fundamental frequency of the main shaft. The frequency components fulfill the Nyquist criterion ($f_{\nu,max} < 1/2\Delta t$).

It is realistic to assume that there is a *linear* relation between these time functions and the related frequency components of the primary signal. The signals generated by the wave form generators can serve as a reference signal of the primary signal and therefore can be used as a *feed signal* for a controller. As a result, the adaptive control methods to adjust the optimal source strengths can be based on *linear feedforward control.* Linear feedforward control generally gives a good reduction if the total transfer functions from anti-noise controller outputs $s_\ell(n)$ to error signal inputs $\varepsilon_m(k)$ are known. The total transfer function comprises not only the acoustic transfer from source position to sensor position, but also the transfer functions of filters and transducers. Bear in mind that the index ℓ denotes the output channel number while the index m denotes the input channel number. In figure 4.0.1 the feedforward control configuration is depicted. Only one anti-noise source and only one error sensor is shown.

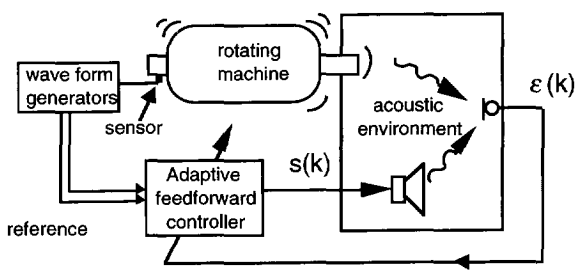

Figure 4.0.1 ; *The ANC feedforward configuration for rotating machinery.*

The objective in ANC is to minimize the measured error signal $\varepsilon(k)$ (figure 4.0.1), which is the sum of the signals generated by the primary noise source and the secondary, anti-noise source, $y_p(k)$ and $y_s(k)$ respectively.
The ANC set-up drawn in figure 4.0.1 can be represented schematically in a block diagram as in figure 4.0.2 in which the waveform generators, the rotating machine and the acoustic environment are replaced by one process, having the reference signal as an *input.* The output of this primary process is the primary signal $y_p(k)$.

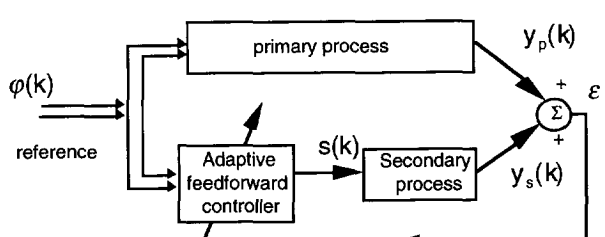

Figure 4.0.2 ; *Block diagram of the ANC feedforward configuration.*

The controller output is the signal $s(k)$. The secondary process is the function transferring the controller output into the process output $y_s(k)$. Besides the frequency response of the transducers and electronic filters, the secondary process comprises the acoustic transfer function from anti-noise loudspeaker to error microphone (see figure 4.0.1). The type of linear model with which the primary process is described, and the type of linear model used in the controller depend on the type of reference signal.

The time input vector

The addition of the outputs of the wave form generators yields a single reference signal comprising all the frequency components to be reduced. Assume there are N frequency components, then the input signal based on a single reference signal is

$$\varphi(k) = \sum_{\nu=1}^{N} \exp(j2\pi f_\nu k\Delta t). \qquad (4.0.2)$$

This signal serves as an input of the linear primary process and as an input of the linear adaptive feedforward controller (figure 4.0.2). A single input signal generally will lead to a polynomial process- and controller model. A well known, simple but in most cases stable polynomial model is the finite impulse response (FIR). If that for both the primary process and the controller a FIR of length I may be used, then both the primary signal $y_p(k)$ and the controller output $s(k)$ are a linear combination of the sequence of the input signal elements $\varphi(k), \varphi(k-1), \cdots, \varphi(k-I+1)$. The controller model based on the FIR often is called a tapped delay, or transversal filter. The input elements at $t=k\Delta t$ can be gathered in a 'time' vector:

$$\vec{\varphi}_t(k) = [\varphi(k)\ \varphi(k-1)\ \cdots\ \varphi(k-I+1)]^T. \qquad (4.0.3)$$

The Fourier input vector

If the outputs of the wave form generators are used independently, the inputs of the primary process and the controller are multi dimensional. Assume that the primary signal comprises I frequency components $\nu = 1,\ldots I$, then the primary signal $y_p(k)$, and also the controller output $s(k)$ are a linear combination (with complex coefficients) of the time functions

$$\varphi_\nu(k) = \exp(j2\pi f_\nu k\Delta t), \qquad (4.0.4)$$

which are the functions on which the Fourier transform is based. The complex coefficients therefore are the Fourier coefficients. Thus, the input elements at $t=k\Delta t$ can be gathered in a 'Fourier' vector:

$$\vec{\varphi}_f(k) = [\varphi_1(k)\ \varphi_2(k)\ \cdots\ \varphi_I(k)]^T. \qquad (4.0.5)$$

In this chapter the theory of linear adaptive feedforward control will be reviewed and applied step by step to the anti-noise configuration. Theoretical implications will be illustrated with results of measurements in the laboratory. In the first three sections of this chapter the transfer functions from secondary sources to error sensors are supposed to be time invariant whereas in the fourth section time varying secondary process parameters will be considered. In the first part of section 4.1 it will be assumed that the acoustic environment and the revolution frequency are stationary as well.

4.1 Basic equations

4.1.1 Linear control

The ANC controller problem may be considered to be basically a parameter estimation problem. Assume the unknown parameters describing the primary process have to be estimated while the primary signal $y_p(k)$ can be observed and the input signal(s) $\varphi(k)$ are known. The acoustic environment and the revolution frequency are assumed to be stationary, so the process parameters are time-invariant. In figure 4.1.1 the parameter estimation configuration is depicted.

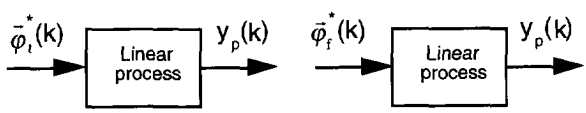

Figure 4.1.1 ; *The output $y_p(k)$ is a linear combination of the 'time' input values $\vec{\varphi}_t^*(k)$ or the 'Fourier' input values $\vec{\varphi}_f^*(k)$.*

The parameters to be estimated using the sequential time input $\vec{\varphi}_t(k)$ are the elements of the FIR (length I) of the primary process. On the other hand, using the Fourier inputs $\vec{\varphi}_f(k)$, each element representing one frequency, the parameters to be estimated are the complex Fourier coefficients of the primary process.
Both the time input vector $\vec{\varphi}_t(k)$ and the Fourier input vector $\vec{\varphi}_f(k)$ are written as a *complex conjugate* because it makes the notation in the derivations more straightforward.
In a general notation, common in adaptive control, process parameters are denoted by the symbol θ_i. For both linear models, the output can be written in a vector notation as

$$y_p(k) = \vec{\varphi}^H(k)\vec{\theta}, \text{ and } k=1,...n, \qquad (4.1.1)$$

in which $\vec{\theta}$ is the time invariant I dimensional vector containing either the FIR filter coefficients if the time input is used or the I dimensional vector containing the complex Fourier coefficients if the Fourier inputs are used.
The following derivations can be applied to both models, since they are both linear.
The n observations are collected in the vector $\vec{y}_p(n) = \left[y_p(1) \quad \ldots \quad y_p(n)\right]^T$ and the n input vectors are written as the matrix $\Phi(n) = \left[\vec{\varphi}(1) \quad \cdots \quad \vec{\varphi}(n)\right]^H$, yielding

$$\vec{y}_p(n) = \Phi(n)\vec{\theta}, \tag{4.1.2a}$$

which becomes the convolution matrix if the time input vector is used:

$$\begin{pmatrix} y_p(1) \\ y_p(2) \\ \vdots \\ y_p(n) \end{pmatrix} = \begin{pmatrix} \varphi^*(1) & \varphi^*(0) & \ldots & \varphi^*(2-I) \\ \varphi^*(2) & \varphi^*(1) & \ldots & \varphi^*(3-I) \\ \vdots & \vdots & & \vdots \\ \varphi^*(n) & \varphi^*(n-1) & \ldots & \varphi^*(n-I+1) \end{pmatrix} \begin{pmatrix} \theta_0^t \\ \theta_1^t \\ \vdots \\ \theta_{I-1}^t \end{pmatrix}, \tag{4.1.2b}$$

and the inverse discrete Fourier transformation if the Fourier input vector is used:

$$\begin{pmatrix} y_p(1) \\ y_p(2) \\ \vdots \\ y_p(n) \end{pmatrix} = \begin{pmatrix} \varphi_1^*(1) & \varphi_2^*(1) & \ldots & \varphi_I^*(1) \\ \varphi_1^*(2) & \varphi_2^*(2) & \ldots & \varphi_I^*(2) \\ \vdots & \vdots & & \vdots \\ \varphi_1^*(n) & \varphi_2^*(n) & \ldots & \varphi_I^*(n) \end{pmatrix} \begin{pmatrix} \theta_1^t \\ \theta_2^t \\ \vdots \\ \theta_I^t \end{pmatrix}. \tag{4.1.2c}$$

Now the I process parameters can be estimated with a least squares solution. For $n \geq I$ and a non singular input correlation matrix $\Phi^H(n)\Phi(n)$ the least squares solution is

$$\vec{\theta}_{ls}(n) = \left(\Phi^H(n)\Phi(n)\right)^{-1}\Phi^H(n)\vec{y}_p(n). \tag{4.1.3}$$

The objective in ANC is to design a secondary signal $y_s(k)$ having the same amplitude as the primary signal, but the opposite sign. In the absence of extraneous noise the addition of the primary and secondary signal yields a residual ideally equal to zero. Contrary to the parameter estimation configuration shown in figure 4.1.1, in ANC the output-error is the observed variable. The output-error is the addition of the primary signal and the secondary signal. The basic output-error model is depicted in figure 4.1.2. The ANC feedforward configuration given in figure 4.0.2 may be considered to be a modification of the basic output-error configuration, the modification being the presence of the secondary process. In the derivations first the basic output-error configuration will be considered. At the end of this section the optimal controller parameters in the ANC configuration will be derived.

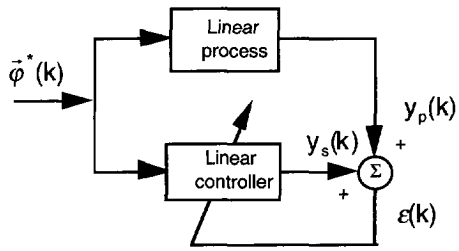

Figure 4.1.2 ; *The basic output-error configuration.*

The optimal controller parameters minimizing the output-error can be estimated if the input is known and the error signal is observed for a number of samples.
Assume that for k=1,...n the stationary parameters of the linear controller are $\vec{\theta}_c$, then

$$\vec{y}_s(n) = \Phi(n)\vec{\theta}_c. \tag{4.1.4}$$

The set of parameters that minimizes the error $\varepsilon(k)$ for k=1,...n

$$\varepsilon(k) = y_p(k) + y_s(k), \tag{4.1.5}$$

can be estimated if the sum of the squares of the n errors $\varepsilon(k)$, the cost function

$$J(\vec{\theta}_c) = \tfrac{1}{2}\sum_{k=1}^{n} \varepsilon^H(k)\varepsilon(k) = \tfrac{1}{2}\sum_{k=1}^{n} \left|y_p(k) + y_s(k)\right|^2, \tag{4.1.6}$$

is minimized. Note that if $\varepsilon(k)=0$ than $\vec{y}_p(n) = -\vec{y}_s(n)$.
The solution with a least squares error (LSE) can be found for $n \geq I$ and a non singular input correlation matrix $\Phi^H(n)\Phi(n)$:

$$\vec{\theta}_{c,lse}(n) = -\left(\Phi^H(n)\Phi(n)\right)^{-1}\Phi^H(n)\vec{y}_p(n). \tag{4.1.7}$$

If the closed loop configuration shown in figure 4.1.2 is used, the LSE equation can not be found directly since the process output vector $\vec{y}_p(n)$ is not available. Furthermore, it may require a considerable computational effort to calculate the inverse matrix which is unfavorable for real time, sample based systems. Therefore other methods are needed to estimate the optimal controller parameters. There are several methods to find adaptively the least squares error solution $\vec{\theta}_{c,lse}(n)$, and there is much literature about the subject (Widrow [14], Astrom [15] and many others). A majority of the estimation methods is based on *gradient* search methods or the *recursive* least squares solution (RLS). In this thesis only the recursive approach will be reviewed.

4.1.2 Recursive Least Squares Error and Projection method

Both underlined problems mentioned above are avoided if the *recursive* least squares error (RLSE) method is used. In the RLSE method an estimate of the vector $\vec{y}_p(n)$ is used and the inverse matrix is calculated recursively.
If the controller parameters are estimated with an arbitrary estimation method using the configuration shown in figure 4.1.2, the most recent estimate at $t=k\Delta t$ is $\vec{\theta}_{c,e}(k-1)$, so

$$y_s(k) = \vec{\varphi}^H(k)\vec{\theta}_{c,e}(k-1), \tag{4.1.8}$$

Combination of equations (4.1.5) and (4.1.8) gives the estimate of $y_p(k)$

$$y_{p,e}(k) = \varepsilon(k) - \vec{\varphi}^H(k)\vec{\theta}_{c,e}(k-1). \tag{4.1.9}$$

The LSE based on (4.1.9) is

$$\vec{\theta}_{c,e}(n) = -\left(\Phi^H(n)\Phi(n)\right)^{-1}\Phi^H(n)\vec{y}_{p,e}(n) \tag{4.1.10}$$

Following the derivation of the recursive least squares solution as described for example by Astrom [15], the input correlation matrix is written as

$$\mathbf{P}(n) = \left(\Phi^H(n)\Phi(n)\right)^{-1} = \left(\sum_{k=1}^{n}\vec{\varphi}(k)\vec{\varphi}^H(k)\right)^{-1}, \tag{4.1.11}$$

leading to a recursive solution (appendix C):

$$\vec{\theta}_{c,rlse}(n) = \vec{\theta}_{c,rlse}(n-1) - \mathbf{P}(n)\vec{\varphi}(n)\varepsilon(n). \tag{4.1.12}$$

The matrix $\mathbf{P}(n)$ can be found recursively with the help of the simple recursive relation for the *inverse* matrix $\mathbf{P}^{-1}(n)$ (appendix C, equation C.2) and the matrix inversion lemma (Astrom [15]). The recursive computation of the matrix $\mathbf{P}(n)$ requires a number of calculations proportional to I^2 (I is number of parameters). As a consequence the computational effort needed to calculate the RLSE estimation is almost completely dominated by the matrix computation if there are more than 4 parameters. In ANC for periodic noise, the number of parameters to be estimated is about 10 to 20, but can be as high as 100. Therefore the RLSE algorithm is simplified using the so called projection method. Using this method the recursive calculation of the matrix (4.1.11) is avoided.
The method is called projection method because, in a geometric interpretation, the projection on the input vectors $\vec{\varphi}^*(k)$ is essential. The I dimensional vector comprising the actual process parameters $\vec{\theta}$, the vector comprising the estimated parameters $\vec{\theta}_{c,e}(k-1)$ and the input vector $\vec{\varphi}^*(k)$ are considered to be vectors in a complex I

dimensional space. Now assume that the input vectors $\vec{\varphi}^*(k)$, k=1,...n, completely span the I dimensional space, consequently the optimal 'anti' vector $-\vec{\theta}$ can be written as a linear combination of the vectors $\vec{\varphi}^*(k)$. Therefore it is natural to update the estimate $\vec{\theta}_{c,e}(k-1)$ each iteration step in the negative direction of $\vec{\varphi}^*(k)$. To guarantee convergence the length of the update is determined by the *projection* of the 'difference' vector

$$\Delta\vec{\theta}_{c,p}(k-1) = \vec{\theta} + \vec{\theta}_{c,p}(k-1), \tag{4.1.13}$$

on the input vector $\vec{\varphi}^*(k)$. Using the measured error

$$\varepsilon(k) = \vec{\varphi}^H(k)\Delta\vec{\theta}_{c,p}(k-1), \tag{4.1.14}$$

the projection of the 'difference' vector $\Delta\vec{\theta}_{c,p}(k-1)$ on the input vector $\vec{\varphi}(k)$ can be written as the vector

$$\vec{\Delta}(k) = \frac{\vec{\varphi}(k)\varepsilon(k)}{\vec{\varphi}^H(k)\vec{\varphi}(k)}. \tag{4.1.15}$$

The estimate is updated with $-\vec{\Delta}(k)$

$$\vec{\theta}_{c,p}(k) = \vec{\theta}_{c,p}(k-1) - \vec{\Delta}(k). \tag{4.1.16}$$

In figure 4.1.3 the procedure is depicted for a two dimensional situation (the vectors are taken real for convenience).

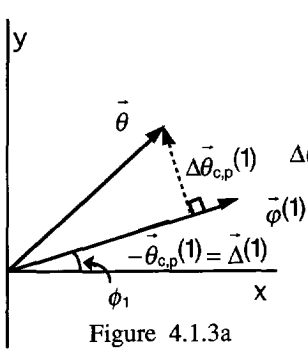

Figure 4.1.3a

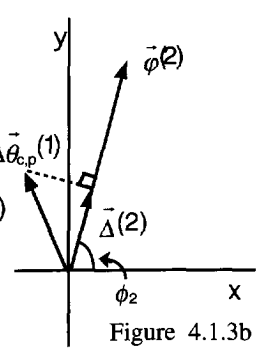

Figure 4.1.3b

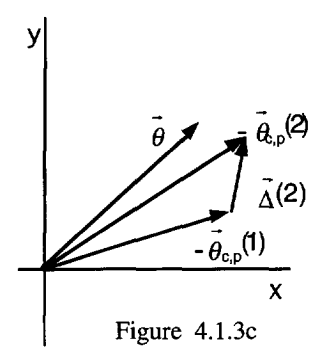

Figure 4.1.3c

a) *Assuming that* $\vec{\theta}_{c,p}(0) = \vec{0}$, *the equations (4.1.13) to (4.1.16) for k=1 yield* $\vec{\theta}_{c,p}(1) = -\vec{\Delta}(1)$. *Using this,* $\Delta\vec{\theta}_{c,p}(1)$ *is found with the help of (4.1.13) for k=2.*
b) *Using (4.1.14) and (4.1.15) for k=2,* $\vec{\Delta}(2)$, *the projection of* $\Delta\vec{\theta}_{c,p}(1)$ *on* $\vec{\varphi}(2)$, *can be calculated.* **c)** *Equation (4.1.16) for k=2 yields* $\vec{\theta}_{c,p}(2)$. *All vectors are real in this example. Note that* $-\vec{\theta}_{c,p}(2)$ *is a better approximation for* $\vec{\theta}$ *than* $-\vec{\theta}_{c,p}(1)$.

The updating formula is known as Kaczmarz's projection algorithm. Note that only the most recent input vector and the most recent error is used in the algorithm. The difference vector $\Delta\vec{\theta}_{c,p}(1)$ drawn in figure 4.1.3a is perpendicular to the input vector $\vec{\varphi}(1)$. As a consequence the optimal estimate is found within 2 steps if $\vec{\varphi}(2)$ is perpendicular to $\vec{\varphi}(1)$. This has implications for an I dimensional space. In an I dimensional space the optimal anti-noise vector is found within I steps if the input vectors $\vec{\varphi}^*(k)$, k=1,..I, form an orthogonal base for the I dimensional space. If, on the other hand, the vectors $\vec{\varphi}^*(k)$ are independent, but all point more or less in the same direction, many steps are needed to find the solution.
An important quantity in studying the rate of convergence of the projection algorithm is the *eigenvalue spread* of the normalized input correlation matrix, defined as

$$\Phi_n^H(n)\Phi_n(n) = \sum_{k=1}^{n} \frac{\vec{\varphi}(k)\vec{\varphi}^H(k)}{\vec{\varphi}^H(k)\vec{\varphi}(k)}. \qquad (4.1.17)$$

The rate of convergence decreases if the eigenvalue spread, the ratio of the maximum eigenvalue to the minimum eigenvalue of the matrix (4.1.17), increases (Widrow[14], Haykin [16]). Besides that, the sensitivity of the eigenvalues to perturbations in the matrix increases with the condition number of the matrix (Noble [17]).
In the 2 dimensional example depicted in figure 4.1.3 the eigenvalue spread of two input vectors is determined by the intermediate angle $\phi_2 - \phi_1$: $\lambda_{1,2} = 1 \pm \cos(\phi_2 - \phi_1)$ (appendix C). For the two input vectors shown in the figure the eigenvalue spread is approximately 3.
It can be proven that if I input vectors form an orthogonal basis of the I dimensional space, the eigenvalue spread of the matrix (4.1.17) is 1 at n=I. The eigenvalue spread of a matrix composed of independent input vectors all pointing more or less in the same direction is large.

4.1.3 Time-varying primary process parameters and extraneous noise

So far, the process parameter vector $\vec{\theta}$ is assumed to be constant. In the ANC applications mentioned in the introduction of this chapter, the primary process however alters in time due to variations in the revolution frequency of the main shaft and due to changes in the acoustic environment. The assumption is made that those variations are slow, that is to say the changes in the process parameter vector are small during one period of the primary signal. A change in the time variant actual process parameter $\vec{\theta}(k)$ will simply change the length of the 'difference' vector 4.1.13 in the ensuing step. As long as the alteration in the process vector is smaller than the change in the estimate, the estimation converges, although of course the estimate is always one step behind. This can be made clear with the help of figure 4.1.4, depicting the situation shown in figure 4.1.3c while $\vec{\theta}(2) \neq \vec{\theta}(1)$. The calculation of the estimate $\vec{\theta}_{c,p}(2)$ is based on the previous

process vector (see figures 4.1.3), the calculation of the new estimate $\vec{\theta}_{c,p}(3)$ however will be based on the new actual process vector $\vec{\theta}(2)$. Thus the estimate will always follow the alterations in the actual process.

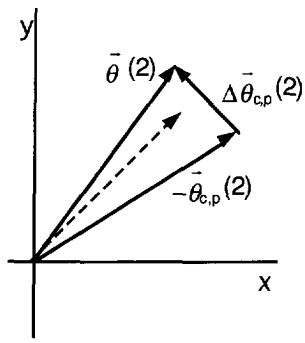

Figure 4.1.4 ; *The difference vector* $\Delta\vec{\theta}_c(2)$ *after a change in the actual process parameter vector. The previous parameter vector is shown with a dotted line.*

The influence of non-correlated, extraneous noise on the projection algorithm has been neglected so far. In most applications however the measured error signal is perturbed with extraneous noise. As a result the lengths of the estimated projections given by equation (4.1.15) will not be calculated properly. In order to decrease the influence of these 'noisy' projections on the estimated parameters, the lengths and so the influence of the extraneous noise can be reduced using a step size factor, resulting in the modified algorithm

$$\vec{\theta}_{c,p}(n) = \vec{\theta}_{c,p}(n-1) - \gamma \frac{\vec{\varphi}(n)\varepsilon(n)}{\vec{\varphi}^H(n)\vec{\varphi}(n)},$$

and $0 < \gamma \leq 1$. It will be clear that the number of steps, needed to find the actual process vector, increases when the step size factor decreases. A second modification is made to stabilize the calculated projection (4.1.15), since it is not unthinkable that the denominator becomes very small. A small real constant α is added, resulting in the algorithm

$$\vec{\theta}_{c,p}(n) = \vec{\theta}_{c,p}(n-1) - \gamma \frac{\vec{\varphi}(n)\varepsilon(n)}{\alpha + \vec{\varphi}^H(n)\vec{\varphi}(n)}. \qquad (4.1.19)$$

The properties of the modified projection algorithm can be found in appendix C and Astrom [15]. Some authors refer to the algorithm as Normalized Least Mean Squares (NLMS, Widrow [14], Haykin [16]).

4.1.4 The input vector and process model

In this section two types of input vectors and the related process models are mentioned: the single, time input with which the FIR coefficients are estimated and the Fourier inputs with which the Fourier coefficients are estimated. Since the input correlation matrix is defined by the input vector, the rate of convergence and the stability of the estimation process are determined by the choice of the input vector.

The time input vector

The components of the time input vector are at t=kΔt

$$\vec{\varphi}_t^*(k) \quad = \quad [\varphi(k) \;\; \varphi(k-1) \;\; \cdots \;\; \varphi(k-I+1)]^H. \tag{4.1.20}$$

The input-output relation of the controller is in that case a *convolution* of the complex conjugate of the time signal $\varphi(k)$ with the controller parameter vector $\vec{\theta}_c^t(k-1)$:

$$y_s(k) = \vec{\varphi}_t^H(k)\vec{\theta}_c^t(k-1) = \sum_{i=0}^{I-1} \varphi^*(k-i)\theta_{c,i}^t(k-1) \tag{4.1.21}$$

In figure 4.1.4 a controller based on the convolution is depicted. The model is also called a tapped delay line, each 'tap' representing one sample delay, so the controller might be called a 'time delay controller'. The parameters $\theta_{c,i}^t(k-1)$ are updated according to the projection algorithm (4.1.19).
The minimum number of complex parameters is equal to the number of frequency components (appendix C), so $I \geq N$.

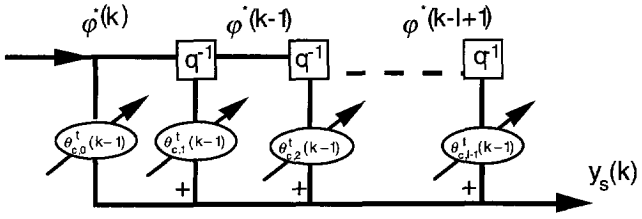

4.1.4 ; *A controller in which the output is the result of a convolution of the input signal with the controller parameters.*

The eigenvalue spread and condition number of the input correlation matrix strongly depend on the relation of one period of the input signal to the length of the total delay.

Using the composed input signal (4.0.2), the eigenvalue spread is optimal for the frequencies present in the signal if the total time delay covers one period of this signal (appendix C) but strongly increases for shorter lengths. The condition number is in general large.

The Fourier input vector

The components of an N dimensional Fourier input vector are at $t=k\Delta t$:

$$\vec{\varphi}_f^*(k) = [\varphi_1(k)\ \varphi_2(k)\ \cdots\ \varphi_N(k)]^H. \tag{4.1.22}$$

The input-output relation of the controller is in that case a *multiplication* of the complex conjugate of the signal values $\varphi_v(k)$, $v = 1,....,N$ with the controller parameters gathered in the vector $\vec{\theta}_c^f(k-1)$

$$y_s(k) = \vec{\varphi}_f^H(k)\vec{\theta}_c^f(k-1) = \sum_{v=1}^{N} \varphi_v^*(k-i)\theta_{c,v}^f(k-1) \tag{4.1.23}$$

In figure 4.1.5 a controller based on the multiplication is depicted. The parameters $\theta_{c,v}^f(k-1)$ are updated according to the projection algorithm (4.1.19).
Since the input *signals* (and not the input vectors) are orthogonal the eigenvalue spread and the condition number of the input correlation matrix of the 'Fourier' controller is already are 1 after one period of the composed signal given by (4.0.2). Hence, it may be expected that, compared to a time delay controller, the convergence rate of a Fourier controller will in general be larger.

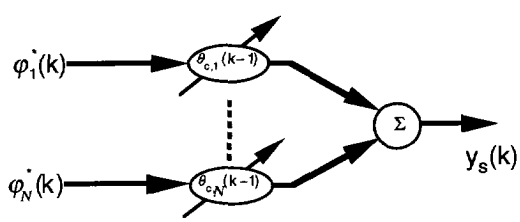

Figure 4.1.5 ; *A controller in which the output is the result of a multiplication of the input signals with the controller parameters.*

A special case of a Fourier controller is the block-based Fourier controller. In such a controller the parameters to be estimated also are the Fourier coefficients of the optimal output signal. The Fourier coefficients determining the controller output signal however are not updated after each sample, but each time after a block of samples. The procedure is performed in three steps. First a Fourier transform is carried out on blocks of samples of the input signal and on blocks of the error signal, so a control loop in the frequency

domain can be created for each frequency component individually (figure 4.1.6). After that, the optimal parameters for each control loop are calculated individually in the frequency domain. In the last step the output signal is calculated using an inverse Fourier transformation.
The input variables of a block **m** are the Fourier coefficients of one period T_0 of the input signal. Using upper case symbols for the Fourier coefficients, the inputs of block **m** are

$$X_\nu(m)=\Delta f X(m, \nu\Delta f)$$

and $\Delta f = \frac{1}{T_0}$. The input-output relation is again a multiplication

$$Y_{s,\nu}(m) = \Theta_\nu(m)X_\nu(m). \qquad (4.1.24)$$

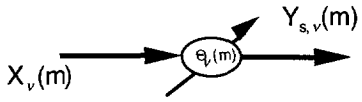

Figure 4.1.6 *; Each input of the block based Fourier controller is multiplied with a controller parameter.*

4.2 The anti-noise control loop

In ANC the general principles of linear control are used to find adaptively the anti-noise signal. However, the general (closed) loop configuration as depicted in figure 4.1.2 has to be modified because of the presence of the *secondary process*, the partly acoustic process from controller output to the error input.

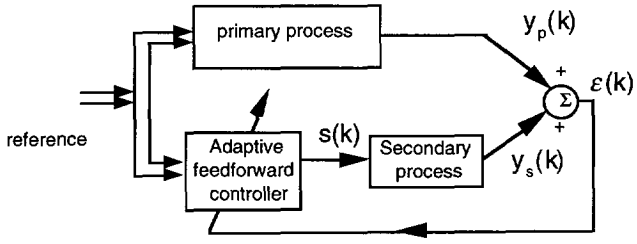

Figure 4.2.1 ; *Block diagram of the ANC feedforward configuration.*

In the first part of this section a single-channel anti-noise control loop will be discussed. The controller in a single channel control loop only has one controller output and only one error input. In figure 4.2.1 a single channel system is shown. In the second part of

this section a multi-channel control loop will be considered. In a multi-channel control loop there are more error inputs and possibly more controller outputs.
In the derivations it will be assumed that the primary process and the secondary process are linear.

4.2.1 Single channel control in ANC

In the previous section it was made clear that the output signal $s(k)$ $(k=1,...n)$ of a linear controller can be written as

$$s(k) = \vec{\varphi}^H(k)\vec{\theta}_c(k-1), \tag{4.2.1}$$

in which $\vec{\varphi}^H(k)$ is the vector comprising the controller input values and $\vec{\theta}_c(k-1)$ is the vector containing the most recent controller parameters.
Assume that the time invariant *secondary* process can be modelled as a finite impulse response (FIR) having the coefficients h_j, then the output of the secondary process can be written as a convolution of the controller output and the finite impulse response

$$y_s(k) = \sum_{j=0}^{J-1} h_j s(k-j). \tag{4.2.2}$$

The measured error is $\varepsilon(k) = y_p(k) + y_s(k)$, hence for a time delay controller

$$\varepsilon(k) = y_p(k) + \sum_{j=0}^{J-1} h_j \sum_{i=0}^{I-1} \varphi^*(k-j-i)\theta_{c,i}(k-j-1), \tag{4.2.3}$$

while for a sample based Fourier controller the measured error is

$$\varepsilon(k) = y_p(k) + \sum_{j=0}^{J-1} h_j \sum_{\nu=1}^{N} \varphi_\nu^*(k-j)\theta_{c,\nu}(k-j-1). \tag{4.2.4}$$

An important assumption is made to simplify the estimation problem to what is known as the filtered-x-configuration (Widrow [14], he uses the symbol x for the input). It is assumed that by taking the step size factor γ small, the change in the estimated parameters is small during the length of the FIR (J samples), so

$$\theta_{c,i}(k-1-j) \approx \theta_{c,i}(k-1) \quad \text{for} \quad j = 0,\ldots,J-1, \tag{4.2.5}$$

and thus, for a time delay controller

$$\varepsilon(k) \approx y_p(k) + \sum_{i=0}^{I-1} \theta_{c,i}(k-1) \sum_{j=0}^{J-1} h_j \varphi^*(k-j-i), \tag{4.2.6}$$

and for a Fourier controller,

$$\varepsilon(k) \approx y_p(k) + \sum_{v=1}^{N} \theta_{c,v}(k-1) \sum_{j=0}^{J-1} h_j \varphi_v^*(k-j). \tag{4.2.7}$$

Both equations can be written in the vector notation

$$\varepsilon(k) \approx y_p(k) + \vec{r}^H(k)\vec{\theta}_c(k-1). \tag{4.2.8}$$

The vector

$$r_i(k) = \sum_{j=0}^{J-1} h_j^* \varphi(k-j-i), \tag{4.2.9}$$

or

$$r_v(k) = \sum_{j=0}^{J-1} h_j^* \varphi_v(k-j), \tag{4.2.10}$$

is called the filtered-x signal. In figure 4.2.2 the process is depicted.
Hence, if the secondary path is known, for small step size factors the problem is reduced to a general linear control configuration. Using the projection algorithm (4.1.15), the controller parameters in a filtered-x configuration are updated according to

$$\vec{\theta}_c(k) = \vec{\theta}_c(k-1) - \gamma \frac{\vec{r}(k)\varepsilon(k)}{\alpha + \vec{r}^H(k)\vec{r}(k)}. \tag{4.2.11}$$

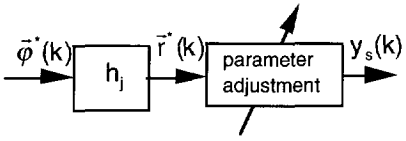

Figure 4.2.2a ; *The configuration which is used to calculate the parameters. It is assumed that the actual values of* h_j *are known.*

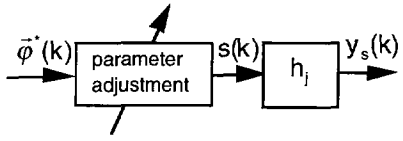

Figure 4.2.2b ; *The actual configuration: the parameters are updated with the help of figure 4.2.2a.*

The normalized input correlation matrix of the filtered-input configuration is for **k=1,...n,**

$$\sum_{k=1}^{n} \frac{\vec{r}(k)\vec{r}^H(k)}{\vec{r}^H(k)\vec{r}(k)}. \tag{4.2.12}$$

The eigenvalue spread of this matrix strongly depends on the input vectors, and will in general not be optimal. For the Fourier controller the eigenvalue spread of the matrix can

be optimized simply if the matrix is diagonal, so if the dot products

$$\sum_{k=1}^{n} r_{\nu}^{*}(k) r_{\kappa}(k), \quad \kappa \neq \nu, \tag{4.2.13}$$

are negligibly small compared to the diagonal elements

$$\sum_{k=1}^{n} r_{\nu}^{*}(k) r_{\nu}(k), \tag{4.2.14}$$

in other words, if the signals $r_{\nu}(k)$ and $r_{\kappa}(k)$ may be considered to be independent. Although independency can only be proven for $n \rightarrow \infty$, it is reasonable to assume that for the Fourier controller the dot products (4.2.13) are negligible after a few periods. If the input signal and the secondary process are stationary during this time interval, then

$$r_{\nu}^{*}(k) r_{\nu}(k) = r_{\nu}^{*}(0) r_{\nu}(0),$$

and, as a consequence the input correlation matrix reduces to the diagonal matrix

$$\frac{1}{\sum_{\nu=1}^{N} r_{\nu}^{*}(0) r_{\nu}(0)} \begin{bmatrix} r_1^{*}(0) r_1(0) & 0 & \cdots & 0 \\ 0 & \ddots & \ddots & \vdots \\ \vdots & \ddots & \ddots & 0 \\ 0 & \cdots & 0 & r_N^{*}(0) r_N(0) \end{bmatrix}. \tag{4.2.15}$$

It will be clear that the eigenvalue spread of this matrix will be optimal if in the updating algorithm (4.2.11) the parameters $\theta_{c,\nu}(k)$ are scaled with a factor

$$\frac{r_{\nu}^{*}(k) r_{\nu}(k)}{\sum_{\nu=1}^{N} r_{\nu}^{*}(k) r_{\nu}(k)}, \tag{4.2.16}$$

resulting in the algorithm

$$\theta_{c,\nu}(k) = \theta_{c,\nu}(k-1) - \gamma \frac{r_{\nu}(k) \varepsilon(k)}{\left(\alpha + r_{\nu}^{*}(k) r_{\nu}(k)\right)}. \tag{4.2.17}$$

Convergence of the algorithm is only guaranteed for small values of the step size factor, the maximum value is inversely proportional to the number of samples in one period of the output signal. Since the step size factor is already bounded by (4.2.5), this restriction does not affect in practice the maximum convergence rate. In practice the measured error is scaled with N, the number of frequencies, leading to similar values of the step size

factor if the number of frequencies to be estimated is varied.
It is important to note that equation (4.2.17) would have been found too, if it is assumed that the momentary 'dot-product' $r_\nu^*(k)r_\kappa(k) \approx 0$, for $\nu \neq \kappa$. Using this assumption, the error equation (4.2.8) can be transferred into

$$r_\nu(k)\varepsilon(k) \approx r_\nu(k)y_p(k) + r_\nu(k)r_\nu^*(k)\theta_{c,\nu}(k-1), \tag{4.2.18}$$

resulting in the alternative error equation

$$\frac{r_\nu(k)}{r_\nu(k)r_\nu^*(k)}\varepsilon(k) \approx \frac{r_\nu(k)}{r_\nu(k)r_\nu^*(k)}y_p(k) + \theta_{c,\nu}(k-1). \tag{4.2.19}$$

The application of the projection algorithm to this error equation will lead to the result (4.2.17). In the derivation of the optimal algorithm for the multi channel controller this will prove to be very helpful.
For a Fourier controller in which the coefficients of a block of samples are calculated using a FFT on the input signals (figure 4.1.6), the filtered-x-inputs of sample block m are

$$R_\nu(m) = H_\nu X_\nu(m), \quad \nu = 1,\ldots N, \tag{4.2.20}$$

while the controller parameters are updated according to

$$\Theta_\nu(m) = \Theta_\nu(m-1) - \gamma\frac{R_\nu^*(m)E_\nu(m)}{\alpha + |R_\nu(m)|^2}. \tag{4.2.21}$$

4.2.2 Multi channel controllers

In an active noise control system for a three dimensional situation several anti-noise sources and error sensors are used. The projection algorithm applied to the filtered-x configuration for a multi channel controller can be derived with the help of the equations for a single channel controller. If there are M sensors, the cost function (4.1.6) is modified to

$$J(\vec{\theta}_c) = \tfrac{1}{2}\sum_{k=1}^{n}\sum_{m=1}^{M} e_m^H(k)e_m(k). \tag{4.2.22}$$

The signal of source ℓ is given by

$$s_\ell(k) = \vec{\varphi}_\ell^H(k)\vec{\theta}_c^\ell(k). \tag{4.2.23}$$

So, for L anti-noise sources the measured error on sensor m is

$$\varepsilon_m(k) = y_{p,m}(k) + \sum_{\ell=1}^{L}\sum_{j=0}^{J-1} h_j^{\ell,m} s_\ell(k-j), \tag{4.2.24}$$

in which $y_{p,m}(k)$ is the primary noise on sensor m. The coefficients of the time invariant finite impulse response describing the transfer function from source output ℓ to sensor input m are $h_j^{\ell,m}$. Similar to single channel control, filtered input signals are used

$$r_{i,\ell,m}^{*}(k) = \sum_{j=0}^{J-1} h_j^{\ell,m} \varphi_\ell^{*}(k-i-j), \text{ (time delay)} \tag{4.2.25}$$

and

$$r_{v,\ell,m}^{*}(k) = \sum_{j=0}^{J-1} h_j^{\ell,m} \varphi_{v,\ell}^{*}(k-j), \text{ (sample based Fourier).} \tag{4.2.26}$$

In order to simplify the notation vectors are used. For a time delay controller the parameters $\theta_{c,i}^{t,\ell}(k)$ are gathered in one vector of length IL

$$\vec{\theta}_{c_L}^{t}(k) = \left[\theta_{c,0}^{t,1}(k) \;\cdots\; \theta_{c,0}^{t,L}(k) \;\cdots\; \theta_{c,I-1}^{t,1}(k) \;\cdots\; \theta_{c,I-1}^{t,L}(k)\right]^T, \tag{4.2.27}$$

and the filtered-x values $r_{i,\ell,m}(k)$ are collected in M (I*L) vectors

$$\vec{r}_m(k) = \left[r_{0,1,m}(k) \;\cdots\; r_{0,L,m}(k) \;\ldots\ldots\; r_{I-1,1,m}(k) \;\cdots\; r_{I-1,L,m}(k)\right]^T. \tag{4.2.28}$$

For the Fourier controller the parameters $\theta_{c,v}^{t,\ell}(k)$ are gathered in one vector

$$\vec{\theta}_{c_L}^{t}(k) = \left[\theta_{c,1}^{t,1}(k) \;\cdots\; \theta_{c,1}^{t,L}(k) \;\cdots\; \theta_{c,N}^{t,1}(k) \;\cdots\; \theta_{c,N}^{t,L}(k)\right]^T, \tag{4.2.29}$$

and the filtered-x values $r_{v,\ell,m}(k)$ are collected in M vectors

$$\vec{r}_m(k) = \left[r_{1,1,m}(k) \;\cdots\; r_{1,L,m}(k) \;\ldots\ldots\; r_{N,1,m}(k) \;\cdots\; r_{N,L,m}(k)\right]^T. \tag{4.2.30}$$

The measured error on sensor m now can be written for both controllers as

$$\varepsilon_m(k) \approx y_{p,m}(k) + \vec{r}_m^{H}(k)\vec{\theta}_{c_L}(k-1). \tag{4.2.31}$$

The error vector is

$$\vec{\varepsilon}(k) = \begin{pmatrix} \varepsilon_1(k) \\ \vdots \\ \varepsilon_M(k) \end{pmatrix} \approx \vec{y}_p(k) + \mathbf{R}^{H}(k)\vec{\theta}_{c_L}(k-1), \tag{4.2.32}$$

in which $\vec{y}_p(k) = \left(y_{p,1}(k) \quad \cdots \quad y_{p,M}(k)\right)^T$ and $\mathbf{R}(k) = \left(\vec{r}_1(k) \quad \cdots \quad \vec{r}_M(k)\right)$. Note that the matrix $\mathbf{R}(k)\mathbf{R}^H(k)$ is singular if $M<IL$ (or $M<NL$).

In all M measured errors, the most recent parameter vector is $\vec{\theta}_{c_L}(k-1)$. For the time delay controller which is used in the measurements the new vector is found applying the projection algorithm to each of the M error equations, yielding

$$\vec{\theta}^t_{c_L}(k) = \vec{\theta}^t_{c_L}(k-1) - \gamma \sum_{m=1}^{M} \frac{\vec{r}_m(k)\varepsilon_m(k)}{\vec{r}^H_m(k)\vec{r}_m(k)}. \tag{4.2.33}$$

In this multi channel configuration the normalized input correlation matrix is given by

$$\sum_{k=1}^{n}\sum_{m=1}^{M} \frac{\vec{r}_m(k)\vec{r}^H_m(k)}{\vec{r}^H_m(k)\vec{r}_m(k)}. \tag{4.2.34}$$

The eigenvalue spread of this matrix strongly depends on the mutual relation of the filtered input signals and generally will not be optimal.

The eigenvalue spread of the Fourier controller however can be optimized assuming that the signals $r_{\nu,\ell_1,m_1}(k)$ and $r_{\kappa,\ell_2,m_2}(k)$ are independent for all values of ℓ_1, ℓ_2 and m_1, m_2 $(\kappa \neq \nu)$.

Using the L dimensional vectors $\vec{\theta}_{c,\nu}(k) = \left[\theta^1_{c,\nu}(k) \quad \cdots \quad \theta^L_{c,\nu}(k)\right]^T$,

and the LxM matrices $\mathbf{R}_\nu(k) = \begin{bmatrix} r_{\nu,1,1}(k) & \cdots & r_{\nu,1,M}(k) \\ \vdots & \ddots & \vdots \\ r_{\nu,L,1}(k) & \cdots & r_{\nu,L,M}(k) \end{bmatrix}$, $\nu = 1,\ldots N$,

the error vector (4.2.32) can be written in the form

$$\vec{\varepsilon}(k) \approx \vec{y}_p(k) + \sum_{\nu=1}^{N}\left[\mathbf{R}^H_\nu(k)\vec{\theta}_{c,\nu}(k-1)\right]. \tag{4.2.35}$$

Bearing in mind the derivations in the previous section, it is assumed that the momentary dot-product equals zero

$$r^*_{\nu,\ell_1,m_1}(k)r_{\kappa,\ell_2,m_2}(k) \quad = \quad 0, \tag{4.2.36}$$

for all values of ℓ_1, ℓ_2 and m_1, m_2, and $\kappa \neq \nu$, so $\mathbf{R}_\nu(k)\mathbf{R}^H_\kappa(k) = \mathbf{0}$.

As a result for each frequency component an alternative error equation can be formulated. Since

$$\mathbf{R}_\nu(k)\vec{\varepsilon}(k) \approx \mathbf{R}_\nu(k)\vec{y}_p(k) + \mathbf{R}_\nu(k)\mathbf{R}^H_\nu(k)\vec{\theta}_{c,\nu}(k-1), \tag{4.2.37}$$

and provided that $\mathbf{R}_\nu(k)\mathbf{R}^H_\nu(k)$ is not singular, the new error equation is

$$\left[\mathbf{R}_v(k)\mathbf{R}_v^H(k)\right]^{-1}\mathbf{R}_v(k)\vec{\varepsilon}(k) \approx \left[\mathbf{R}_v(k)\mathbf{R}_v^H(k)\right]\mathbf{R}_v(k)\vec{y}_p(k) + \vec{\theta}_{c,v}(k-1), \qquad (4.2.38)$$

leading to the updating algorithm for the Fourier controller

$$\vec{\theta}_{c,v}(k) = \vec{\theta}_{c,v}(k-1) - \gamma\left[\mathbf{R}_v(k)\mathbf{R}_v^H(k)\right]^{-1}\mathbf{R}_v(k)\vec{\varepsilon}(k). \qquad (4.2.39)$$

In this algorithm the values of the step size factor are restricted too, the maximum value being determined by the number of samples in one period of the output signal. In practice the measured error is scaled with N, the number of frequencies.
The eigenvalue spread of the input correlation matrix linked to the algorithm (4.2.39) is optimal, which means that, contrary to the multi channel algorithm of the time delay controller, the rate of convergence for the Fourier controller does not depend on the position of sources and sensors.

4.3 Active noise control experiments

In a one dimensional wave field, like the wave field in a duct, one anti-noise source is able to reconstruct the (negative) primary wave field and one error sensor suffices to check the result (chapter 2). Therefore a single channel ANC system can be used to reduce actively a one dimensional wave field. The anti-noise signal is generated by a loudspeaker while the error signal is measured by a microphone. Since these signals are real time functions, the algorithms in the previous section have to be modified somewhat. In the first part of this section these modifications will be given. Then the behaviour of a single channel anti-noise system based on the projection algorithm will be examined with the help of the results of a number of experiments in the laboratory. Experiments are carried out with all three different inputs mentioned in section 4.1.
In a three dimensional situation more anti-noise sources and sensors are needed (chapter 3). In the last part of this section some results of measurements with multi-channel ANC systems will be discussed. The derivations of the multi-channel controllers for real time signals are not given, since they can be found directly with the help of section 4.2 and the following derivations for single channel controllers.

4.3.1 Single channel controllers

Single channel controllers are mainly used for the reduction of one dimensional wave fields, like the wave field in a duct. In a one dimensional wave field one anti-noise source is able to reconstruct the (negative) wave field and only one error microphone is needed to measure the result.
The microphone and loudspeaker signals are real, so using the filtered-x assumption

(4.2.5), the measured error is

$$\varepsilon(k) \approx \mathrm{Re}\left[y_p(k)\right] + \mathrm{Re}\left[\sum_{i=0}^{I-1} r_i^*(k)\theta_{c,i}(k-1)\right]. \tag{4.3.1}$$

Consider a single input signal given by equation (4.0.2),

$$\varphi(k) = \sum_{v=1}^{N} \exp(j2\pi f_v k\Delta t). \tag{4.3.2}$$

Combination of this signal with a tapped delay (figure 4.1.4) gives the filtered input signal

$$r_i(k) = \sum_{j=0}^{J-1} h_j^* \sum_{v=1}^{N} \exp(j2\pi f_v(k-j-i)\Delta t)). \tag{4.3.3}$$

Note that with this type of configuration, the computational effort can be reduced considerably using

$$r_{i+1}(k) = r_i(k-1). \tag{4.3.4}$$

The controller parameters are updated according to equation (4.2.11) (appendix C).
In a simplified form the time delay controller is often used with a *real* input :

$$\varphi(k) = \sum_{v=1}^{N} \cos(2\pi f_v k\Delta t). \tag{4.3.5}$$

As a consequence all imaginary parts of the signals are zero, and the estimation problem only contains real numbers. Since the behaviour of a *real* time delay controller does not deviate much from the behaviour of a *complex* time delay controller, all experiments are carried out with a real time delay controller.
For a sample based Fourier controller (figure 4.1.5), the filtered input signals are

$$r_v(k) = \sum_{j=0}^{J-1} h_j^* \exp(j2\pi f_v(k-j)\Delta t)), \tag{4.3.6}$$

while the controller parameters are updated according to equation (4.2.17).
In the block based Fourier controller the equations (4.2.20) and (4.2.21) are used.

4.3.2 Experiments with single channel ANC

The behaviour of an anti-noise controller can be characterized by its rate of *convergence*, its *performance* and its *stability*. The rate of convergence is linked with the eigenvalue spread of the input correlation matrix and can be varied with the step size factor. The

maximum step size factor is bounded by the total delay of the secondary process (equation (4.2.5) must be valid) and the extraneous noise. The performance, or overall reduction, strongly depends on the rate of convergence for systems which change in time: if the rate of convergence is small the controller cannot track the alterations . The stability is linked with the condition number of the input correlation matrix. Experiments are carried out to examine the behaviour of a single channel system for the three inputs mentioned in section 4.1 (time delay, sample-Fourier and block-Fourier). The input correlation matrices based on the filtered input signals are calculated and their eigenvalues and condition number are compared with respectively the rate of convergence and the stability of the controller.
In the experiments two set-ups are used: a set-up in which the noise source, anti-noise source and the error-sensor are placed in an anechoic room, and a set-up in which the noise source, the anti-noise source and the error sensor are placed in a duct. The impulse responses of the primary and secondary process are assumed to be time invariant. The FIR of the secondary process, truncated to 150 points, is measured in both set-ups before operation with the help of broad band noise. The sampling frequency used in the controller is 2 kHz. The input signals are produced by wave form generators. In figure 4.3.1 the set-ups are depicted (see also figure 4.1.3).

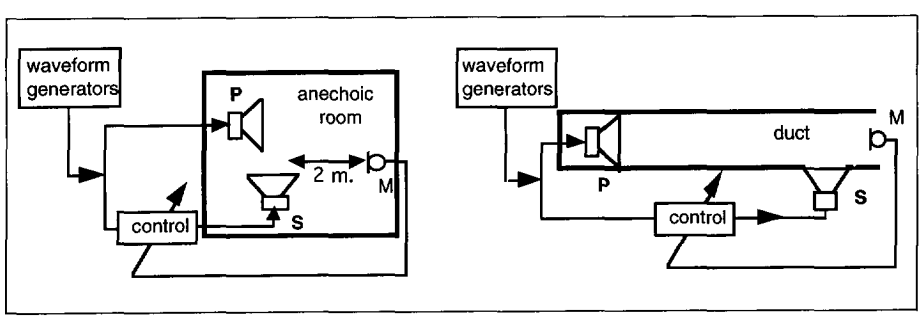

Figure 4.3.1 ; *The single channel set-up in the anechoic room and in the duct .*

The error sensor signal is measured as a function of time, and the results are shown in graphs in which the level of the error signal, averaged over 100 samples is drawn.
In a first experiment the set-up in the anechoic room is used. The distance between the secondary source and the error-sensor is 2 meters. The total delay caused by this acoustical path, filters and loudspeakers is about 25 samples. After about 35 samples the FIR of the secondary process may be truncated. Five wave form generators create signals comprising the following frequency components: f_1=55 Hz, f_2=110 Hz, f_3=165 Hz, f_4=220 Hz and f_5=275 Hz. At a sample frequency of 2 kHz one period of the composed signal having a fundamental frequency of 55 Hz runs to just over 36 samples.
The tapped delay line of the time delay controller comprises 32 samples, nearly one period. The filtered-x vector is found with equation (4.3.3), while the 32 controller parameters are updated according to (4.2.11). The eigenvalue spread of the 5 largest

complex eigenvalues of the matrix (4.2.12) is approximately 8. The calculated condition number is very large (10^{13}).
Both the sample- and the block based Fourier controller have 5 complex parameters, one for each frequency component. The block based Fourier controller has a block size of 64 samples and a sample frequency of 880 Hz. The coefficients are calculated with the help of the scaled projection algorithms, equation (4.2.21) for the block based Fourier controller and equation (4.2.17) for the sample based controller. The condition number and eigenvalue-spread are 1 for both controllers, which means that the convergence rate of the Fourier only is bounded by the delay.
In all cases the maximum step size factor is used for which the algorithm is stable during the experiment (at least about 5 minutes anti-noise).
In figure 4.3.2. the results of the measurements with the three different inputs configurations are depicted. At t=0.2 s. the active noise controller is started.

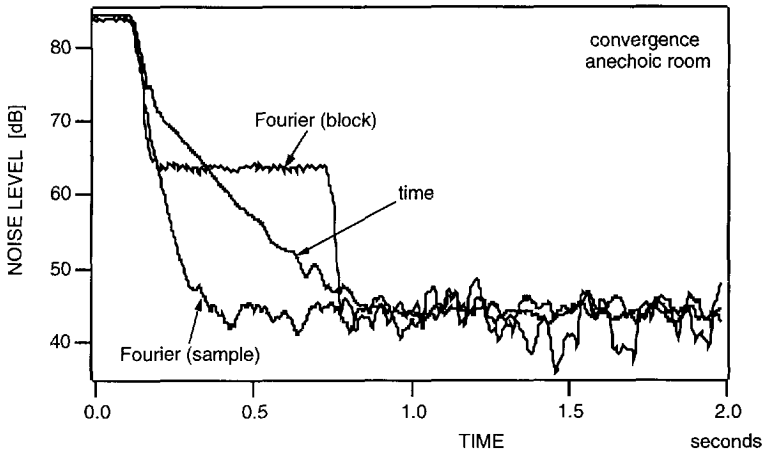

Figure 4.3.2 ; *The level of the measured error during convergence for three different input configurations in the anechoic room.*

The graphs in figure 4.3.2 show that the relation of the convergence rates of the sample based Fourier controller to that of the time delay controller is in agreement with their eigenvalue spread. Also the typical outcome of the block operation used in the block based Fourier controller can be seen in the figure. The eventual reduction (or: performance) of the controllers is the same. The background noise level is found at approximately 40 dB in this measurement. It is affected by the relatively high level of (very) low frequency noise.
In a second experiment the set-up in the duct is used. In this experiment only the time delay controller and the sample based Fourier controller are considered. The length of the duct is 4 m. Due to the multiple reflections in the duct the impulse response in the duct is longer than in the anechoic room, all 150 elements of the impulse response are needed to

calculate the filtered input signal. The convergence of the error signal to the noise level is measured for two different primary signals: the signal comprising 5 frequency components, mentioned above, and a signal comprising 8 harmonic frequency components ranging from 32 Hz to 256 Hz. The sampling frequency is 2 kHz. In the time delay controller for both signals 32 tap elements are used, which means that the convolution filter for the second signal is rather short compared to one period (62 samples). The spread of the 5 largest eigenvalues for the first input signal has, due to the acoustic transfer in the duct, increased to 20, the condition number is approximately 10^9. The eigenvalue spread of the largest 8 eigenvalues for the second signal is about 10^{11} and the condition number is 10^{17}. For the Fourier controller again scaled inputs are used so eigenvalue spread and condition number are 1.

In figure 4.3.3 four noise levels of the error signal (2 primary signals and two controllers) are shown as a function of time. The figure shows that in accordance with the eigenvalue spread the convergence of the time delay controller is rather small for the signal containing 5 components and even smaller for the signal containing 8 harmonics. Compared to the measurement in the anechoic room, the convergence of the Fourier controller is somewhat smaller due to a decrease of the maximum step size factor. This is caused by the somewhat longer impulse response in the duct.

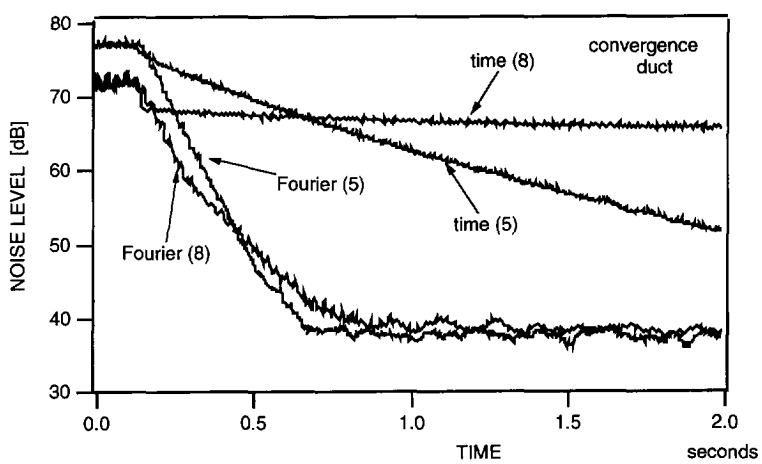

Figure 4.3.3 ; *The level of the measured error during convergence for a Fourier controller and a time delay controller in a duct. Two different primary signals are used.*

In all experiments the calculated condition number of the input correlation matrix of the time delay controller is much larger than the condition number of the Fourier controller. This must have consequences for the stability of the controller. To establish the stability of both controllers an experiment is carried out in which the set-up in the duct is used.

The primary source radiates the signal with the 5 harmonics mentioned above. ANC is switched on and the controllers converge to the noise level according to the figures shown before. Now the time-delay controller, based on convolution, becomes unstable after a few hours. That is to say it calculates an output signal so high that the output-overload protection circuit, which prevents damage on the loudspeakers, switches off the controller. The experiment is repeated several times with the same set-up and each time the controller was switched off automatically by the overload protection circuit after approximately 5 hours. The Fourier controller, having a condition number around 1 did not become unstable at all. After 27 hours (200 million samples) the experiment with the Fourier controller was stopped.

4.3.3 Experiments with multiple channel ANC

In the experiments for multi-channel ANC again two set-ups are used: a set-up in which the noise source, 3 anti-noise sources and 3 error-sensors are placed in the anechoic room, and a set-up in which the noise source, the 3 anti-noise sources and the 3 error sensors are placed in an enclosure (4.3.1). Theoretically a set up with 3 anti-noise sources and 3 sensors should reduce the pressure level on the sensors to the background noise level (chapter 3). The impulse responses of the primary and secondary process are assumed to be time invariant. The FIR model of the 9 secondary processes, truncated to 150 points is measured in both set-ups before operation with the help of broad band noise. The sampling frequency used in the controller is 1 kHz. The periodic primary source signal contains 5 frequency components: f_1=50 Hz, f_2=100 Hz, f_3=150 Hz, f_4=200 Hz and f_5=250 Hz., so one period of the single input signal is 20 samples.
In the time delay controller 22 controller parameters are used, which means that the total delay completely covers one period. The parameters are calculated with the help of the projection algorithm (4.2.33). The Fourier controller contains 5 controller parameters and is calculated with the scaled projection algorithm (4.2.39).

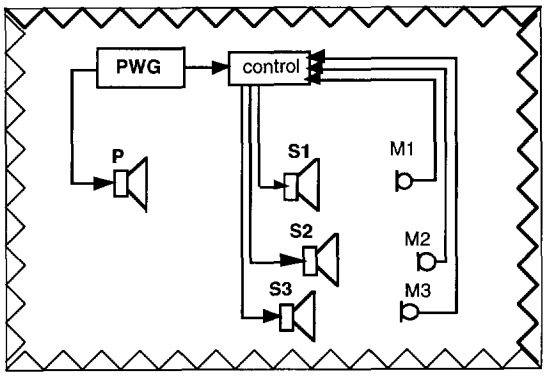

Figure 4.3.4 ; *The multi channel set-up in the anechoic room .*

In the set-up in the anechoic room the distances between sources and sensors are rather short, they range from 0.75 m. to 1.00 m. The impulse responses of the secondary processes are measured and may be considered to be close to a simple delay of about 10 samples for the frequencies from 100 Hz to 300 Hz, so it may be expected that not only the Fourier controller, but also the time delay controller will have an optimal eigenvalue spread.
Since in the time delay controller the total delay completely covers one period the rate of convergence is bounded (for both controllers) by the delay only. In figure 4.3.5 the sum of the squared error signals, averaged over 100 samples, is drawn as a function of time.

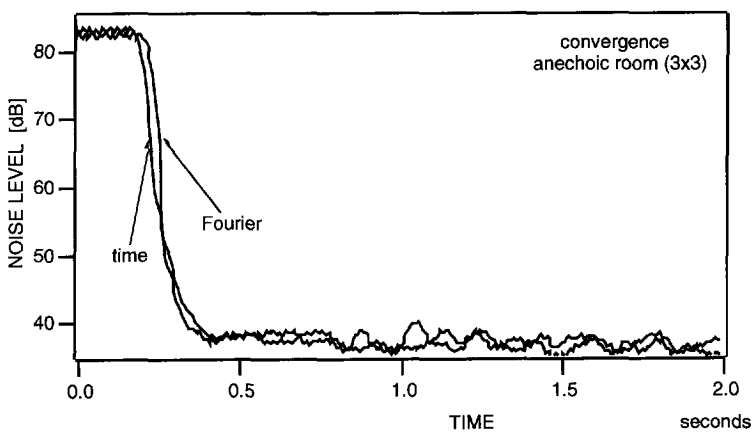

Figure 4.3.5 ; *The level of the sum of the squared errors on the three sensors during convergence for a Fourier controller and a time delay controller in the anechoic room.*

The figure makes clear that the rate of convergence for both controllers is very large, which may be expected considering the optimal eigenvalue spread and the short delay. In both cases the pressure level on the microphones is reduced to the (non correlated) background noise level.
In a second experiment the set-up in the enclosure is used, a rectangular box of dimensions 1.00 m x 0.85 m.x 0.33 m.. The 9 transfer functions from anti-noise sources to error sensors in this set-up strongly depend on the position of the sources, the position of the sensors and, besides that, on the frequency (chapter 3). Since it is not possible to scale the time delay controller, the input correlation matrix given by (4.2.34) will have a large eigenvalue spread. The eigenvalue spread in the set-up in the box was approximately 2500. The eigenvalue spread of the Fourier input matrix is optimal since the scaled projection algorithm is used (4.2.39). The results of the measurements are depicted in figure 4.3.6. The step size factor of the Fourier controller is bounded (section 4.2) and therefore the convergence is not as fast as in the anechoic room. The noise level is reached after approximately one to two seconds. The time delay controller has a rather

typical behaviour: an initial fast convergence after which the rate of convergence decreases gradually. The time delay controller did not reach the background noise level within the measurement time (5 minutes).

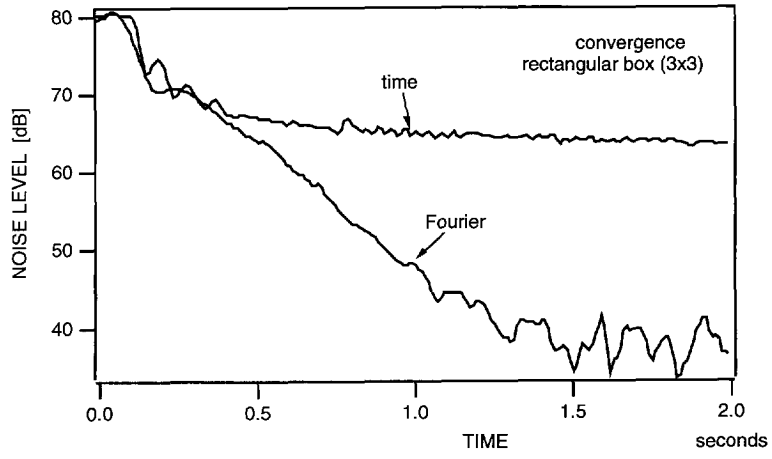

Figure 4.3.6 ; *The level of the sum of the squared errors on the three sensors during convergence for a Fourier and a time delay controller in the rectangular box*

In multi channel control the condition number for the time delay controller is, again, very large. In an experiment for which the 3x3 multi channel set-up was used in a room, the time until the controller becomes unstable is measured. The time delay controller was switched off automatically by the output-overload protection after 140 minutes while the Fourier controller was stable during 27 hours, before being switched off manually.

4.4 Time varying secondary process parameters

In the previous sections the derivation of the projection algorithm was reviewed and it was applied to the anti-noise configuration. In this configuration the so called filtered-x assumption is used in the updating algorithm, and therefore an estimate of the secondary process is needed (equation (4.2.9 and 4.2.10)). So far it was assumed that the secondary process is stationary, which means that it can be measured off-line, before operation of anti-noise. Due to changes in the acoustic environment however the parameters describing the secondary process often alter, and consequently a regular update of these parameters is needed in order to guarantee convergence. This means that besides the configuration in which the controller parameters are estimated (described in the previous sections), an additional controller loop is needed in which the parameters describing the secondary process are estimated. In this additional loop the existing controller output and error input are used. If the primary signal is absent these parameters can be estimated using the most basic configuration (figure 4.1.1), or, in case the

projection algorithm is used, the basic output-error configuration shown in figure 4.1.2 and in figure 4.4.1a.

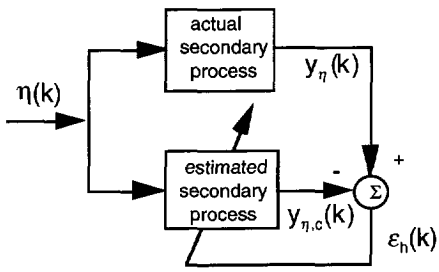

Figure 4.4.1a ; *Off-line estimation.*

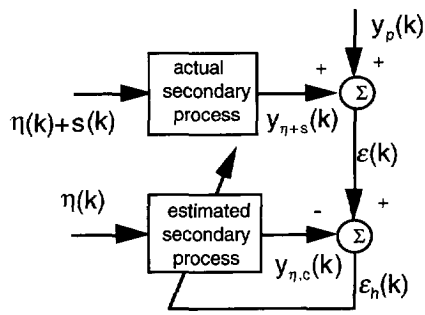

Figure 4.4.1b ; *On-line estimation.*

In ANC the secondary process is described generally with its FIR. For periodic signals however also Fourier coefficients may be used. The FIR of the secondary process is found using a broadband excitation signal $\eta(k)$ as a controller output. This excitation signal is an input of the actual secondary process as well as an input of the estimated secondary process. The outputs of the processes are in that case $y_\eta(k)$ and $y_{\eta,c}(k)$ respectively. Ideally $y_{\eta,c}(k) = y_\eta(k)$. On-line, that is to say, if the primary signal is present, the excitation signal is added to the anti-noise signal. The off-line and on-line configuration are shown in figure 4.4.1a and 4.4.1b. The estimation of the FIR coefficients of a process is much described in literature (for ANC in Eriksson [18] for instance).

If the parameters are estimated on-line, the level of the process output signal $y_\eta(k)$ must be small compared to the primary signal, because it is not desirable to increase the error level audibly. As a consequence the error signal $\varepsilon_h(k)$ comprises much 'extraneous noise' and so the step size factor of the secondary process estimation has to be very small. Furthermore, the FIR generally comprises many elements, especially in a reverberant environment. For those reasons only slow alterations in the parameters can be tracked.

It can be advantageous in some cases to estimate the Fourier coefficients of the secondary process. In the first case because the relatively high level of the anti-noise signal $s(k)$ can be part of the excitation signal. Furthermore, the number of parameters to be estimated is in most cases small: only the Fourier coefficients of the frequency components related to the revolution of the rotating machine have to be estimated. Obviously the method only makes sense in case a block- or sample based Fourier controller is used. An important problem arises using this method since the excitation signal, used to estimate the parameters, and the primary signal are strongly correlated. This correlation is the cause of errors in the estimated values. The correlation can be reduced using *difference* signals: signals which are the difference of two samples of an original signal with a time spacing

of one period (van Overbeek, [19]). In the following section the method to estimate the Fourier coefficients of the secondary process will be reviewed.

4.4.1 On-line estimation of the Fourier coefficients in a block Fourier controller

Assume that the primary signal is stationary having a period of (exactly) p samples. Then the difference signals are:

$$\Delta y_p(k) = y_p(k) - y_p(k-p), \tag{4.4.1}$$

and similarly for $s(k)$, $\varepsilon(k)$ and $y_s(k)$. The sampling interval is Δt.
The time variant secondary process is determined by its impulse response $h_j(k)$, $j=1..J-1$.The time variant Fourier coefficient f_ν of this secondary process is

$$H_\nu(k) = \sum_{j=0}^{J-1} h_j(k) \exp(j2\pi f_\nu j\Delta t). \tag{4.4.2}$$

The application of the estimation method using difference signals is most simple for the Fourier-block based controller. In that case the Fourier coefficients of the secondary process are estimated using the (fast) Fourier transform, performed on two successive blocks (block $m-1$ and block m) of the controller output signal $s(k)$ and the measured error signal $\varepsilon_h(k)$. Each of the blocks comprise one (ore a few) period(s) of the signal, yielding after subtraction the Fourier coefficients of the difference signals: $\Delta S_\nu(m)$ and $\Delta E_{h,\nu}(m)$. It is assumed that the signals are stationary during one block. The input-output relation for a system-identification configuration with these signals is

$$\Delta E_\nu(m) = \Delta Y_{p,\nu}(m) + H_\nu(m)\Delta S_\nu(m) + \Delta H_\nu(m)\Delta S_\nu(m) + \Delta H_\nu(m) S_\nu(m)$$

Furthermore it is assumed that the alterations in the Fourier coefficients (4.4.2) are very small during two blocks, so $H_\nu(m) \approx H_\nu(k)$ if k is in block $m-1$ and in block m.
Since the frequency coefficients may be considered to be independent, a very simple configuration can be used. The configuration is depicted in figure 4.4.2, note the resemblance to figure 4.1.1.

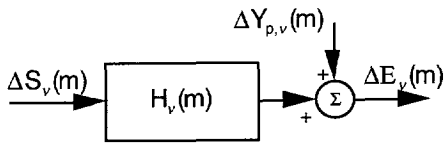

Figure 4.4.2 ; *Estimation of the Fourier coefficients* $H_\nu(m)$ *using difference signals (block operation).*

If the primary difference signal $\Delta Y_{p,v}(m)$ is assumed to be negligibly small and, moreover,

$$H_v(m) \approx H_v(m-1), \quad v = 1,\ldots N,$$

than the input-output relationship of the configuration shown in figure 4.4.2 is

$$\Delta E_v(m) \approx H_v(m)\Delta S_v(m), \tag{4.4.3}$$

yielding the (stabilized) least squares solution

$$H_{v,ls}(m) = \frac{\Delta S_v^*(m)\Delta E_v(m)}{\alpha + |\Delta S_v(m)|^2}, \tag{4.4.4}$$

in which α is a small positive constant.
The updating algorithm must be used with care since it is not unimaginable in ANC that $\Delta S_v(m) \approx 0$, yielding questionable values for $H_{v,ls}(m)$. To avoid this a range is defined: the estimation may only be performed if $|\Delta S_v(m)| \geq \beta$, and β being a positive constant. The range is known as the dead zone of the algorithm.
The equations (4.4.3) , (4.2.20):

$$R_v(m) = H_{v,ls}(m)X_v(m),$$

and (4.2.21)

$$\Theta_v(m) = \Theta_v(m-1) - \gamma \frac{R_v^*(m)E_v(m)}{\alpha + |R_v(m)|^2},$$

are implemented in a hardware controller ('HADAP'-unit). This active noise control unit is used in situations where the revolution frequency and the acoustical process are changing in time relatively slowly (it is also used in the experiments described in chapter 2). A great number of experiments is carried out in several industrial applications, in chapter 5 an example of an industrial application in which it is used will be presented.

4.4.2 The estimation of the Fourier coefficients in a sample based Fourier controller

With the help of the projection algorithm the Fourier coefficients $H_v(k)$ (4.4.2) can also be estimated on a sample base. The derivations will be more clear for the off-line configuration, so before the on-line estimation method based on *difference* signals is discussed, the off-line estimation method based on normal signals will be interpreted. It is assumed that during the off-line estimation the controller parameters $\bar{\theta}_c$ are fixed.
The controller output signal is (see (4.2.1))

$$s(k) = \vec{\varphi}^{H}(k)\vec{\theta}_c = \sum_{v=1}^{N} \varphi_v^*(k)\theta_{c,v} . \qquad (4.4.5)$$

In figure 4.4.3 the off-line output-error configuration is drawn.

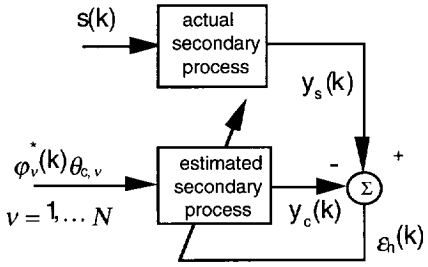

Figure 4.4.3 ; *The output error configuration used to estimate the Fourier coefficients of the secondary process on a sample base (off-line).*

The real part of the controller output $s(k)$ is the input for the actual secondary process, so, if the FIR elements are real the output of the secondary process is

$$y_s(k) = Re\left[\sum_{j=0}^{J-1} h_j(k) \sum_{v=1}^{N} \varphi_v^*(k-j)\theta_{c,v}\right] =$$

$$= Re\left[\sum_{v=1}^{N} \varphi_v^*(k)\theta_{c,v} \sum_{j=0}^{J-1} h_j(k)\varphi_v^*(-j)\right]. \qquad (4.4.6)$$

Combination of the expression for $\varphi_v(k)$ (equation (4.04)) and equation (4.4.2) yields

$$y_s(k) = Re\left[\sum_{v=1}^{N} \varphi_v^*(k)\theta_{c,v} H_v(k)\right]. \qquad (4.4.7)$$

Using for convenience $x_v^*(k) = \varphi_v^*(k)\theta_{c,v}$, this can be written as

$$y_s(k) = Re\left[\sum_{v=1}^{N} x_v^*(k) H_v(k)\right]. \qquad (4.4.8)$$

The input of the estimated secondary process is multi dimensional ($x_v^*(k)$, $v = 1, \ldots N$).The output of the estimated process must be real. Assume that the estimated Fourier coefficients are $H_{v,c}(k)$, than the output can be written as

$$y_c(k) = Re\left[\sum_{\nu=1}^{N} x_\nu^*(k) H_{\nu,c}(k)\right]. \qquad (4.4.9)$$

The output error obviously is $\varepsilon_h(k) = y_s(k) - y_c(k)$. The projection algorithm applied to the configuration depicted in figure 4.4.3 gives the algorithm with which the Fourier coefficients of the secondary process can be estimated on a sample base:

$$H_{\nu,c}(k) = H_{\nu,c}(k-1) + \gamma \frac{x_\nu(k)\varepsilon_h(k)}{\alpha + x_\nu^*(k)x_\nu(k)}. \qquad (4.4.10)$$

The estimation of the Fourier coefficients on-line, in the presence of the primary signal, requires a configuration with difference signals. The error equation of the estimation loop is (see figure 4.4.4)

$$\varepsilon_h(k) = \Delta y_s(k) + \Delta y_p(k) - y_c(k). \qquad (4.4.11)$$

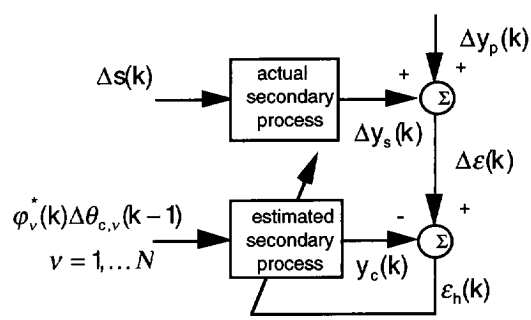

Figure 4.4.4 ; *On-line estimation of the Fourier coefficients on a sample base.*

The derivation of the algorithm with which the Fourier coefficients are estimated on-line on a sample base is identical to the off-line derivation, but for two additional assumptions:

- the frequency coefficients f_ν of the primary difference signal $\Delta y_p(k)$ are negligibly small
- the *differences* $\Delta\theta_{c,\nu}(k-1)$ are changing in time only slowly .

Defining $\Delta x_\nu^*(k) = \varphi_\nu^*(k)\Delta\theta_{c,\nu}(k-1)$, the updating algorithm can be written as

$$H_{\nu,c}(k) = H_{\nu,c}(k-1) + \gamma \frac{\Delta x_\nu(k)\varepsilon_h(k)}{\alpha + \Delta x_\nu^*(k)\Delta x_\nu(k)}. \qquad (4.4.12)$$

Since generally the difference signal is small (in order to fulfill the filtered-x assumption), the controller output $y_c(k)$ will be small in relation to the 'extraneous' noise $\Delta y_p(k)$, which means that this method can only be used if the parameters to be estimated change in time slowly

In the projection algorithm (4.2.17) with which the controller parameters $\vec{\theta}_c(k)$ of the (sample based) Fourier controller are estimated the filtered-x values $r_v(k)$ are used. The filtered-x values are calculated with the estimated Fourier coefficients of the secondary process. Using the definition (4.2.10) the filtered-x values are

$$r_v(k) = \sum_{j=0}^{J-1} h_j^*(k)\varphi_v(k-j) = \varphi_v(k)\sum_{j=0}^{J-1} h_j^*(k)\varphi_v(-j), \tag{4.4.13}$$

so

$$r_v(k) = \varphi_v(k)H_{v,c}^*(k). \tag{4.4.14}$$

4.5 Conclusions

The ANC controller problem has been solved using a parameter estimation approach. The parameters are estimated using a simplified RLSE method: Kaczmarz's projection algorithm [15]. Actually this projection algorithm is referred to by other authors as Normalized Least Mean Squares (NLMS, [14] and [16]). However, the interpretation of the algorithm as a sequence of projections of the estimator on the input vectors clarifies some interesting properties of the algorithm. Firstly place the interpretation shows that it is very important for the convergence speed that the input vectors are orthogonal. An I-dimensional vector in an I-dimensional orthogonal space can be estimated with the projection algorithm in I steps. It means that if the input vectors are orthogonal, the eigenvalue spread of the input correlation matrix is already optimal after one period of the reference signal. Furthermore, in a geometric interpretation the consequences of extraneous noise and a time varying process parameter vector can be easily visualized.

In 1975 Glover [11] proposed to use a sine and a cosine as input signals for noise cancellation. In his concept he uses a unit 'secondary process' and therefore the LMS-algorithm in combination with these input signals may be considered to be a projection algorithm with orthogonal (Fourier) input vectors. In an anti noise (filtered-x) configuration comprising a real secondary process these Fourier input vectors can be used too. However, in order to guarantee an optimal eigenvalue spread of the input correlation matrix the (filtered) input signals must be scaled properly.

In this chapter the proper scaling factors are derived for a SISO controller and a MIMO controller. In a number of experiments the behaviour of the projection algorithm using optimally scaled Fourier input vectors (a Fourier controller) is compared with the projection algorithm applied to a tapped delay line. The experiments show that due to the optimal eigenvalue spread the convergence speed of the Fourier controller is much higher

in both the SISO as well as in the MIMO controller.
Finally, the on-line estimation of the Fourier coefficients of the secondary process is discussed. It is proposed to estimate the coefficients using difference signals, thus reducing the correlation between the primary noise and the excitation signal. The method works well in practice and is implemented in a hardware control unit comprising the block-based Fourier controller ('HADAP').

5. PRACTICAL APPLICATIONS OF ANTI NOISE

Introduction

In the previous three chapters the theoretical derivations underlying active noise control were illustrated with the results of numerical simulations and experiments in the laboratory. Two algorithms have been developed during this study: the on-line estimation based on difference signals, described in section 4.4 and the sample based Fourier controller described in section 4.2. In two applications these algorithms are used. In this chapter the ANC experiments in the applications and their results are described.
In the first experiment ANC is used to reduce periodic noise generated by a vacuum pump, installed in a chemical plant. The pump is used to maintain reduced pressure inside the drums of filters used for drying and washing a chemical substance. Two fall-pipes coming from the delivery side of the pump drain off a mixture of hot water of about 70 °C and very humid air into a reservoir. The revolution frequency of the pump is approximately 8 Hz, and the pump has 16 rotor blades. The 16^{th} , 32^{nd} and 48^{th} harmonic of the revolution frequency are strongly present in the frequency spectrum of the noise coming out of the fall-pipes. The wave-lengths of the harmonics shift in the course of time due to alterations in the temperature and changes in the density of the air and water mixture. In these circumstances the reduction of the low frequency noise with passive means is difficult to achieve. If active noise control is to be used, a fully adaptive system is needed, adjusting its parameters to alterations in both the primary noise and the secondary process. In the experiments the periodic noise coming out of the fall-pipes is reduced with the help of an anti noise controller with the following characteristics: a hard-ware unit, the so called 'HADAP-unit', developed by TPD, comprising algorithms for the block-based Fourier controller in combination with the on-line estimation of the secondary process described in section 4.4.1.
In the second experiment ANC is used to reduce periodic low frequency noise inside the cabin of a delivery van. The noise level in the cabin is annoyingly high, mainly because the sound insulation of the cabin is poor at low frequencies. The periodic noise in the cabin is largely determined by the diesel engine. The firing frequency and several harmonics of the engine revolution frequency are present in the frequency spectrum during a drive. During acceleration and deceleration the revolution frequency of the engine changes continuously. However, it may be assumed that the rate of these changes are so small, that the primary noise may be considered periodic. The inner dimensions of the cabin roughly are 1.65 m. width x 1.25 m. length x 1.60 m height , and up to 200 Hz the modal density is not very high. In the experiments the engine related noise in the cabin is reduced with an anti noise system for three dimensional situations. The multi-channel system contains 5 error-microphones and 4 anti noise sources. The controller must be able to track the fast changes in the primary wave field meaning that the sample based Fourier controller must be used.
In both experiments the measured data is recorded on a multi channel digital recording

system (a DAT recorder). Simultaneously with the measured microphone signals a pulse train is recorded comprising 256 pulses per revolution (vacuum pump) or 35 pulses per revolution (delivery van). With the help of the pulse train the recorded microphone signals can be analysed using a sampling frequency which is synchronized with the engine revolution. The Fourier transform applied to data blocks acquired with a synchronized sampling frequency yield *order spectra.*

5.1 Anti noise applied to a vacuum pump in a chemical plant

5.1.1 Introduction

The reduction of noise caused by large industrial vacuum pumps is a well known problem in industrial noise control. The noise is generated in the pumps by the rotor blades and propagates through the duct on the delivery side to the environment. The frequency spectrum of this noise generally is dominated by a few harmonic components, the blade passing frequency (i.e., the revolution frequency of the axis times the number of rotor blades) being the fundamental frequency. In these large pumps the blade passing frequency ranges from some 30 Hz up to about 150 Hz. The pressure levels in the ducts can be very high, and sometimes even non-linear acoustics is involved. Often the ducts transport not only air but also water, dust, chemical residues and the like. Furthermore, the temperature, mean flow and the density in the duct and sometimes the revolution frequency of the pump change in the course of time. Given all those circumstances, passive noise reduction is very difficult: scalings accumulate on sound absorbing materials and tuned resonators get out of tune.
In some cases active noise control can provide a solution, especially if the frequency spectrum is dominated by a few harmonic components only. The variations in the temperature, density and mean flow require a controller able to update on-line the transfer function from error microphone to anti noise source regularly (say every minute or so). In the ducts of the vacuum pump with which the experiments are carried out the variations are slow as compared to the period of the blade passing frequency. Furthermore, the changes in the revolution frequency of the axis are very small: within 0.5% during the measurements. Therefore it is certainly possible to use a block-based Fourier controller to reduce the periodic pump noise. This controller, combined with an on-line estimation of the transfer function described in section 4.4.1 is implemented in a one-channel hardware unit developed and constructed at TPD, which comprises a Digital Signal Processor (DSP).

5.1.2 The initial situation in the plant

The machine with which the experiments are carried out, is a dual vacuum pump the suction being based on centrifugal force. Each side of the dual pump has 16 rotor blades

and one common axis which is driven via driving belts by a large electromotor of about 100 kWatts. The dual vacuum pump can serve two systems at different vacuum levels. There are two inlets on top of the pump and two outlets at the back side. In figure 5.1.1 a picture of a pump is shown. In the front the electromotor is visible; the driving belts are covered for safety reasons. The two pump inlets on top are connected to one vacuum pipe, the two outlets drain off through fall-pipes into a reservoir.

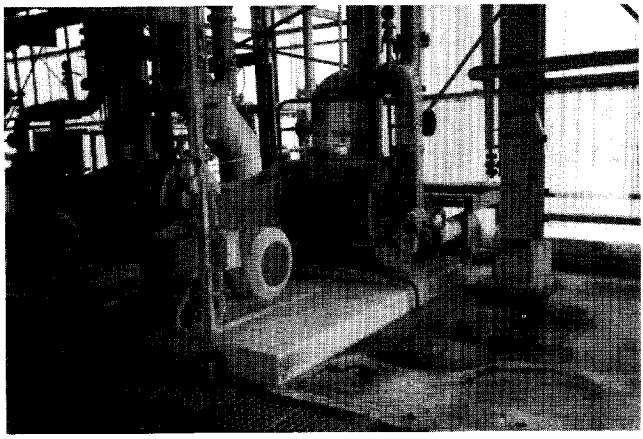

Figure 5.1.1 ; *The vacuumpump as it is installed on the platform in the filter-building. The dimensions of the platform are about 3.5 x 2 m.*

Actually in total 5 of these vacuum pumps are installed on the ground floor of what is known as the filter building. Generally two or three of the pumps are at work. In figure 5.1.2 the situation in the filter building is shown.

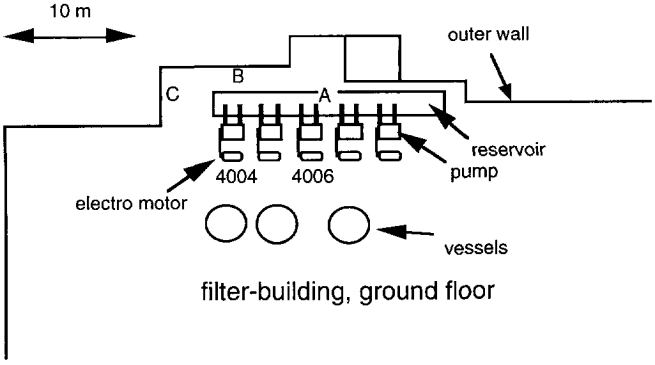

Figure 5.1.2 ; *The situation in the filter-building .The measurement positions are indicated by the letters A,B and C.*

ANC experiments are carried out with the pumps numbered 4004 and 4006 but also some measurements are made while other pumps (4007 and 4008, the two pumps to the right of 4006) are at work. The reservoir is covered with concrete lids and the fall-pipes stick through circular openings in the lids into the reservoir. Noise coming out of the fall-pipes comes into the building through cracks and openings between the lids and the reservoir. The pumps and the electromotors are placed on platforms on the concrete floor (see figure 5.1.1). The outer wall of the building is made of corrugated plastic. On the pumps 4004 and 4006 an optical sensor is mounted on the fly-wheel giving a synchronization signal of 256 pulses per revolution. With the help of the synchronization signal the harmonics due to 4004 and 4006 can be traced in the measured spectra, provided of course that the frequency resolution is sufficient. The revolution frequencies of the pumps are all around 8 Hz. The revolution frequency of the pump 4004 is 7.66 Hz giving a blade passing frequency of just over 122.5 Hz, while the pump 4006 has a blade passing frequency of 123.5 Hz. A number of noise measurements are made in the filter building in several combinations with working pumps. On 3 positions around the pumps (A,B and C, see figure 5.1.2) microphones were placed at a height of approximately 2 meters.
The acoustic pressure at position B, recorded while the pumps 4004, 4007 and 4008 are at work, is analysed using a synchronized sampling frequency. The synchronization signal from the optical sensor on pump 4004 is used and the amplitudes of the frequency components of 50 blocks of 2048 samples are averaged, yielding the order spectrum shown in figure 5.1.3. Clearly the first order harmonic (the blade passing frequency), the 2^{nd} order harmonic and the 3^{rd} order harmonic are prominent in the spectrum. The two other high levelled frequency components around the harmonics of 4004 are the harmonics of the blade passing frequencies of the pumps 4007 and 4008. Simultaneously the pressure level at the positions A and C is measured.

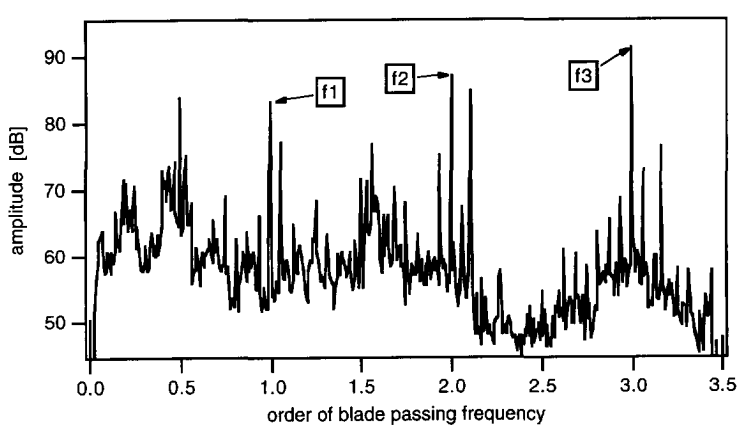

Figure 5.1.3 ; *The order spectrum at position B while 4004, 4007 and 4008 are at work. The sampling frequency is synchronized with the revolution of 4004.*

In figure 5.1.4 (left figure) a bar chart is shown in which the pressure levels of the blade passing frequency of 4004 ('1') and the two ensuing harmonics ('2') and ('3') are depicted for the measurement positions A, B and C. Note that the mutual relation between the levels of the first three harmonics differ from one measurement position to another. Furthermore, it turned out that the pressure levels of the harmonics strongly fluctuate in time. In figure 5.1.4 at the right the same bar chart is made for a measurement a few hours later, the same pumps are at work and the operating conditions did not change.

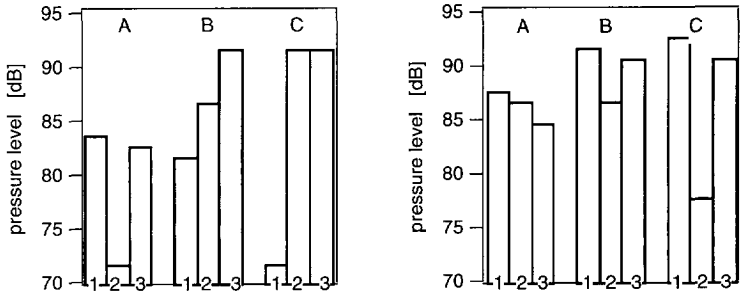

Figure 5.1.4 ; *The pressure levels of the blade passing frequency (1), the first harmonic (2) and the second harmonic (3) on the measurement positions A, B and C on two different moments.*

The large changes in the pressure level can be explained assuming that the pressure is an addition of interfering waves, while the amplitudes and phases of these waves change in time.

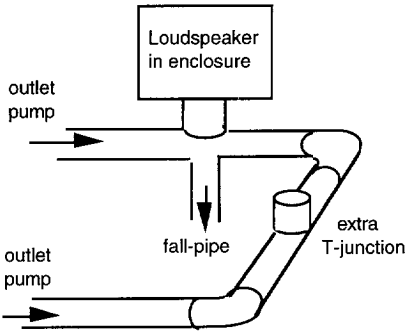

Figure 5.1.5 ; *The PVC modification of the two outlets to one fall-pipe.*

5.1.3. The anti noise set-up

Each (dual) vacuum pump has two outlets and so two single channel anti noise systems would be required to silence one pump. However, without any objections the two outlets

may be connected to one fall-pipe, making it possible to silence one pump with one single channel anti noise system. Therefore one fall-pipe is removed and the two outlets are connected to one fall-pipe. In figure 5.1.5 the modification of the fall-pipes of 4004 and 4006 is drawn schematically, showing the (PVC) ducts connecting the two outlets. The diameter of the ducts is 0.15 meters. In the figure the loudspeaker is placed just above the fall-pipe. In figure 5.1.6 a picture of the modification of 4004 is shown.
The anti noise source, a 15-inch 500 watts loudspeaker in an enclosure, is placed just above the fall-pipe (see figures 5.1.5 and 5.1.6). In order to avoid radiation, the enclosure has a double wall; the inner wall is made of PVC, the outer wall of compressed

Figure 5.1.6 ; *The PVC modification with which the two outlets are connected to one fall-pipe. The enclosure of the loudspeaker (without cover) is visible. The dimensions of the loudspeaker box are about 0.5 m x 0.5 m x 0.5 m.*

wood. The error sensor, a microphone in a rubber, waterproof cover, was placed in the fall-pipe and was protected against the direct flow of (hot) water streaming through the pipe. The error microphones are calibrated without the covers. During all measurements the operating conditions for the pumps did not change, however this does not mean that there are no variations in the temperature, the mean flow and the averaged density in the ducts.
In order to determine the effect of the modification on the acoustic pressure levels, the

pressure at the positions A, B and C is recorded at two different moments while the pumps 4004, 4007 and 4008 are at work. In figure 5.1.7 the pressure levels at the blade passing frequency of 4004, the 2nd harmonic and the 3rd harmonic are shown in a bar chart. Noticeably the levels at A, B and C are on the average some 10 dB below the levels depicted in figure 5.1.4. Other measurements, including measurements at the harmonics due to the vacuum pump 4006, show that on the average the modification indeed reduces the level of the acoustic pressure at the harmonics.

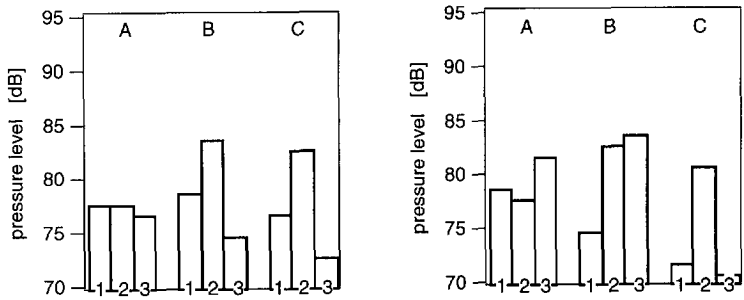

Figure 5.1.7 ; *The pressure levels of the blade passing frequency (1), the first harmonic (2) and the second harmonic (3) on the measurement positions A, B and C on two different moments after the modification, but without anti noise.*

In the ANC experiments, the anti noise signals are calculated using the block based Fourier controller described in chapter 4. The blocks of data on which the Fourier transforms are applied are acquired with a synchronized sampling frequency using the optical sensor. The transfer functions are updated on-line with the algorithms described in section 4.4.1 (no estimation is made before operation).
The acoustic pressures at the two error microphones in the fall-pipes and at the three measurements microphones A, B and C are recorded simultaneously with the sensor signals from the optical sensors on the fly-wheels of 4004 and 4006.

5.1.4. Anti noise applied to the vacuum pump

A complete ANC system is installed on both the vacuum pumps 4004 and 4006. In a first experiment anti noise is applied to the blade passing frequency, the 2nd harmonic and the 3rd harmonic due to 4006. During the experiment no other pumps are at work. The acoustic pressure at the error microphone, mounted in the fall-pipe of 4006, and at the positions A, B and C is recorded without and with anti noise.

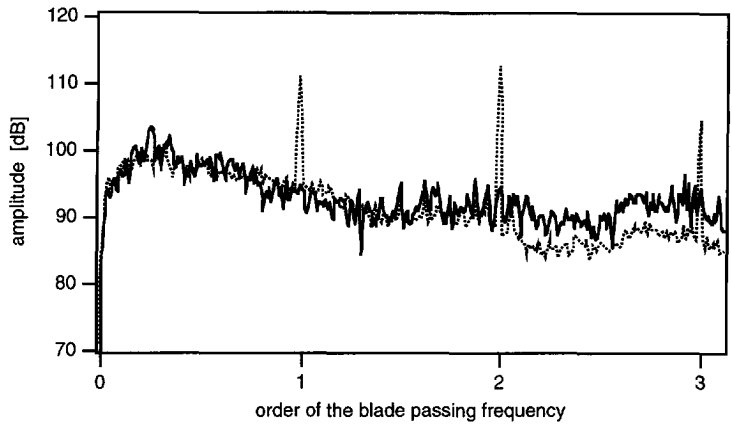

Figure 5.1.8 ; *The order spectra without ANC (dotted line) and with ANC (solid line) on the error microphone of 4006.*

The measurements are analysed using a synchronized sampling frequency. In figure 5.1.8 the order spectra of the pressure with ANC (solid line) and without ANC (dotted line) at the error microphone are depicted. The pressures of 50 blocks of 2048 samples are averaged, in the figure only the first 400 components of the spectra are shown. The recording with ANC is made about 30 seconds after the controller has been started. Clearly the harmonic components at the fundamental frequency and the two following harmonics are reduced to the level of the surrounding frequency components. The increased level around the 3rd harmonic during ANC is probably due to flow noise. Although the acoustic pressure of the harmonics is reduced completely in the fall-pipes, there is no substantial reduction at the positions A, B and C: as an example the order spectra at position B are analysed and depicted in figure 5.1.9. The level at the fundamental frequency is higher during ANC while the level of the 3rd is lower. This means that the acoustic pressure at the harmonic frequency components in the filter building is not only determined by the noise coming out of the pump outlets but also by other sources. The measurements without and with anti noise are carried out with a time interval of about one hour, and so the changes in figure 5.1.9 might as well be caused by an alteration of amplitudes and phases of interfering waves.

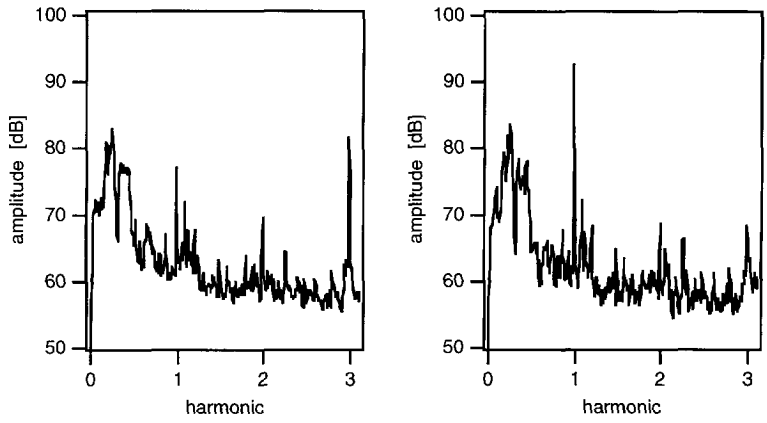

Figure 5.1.9 ; *The order spectra without ANC (left) and with ANC (right) on the measurement microphone B.*

In a second experiment the measurements are repeated, in this case not only 4006 but also 4008 is at work. In figure 5.1.10 the order spectra without ANC (dotted line) and with ANC (solid line) at the error microphone are shown. Again the harmonics due to 4006 are reduced completely. In these measurements the level at the surrounding frequencies due to flow noise is not as high as in figures 5.1.8. The reduction of the second harmonic is over 30 dB. Note that in both situations without- and with anti noise the harmonics of 4008 are present, the algorithm is not bothered by these harmonics. Again there is no distinct reduction of the acoustic pressure at the measurement microphones A, B and C.

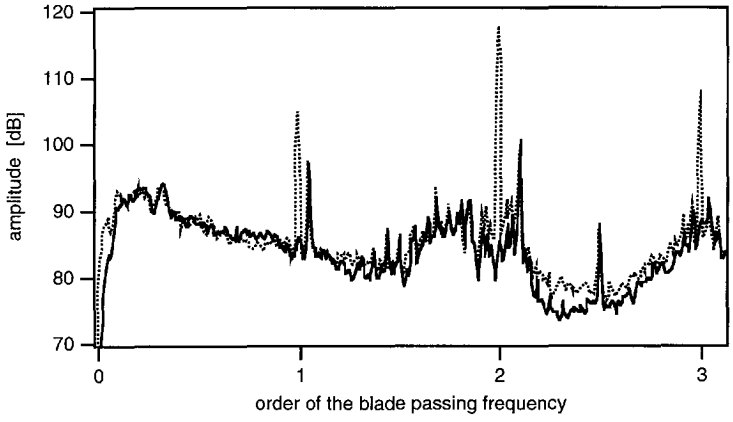

Figure 5.1.10 ; *The order spectra without ANC (dotted line) and with ANC (solid line) on the error microphone of 4006. During both measurements 4008 is at work.*

The experiments are repeated 5 times spread over two different days. In all experiments the level at the harmonic components measured at the error microphone in the fall-pipe of 4006 is reduced to the level of the surrounding frequency components. The pressure amplitudes of the 5 measurements are averaged for each harmonic component and each position. The results are compared with the results of 5 measurements in the initial situation and the results of 4 measurements with the duct modification but without ANC. The results are plotted using bar charts in figure 5.1.11a (position A), 5.1.11b (position B) and 5.1.11c (position C).

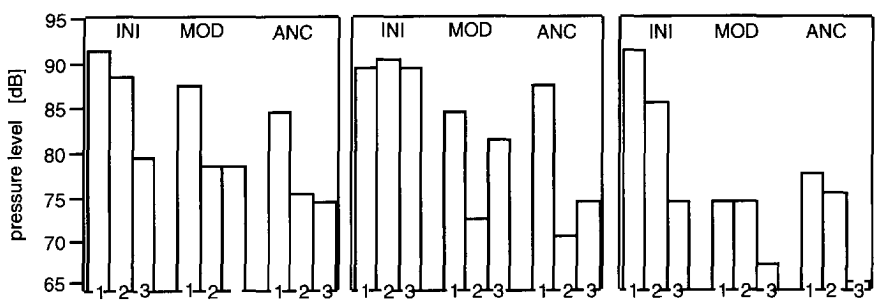

Figure 5.1.11a Figure 5.1.11b Figure 5.1.11c

The pressure levels at the three first harmonic components averaged over several measurements. INI: initial situation, MOD: after the modification of the ducts, ANC: with ANC. a) The levels at position A; b) the levels at B, c) the levels at C.

The initial situation is marked by INI, the modified situation without ANC by MOD and the modified situation with ANC by ANC. The modification of the outlet ducts causes a considerable reduction, especially at the positions B and C (the farthermost position from 4006). The additional reduction due to anti noise is small, at some harmonics even an increase is found. The same experiments are carried out with ANC on the fall-pipe of 4004. In figure 5.1.12 the order spectra at the error microphone in the fall-pipe of 4004 without ANC (dotted line) and with ANC (solid line) are plotted. The fundamental frequency and the 2nd harmonic are reduced to the level of the surrounding frequency components but the ANC system is not able to reduce the 3rd harmonic. In experiments with the loudspeaker mounted in a comparable geometrical situation in the laboratory higher pressure levels could be realised around these frequencies. Apparently the circumstances in the outlet (high temperature and humidity and an increased static pressure) reduce the efficiency of the loudspeaker in its enclosure at these frequencies. The results of the experiments show that the algorithms are capable to find the correct transfer functions and are able to calculate the proper anti noise signal in the circumstances of the vacuum pump. Furthermore, apart from the 3rd harmonic of 4004, the ANC system reduces the acoustic pressure at the harmonics on the error microphone to the level of the surrounding frequencies.

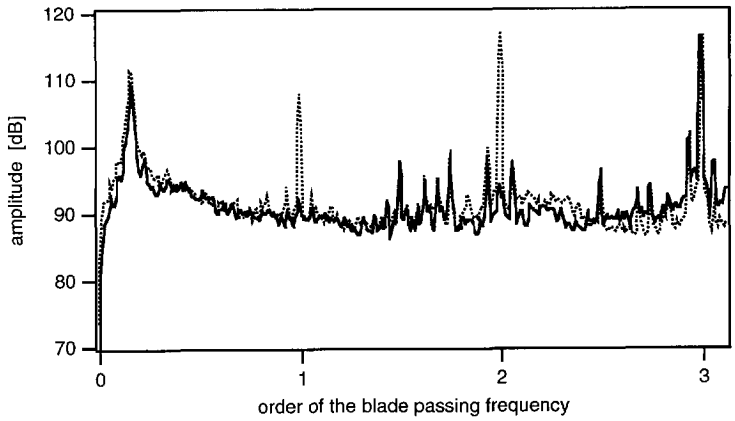

Figure 5.1.12 ; *The order spectra without ANC (dotted line) and with ANC (solid line) on the error microphone of 4004.*

In the initial situation, before the modification is made, the periodic noise in the filter building is largely determined by the noise coming out of the outlets of the pumps. After the modification, in which the two outlets are connected to one fall-pipe, the periodic noise in the filter building is mainly caused by other sources (radiation of the pump itself and the ducts). So, in spite of the fact that the anti noise system works properly, there is no considerable reduction in the building.

5.2 Anti noise in the cabin of a delivery van

5.2.1 Introduction

The sources of noise in vehicles which are driven by a combustion engine can roughly be divided in two types: the sources related to the drive unit (combustion noise, transmission) and the sources related to other sources (rolling noise, wind). The sources related to the power unit are mainly periodic and deterministic, whereas the others are mainly stochastic. If no noise control measures are taken the noise level in the interior of vehicles is very high. Therefore car manufacturers apply passive noise control to prevent hearing damage of driver and passengers and to improve the comfort in the cabin. At low frequencies, below about 200 Hz, passive noise control for airborne noise is bulky or weighty and therefore not very suitable in (small) vehicles. The firing frequency of most combustion engines installed in cars lies within the low frequency range from about 20 Hz up to 200 Hz. In most passenger cars the level at the firing frequency is prominent in the spectrum measured during a drive. Although this so called 'booming noise' adds in most cases virtually nothing to the noise level in dB(A), it is known to be annoying, so

the reduction of 'booming noise' improves the comfort in the interior. Passive reduction of noise at the firing frequency is not practical, while active reduction is very feasible because the noise source is periodic, a reference signal is available and the modal density is not high below 200 Hz in most car interiors [20], [21] . So, multi dimensional active noise control for the firing frequency complements passive noise control in vehicles equipped with a combustion engine. The performance of multi-dimensional ANC depends on the maximum convergence speed of the adaptive algorithm. In cars the changes in the revolution frequency are relatively fast and therefore a fast convergence is needed. This means that the performance strongly depends on the eigenvalue spread of the input correlation matrix of the algorithm (see chapter 4). In small commercial vehicles, like for example delivery vans, not only the firing frequency but also other harmonics contribute substantially to the noise level at frequencies below 200 Hz [22]. According to the derivations and experiments in chapter 4 an ANC system with a sample based Fourier controller is able to reduce several harmonics without instability problems while the eigenvalue spread is optimal. In a small commercial vehicle, a delivery van, the behaviour of the sample based Fourier controller has been studied. The Fourier controller is implemented on a DSP (TMSC30) based hardware developed and controller constructed at TPD ('Octopus'). With the help of an acoustic antenna comprising 64 microphones which are multiplexed to an 8 channel (digital) recording system, the wave field in a horizontal plane is measured during the experiments. The microphones of the antenna are mounted at a height just above the head of the driver (1.4 m above the floor). The switch-pulse of the multiplexer is synchronized with the engine revolution in a such a way that there is an integer number of engine revolutions in each block of data.

5.2.2 The wave field in the delivery van

The experiments are carried out in the cabin of a Mercedes delivery van, type 309 D, which is equipped with a five cylinder diesel engine (65 kWatt). The cabin of the van is separated from the cargo space by a partition wall of 15 mm thick ply wood. The engine compartment is positioned in the front of the car, more or less between the driver seat and the passenger seat. In figure 5.2.1 a schematic side view of the interior is shown.
The sound insulation of the engine is poor because the passive noise control measures are restricted: the demands for comfort are not considered to be as high as they are in a passenger car and generally no weighty partitions are used because they diminish the carrying capacity.
In the cabin not much passive absorption is present. At frequencies below 200 Hz the reverberation time is about 0.25 seconds, giving an averaged absorption coefficient a=0.15. Computer simulations [23] of the wave field in the cabin interior imply that the modal density is small at frequencies below about 200 Hz. In these computer simulations on a 2 dimensional wave field the eigenfrequencies of a *vertical plane* between the driver seat and the passenger seat are calculated up to 200 Hz. There are of course more actual eigenfrequencies in the (3 dimensional) cabin between 0 Hz and 200 Hz, but the 2D

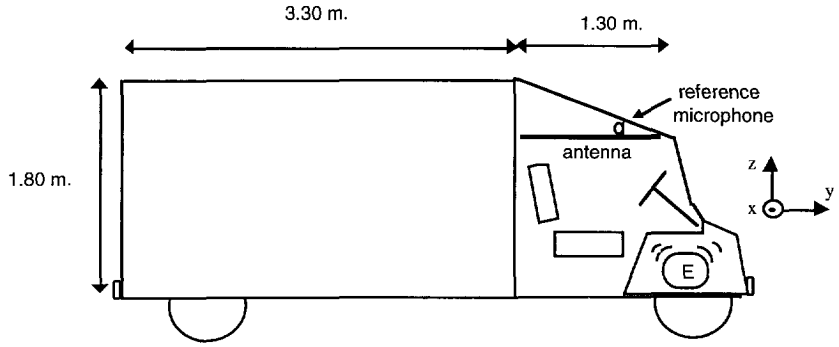

Figure 5.2.1; *A sectional view of the delivery van.*

simulations give an impression of the modal density. In the 2D wave field the eigenfrequencies are 57 Hz, 90 Hz, 159 Hz and 197 Hz. The actual number of eigenfrequencies can be estimated by studying the acoustic resonances in the cabin. In an experiment loudspeakers are placed at two positions near the bottom of the cabin: in the corner behind the passenger seat and in the corner in front of the passengers seat. The acoustic transfer functions from each of the the loudspeakers to 7 microphones, placed near the ceiling in the other corners of the cabin are measured, and the average of the amplitudes of the resulting 14 transfer functions as a function of the frequency is calculated. The result is plotted in figure 5.2.2. The eigenfrequency at 90 Hz and to a less extent at 157 Hz can be found back as resonances in the cabin. Besides these resonances there are some more maxima in the averaged acoustic transfer (50 Hz, 100 Hz, 110 Hz, 142 Hz 175 Hz and around 200 hz), but the number is restricted and it may be assumed that up to about 150 Hz the modal density is not high.

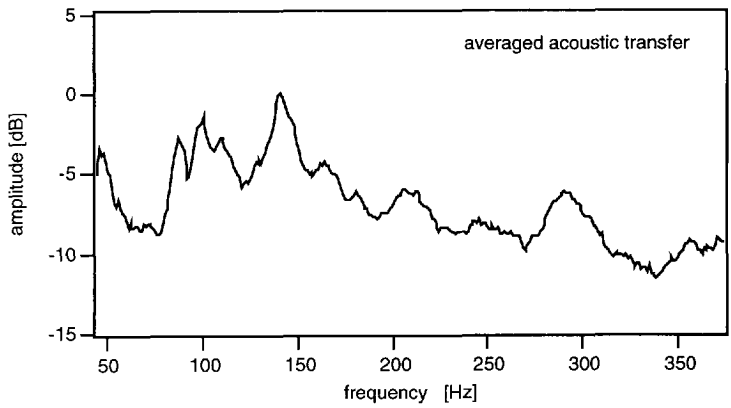

Figure 5.2.2; *The amplitude averaged over 14 acoustic transfer functions in the delivery van.*

At any resonance frequency there will be clearly audible spatial maxima and minima of the acoustic pressure if the modal density is small. With the help of the acoustic antenna these maxima and minima can be made visual. At 70 km/h (5^{th} gear) the firing frequency is about 108 Hz which is close to one of the eigenfrequencies of the cabin. In figure 5.2.3 at 64 positions the spectral component of the wave field at the firing frequency is shown. The driver position is in the right corner at the back (at the minimum x position and the minimum y position), while the steering wheel is in the right foremost corner of the figure (at the minimum x position and the maximum y position since it is not an English car).

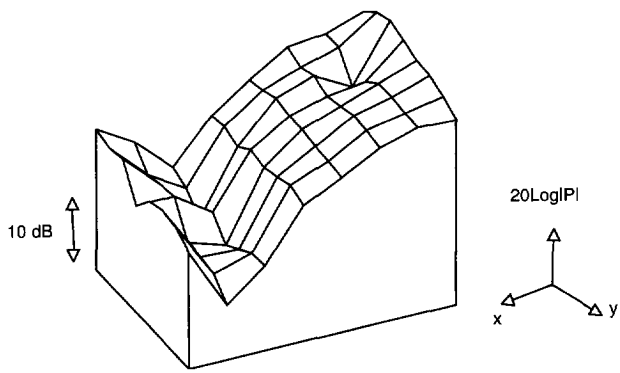

Figure 5.2.3; *The wave field in the cabin at the firing frequency. The speed is 70 km/h (5^{th} gear)..*

The amplitude of the wave field at the firing frequency is high at the right side of the figure (the driver side), while there is a nodal line of small pressure amplitudes in the length direction at the left (passenger side). Note that there is a small dip in the wave field which is caused by the head of the driver.

The five cylinder engine ignites five times in two revolutions of the engine so in the order spectrum of the engine harmonics the firing frequency is found at 2.5. The engine revolution frequency during a drive ranges from 10 Hz (600 rpm) up to 75 Hz (4500 rpm) so the firing frequency ranges from 25 Hz to nearly 190 Hz.

The acoustic pressure is measured in a great variety of driving conditions. Synchronous with the microphone signals, a pulse train produced by a (magnetic) sensor which counts the 140 cogs on the flywheel is recorded (after a division by 4, so 35 samples per revolution are on the tape).

In order to study the behaviour of the algorithm in the course of time, sequences of Fourier transformed data blocks are plotted: the acquired data is divided in data blocks and each data block is transformed to the Fourier domain, giving a sequence of engine-order spectra if a synchronized sampling is used and a sequence of frequency spectra if a fixed sampling frequency is used.

In figure 5.2.4 a sequence of 157 blocks acquired with a synchronized sampling frequency is shown. The pressure level (in dB) is indicated by a color, the color-axis is

shown next to the figure. The pressure is measured with a *reference microphone* which is positioned near the ceiling in the left front corner of the cabin (see figure 5.2.1). Each data block comprises 24 periods of the engine revolution frequency, so one data block equals 24x35=840 samples. The constant driving speed is 70 km/h
(± 2 %) in the 5th gear, resulting in an engine revolution frequency of 43 Hz (2600 rpm). One data block covers about 0.55 seconds. In order to smooth the plotted data, the linear moving average of 2 blocks is plotted. The figure makes clear that the level at the firing frequency (2.5 times the engine revolution frequency) is prominent in all blocks. Several harmonics contribute to the noise level. However, occasionally some of the harmonics 'disappear' in the level of the surrounding frequencies. A bump in the road lifts up the entire spectrum a bit (see for instance block number 125). In figure 5.2.5 the order spectrum averaged over all 157 blocks is shown. Clearly the pressure level at the firing frequency rises above the other engine harmonics.

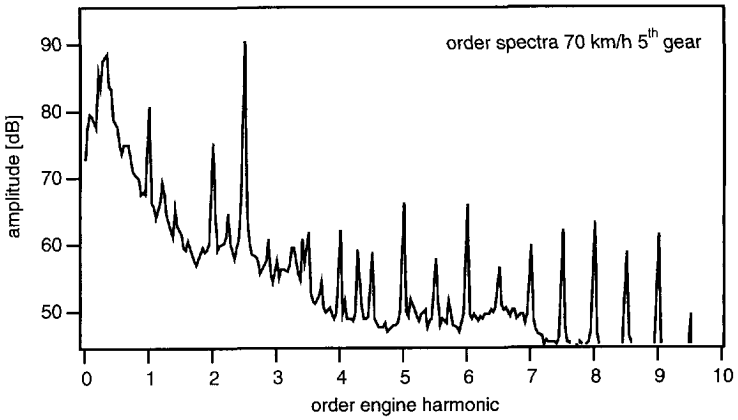

Figure 5.2.5; *Order spectrum in the cabin at 70 km/h.(2600 rpm).*

In another experiment the van is accelerated in the 5th gear from 70 km/h to 110 km/h in 38 seconds (maximum acceleration) after which the throttle pedal is released. During the experiment the acoustic pressure is measured at the reference microphone and a sequence of 210 data blocks is acquired with a fixed sampling frequency. Each data block comprises 256 samples. The sampling frequency is 1024 Hz so one data block takes 0.25 seconds. In figure 5.2.6 the sequence of frequency spectra is shown. At t=0 the speed of the car is just over 70 km/h and the engine revolution frequency is 2650 rpm, resulting in a firing frequency of about 110 Hz. Up to a firing frequency of 160 Hz at t=20 seconds (3800 rpm and 102 km/h), the level of the firing frequency is prominent in the spectrum. Above 3800 rpm the level at the second engine harmonic increases rapidly, and around 4050 rpm (109 km/h at t=30 seconds) the construction seems to be at resonance at twice the revolution frequency (other measurements show that the second engine harmonic also protrudes around 4050 rpm in the 3th and 4th gear). At t=38 seconds the throttle pedal is

released and t=52.5 seconds the speed is again 70 km/h (all in the 5th gear). The figures 5.2.4 to 5.2.6 make clear that in the cabin several engine harmonics substantially contribute to the noise level at low frequencies. In most cases the level at the firing frequency dominates the spectrum above 25 Hz, in some driving conditions however, the level at another engine harmonic is prominent.

5.2.3 *The anti-noise set-up in the delivery van*

The anti noise signals in the delivery van are calculated using the sample based Fourier controller described in chapter 4. The algorithm is implemented on a DSP based hardware unit which is developed and constructed at TPD. All experiments discussed in this section are carried out with a multi-channel system comprising 5 error microphones and 4 anti-noise outputs connected to loudspeakers. The reference signal is obtained with the help of the magnetic sensor on the flywheel. The hardware unit has analog inputs and therefore this sensor signal is fed to a signal generator which generates in each revolution simultaneously one period of a sine and one period of a cosine. In figure 5.2.7 the set up is drawn schematically.

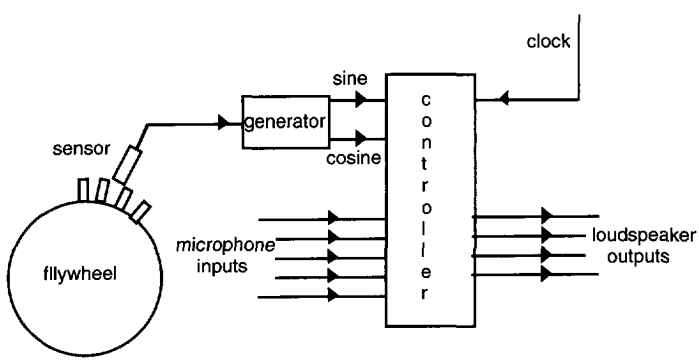

Figure 5.2.7 ; *The set-up of the active noise control system in the delivery van.*

The error microphones are positioned near the ceiling (see figure 5.2.8a) and the anti-noise loudspeakers are placed at floor level, two of them being mounted in the plywood partition wall (figure 5.2.8b). In the ANC experiments a maximum of four engine harmonics will be reduced: the firing frequency at 2.5 times the engine revolution frequency, the second engine harmonic at twice the revolution frequency and additionally one or two others. At frequencies below 38 Hz the efficiency of the loudspeaker is very small and more electric power is needed to cancel the wave field than the loudspeaker can handle. Therefore ANC for the harmonic concerned is switched off automatically if its frequency is below 38 Hz. There is also an upper frequency limit of about 210 Hz which is due to the restricted memory available: the inverse matrices (see chapter 4) are stored in the hardware memory and only a limited number of frequency components can be stored.

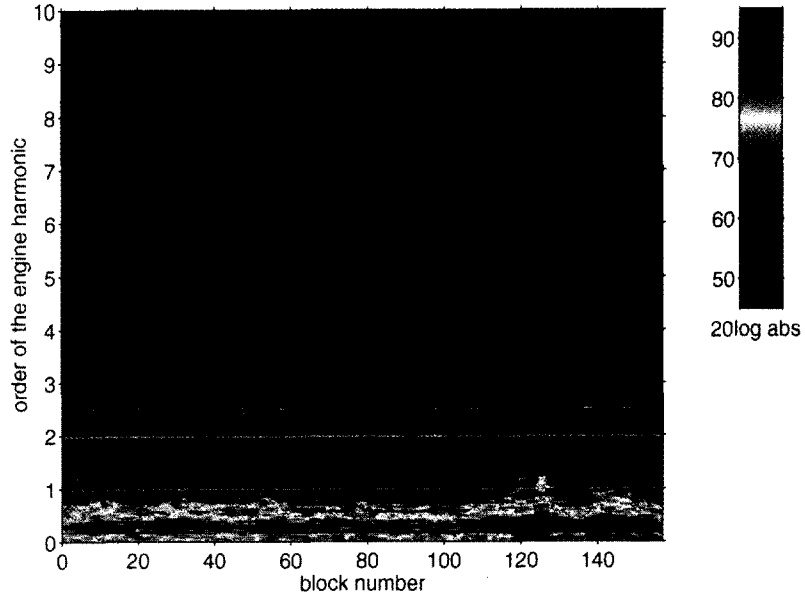

Figure 5.2.4 ; *The order spectra of 157 data blocks measured (gap-free) at the reference microphone at 70 km/h (5th gear).*

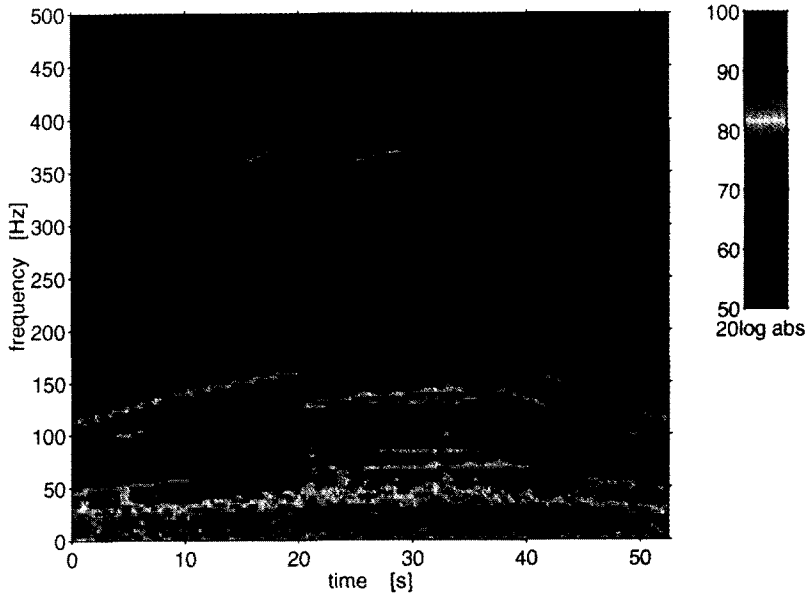

Figure 5.2.6 ; *The frequency spectra of 210 data blocks measured (gap-free) at the reference microphone during acceleration and deceleration from 70 km/h to 110 km/h to 70 km/h (5th gear).*

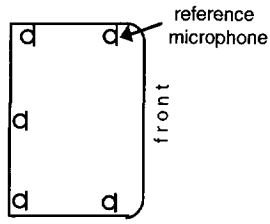

Figure 5.2.8a ; *The microphone positions near the ceiling*

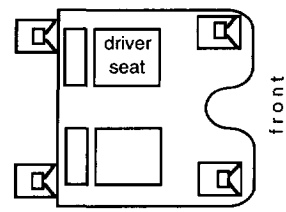

Figure 5.2.8b ; *The loudspeaker positions on the floor.*

Several experiments are carried out at constant driving speed in the 4th and 5th gear, during (normal) acceleration from 0 km/h to 70 km/h with changing gears and during (maximum) acceleration and deceleration from 70 km/h to 110 km/h in the 5th gear. In the experiments at 'constant' driving speed the actual speed varies a little, but always less than ± 2 percent.

The (magnetic) sensor signal, the acoustic pressure at the reference microphone and the (multiplexed) microphone signals of the antenna are recorded on (digital) tapes during all measurements.

The reference microphone is one of the error sensors (see figure 5.2.8a) and a comparison of the acoustic pressures on this sensor with and without anti-noise shows the reduction which is possible using the sample based Fourier controller in the set-up described above. The reduction is optimal if in the spectrum of the residual, the level of the engine harmonic which is cancelled does not rise above the level of the surrounding frequencies. The acoustic pressure on the reference microphone with and without anti-noise will be presented in graphs showing the frequency spectrum as a function of the time and the order spectrum as a function of the block number. The pressure level at the reference microphone is not always a measure for the noise experienced by the occupants of the cabin. For instance, at some frequencies it can happen that the reference microphone is positioned at a spatial pressure minimum while the head of the driver (or the passenger) is at a pressure maximum. Furthermore, the local reduction at the reference microphone due to anti-noise does not guarantee a reduction somewhere else in the cabin. The global reduction strongly depends on the number of dominant eigenmodes (see chapter 3). In general, using 4 anti-noise loudspeakers 4 eigenmodes can be reduced.

With the acoustic antenna a number of wave fields are measured at head height in the cabin. The position of the maxima and minima in the wave field can be determined and the effect of anti-noise on the wave field can be made visual. The acoustic pressure at several harmonic components will be presented in 3D figures, showing along the z-axis the pressure level in the horizontal plane (see figure 5.2.3).

The transfer functions from anti-noise output to error input are measured before operation. During the ANC experiments the transfer functions appear to hardly change and in order to save calculation time these functions are not adjusted during operation.

The majority of the measurements are performed with only the driver in the cabin. The results of measurements when also a passenger was present in the cabin did not significantly deviate from the results of measurements with only the driver present.
All experiments are carried out on asphalted roads in the Netherlands. The measurements with and without active noise control are carried out on the same road but not on exactly the same stretch of the road, so in a few experiments there are small differences in the level of the surrounding frequencies if the situations with and without anti-noise are compared.
The sequences of spectra which will be shown in the following two sections are all averaged (linear moving average of two blocks) before they are plotted.

5.2.4 The reduction at the reference microphone; constant speed

In a first series of experiments the reduction at constant speed is measured. For each driving condition 157 blocks of acquired data are analysed with a synchronized sampling frequency. Each block of 840 samples covers exactly 24 periods of the engine revolution frequency.
In the first experiment the van is driven on a secondary road at 50 km/h (4^{th} gear) and the pressure level is measured with the reference microphone. After a short while the active noise control system is switched on and the measurement is repeated. The revolution frequency of the engine at 50 km/h in the 4^{th} gear is 40 Hz (2400 rpm), giving a firing frequency of 100 Hz. The 157 blocks of data cover 94 seconds. In figure 5.2.9 two sequences of order spectra of the pressure level (linear average of two spectra) are shown. The 157 blocks depicted in the upper figure are measured without anti-noise, the 157 blocks in the lower figure are measured with anti-noise on the engine harmonics number 2, 2.5 (firing frequency) and 4. The level at the firing frequency is prominent in the first 157 spectra. During ANC the pressure level at all three harmonics is almost completely reduced to the noise level of the surrounding frequencies in the entire sequence. It is important to note that the algorithm is not influenced by a sudden increase of extraneous noise caused by a bump in the road (for instance at block number 65). Furthermore, no additional noise at other frequencies is generated by the active noise control system, only the three harmonics are reduced.
The sequences of 157 spectra are averaged yielding a spectrum for the situation without anti-noise and a spectrum for the situation with anti-noise. In figure 5.2.10 the two spectra are plotted: a dotted line for the situation without anti-noise and a solid line for the situation with ant-noise. The pressure level at the firing frequency is reduced by well over 20 dB.

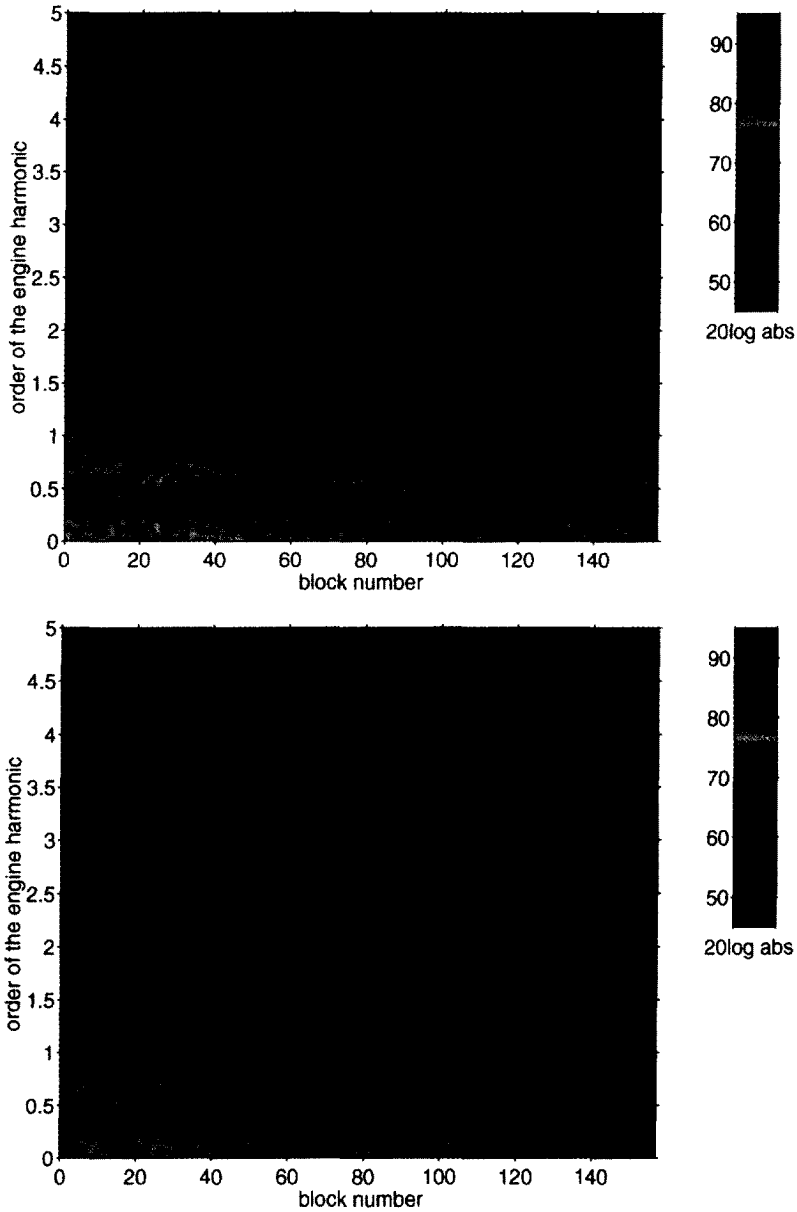

Figure 5.2.9 ; *The order spectra of 157 data blocks measured (gap-free) at the reference microphone at 50 km/h (4th gear). In the upper figure the situation without anti-noise is plotted, in the lower figure the situation with anti-noise is shown.*

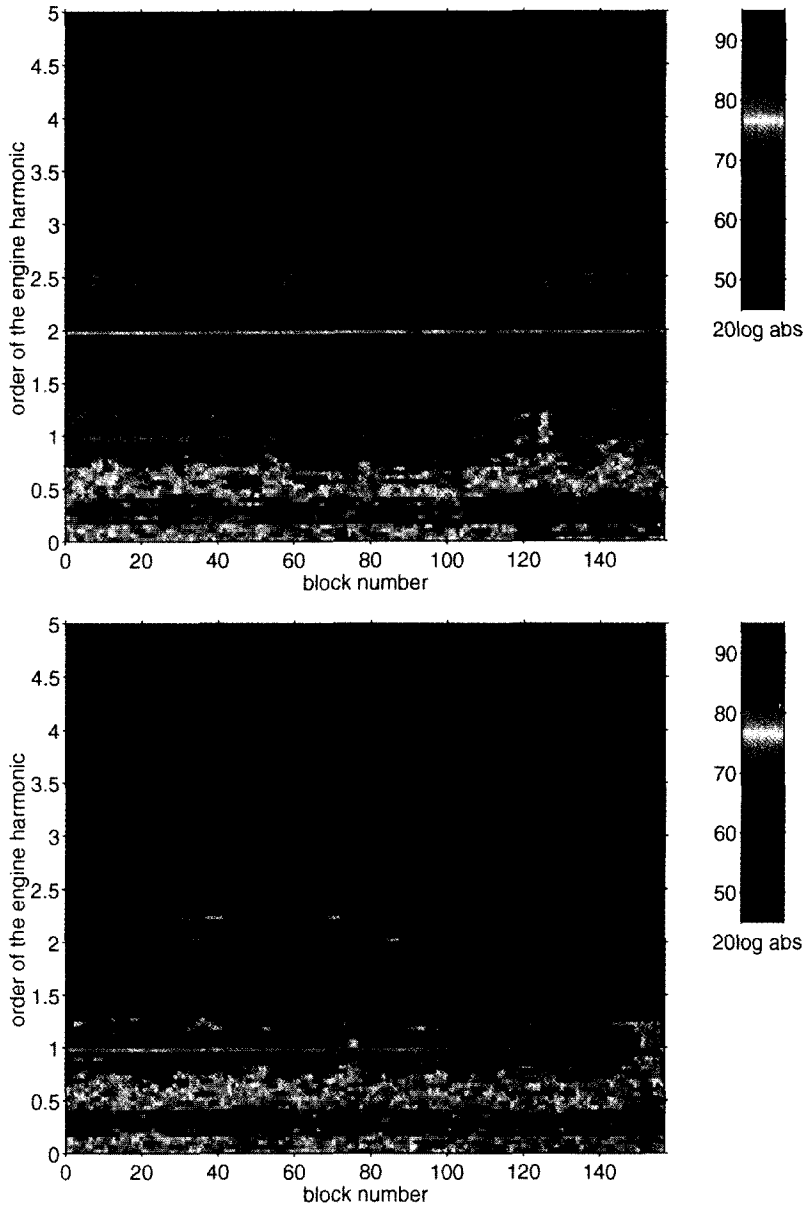

Figure 5.2.11 ; *The order spectra of 157 data blocks measured (gap-free) at the reference microphone at 70 km/h (5th gear). In the upper figure the situation without anti-noise is depicted, in the lower figure the situation with anti-noise is plotted.*

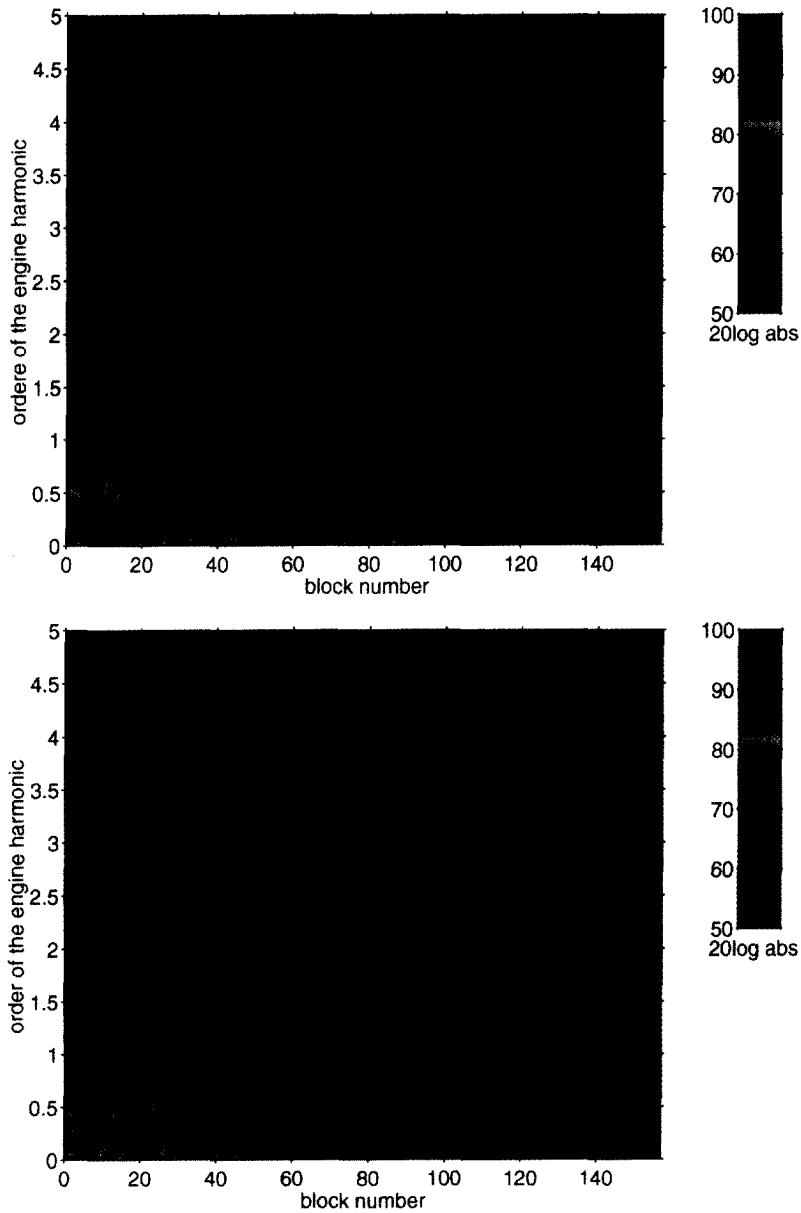

Figure 5.2.13 ; *The order spectra of 157 data blocks measured (gap-free) at the reference microphone at 110 km/h (5th gear). In the upper figure the situation without anti-noise is plotted, in the lower figure the situation with anti-noise is shown.*

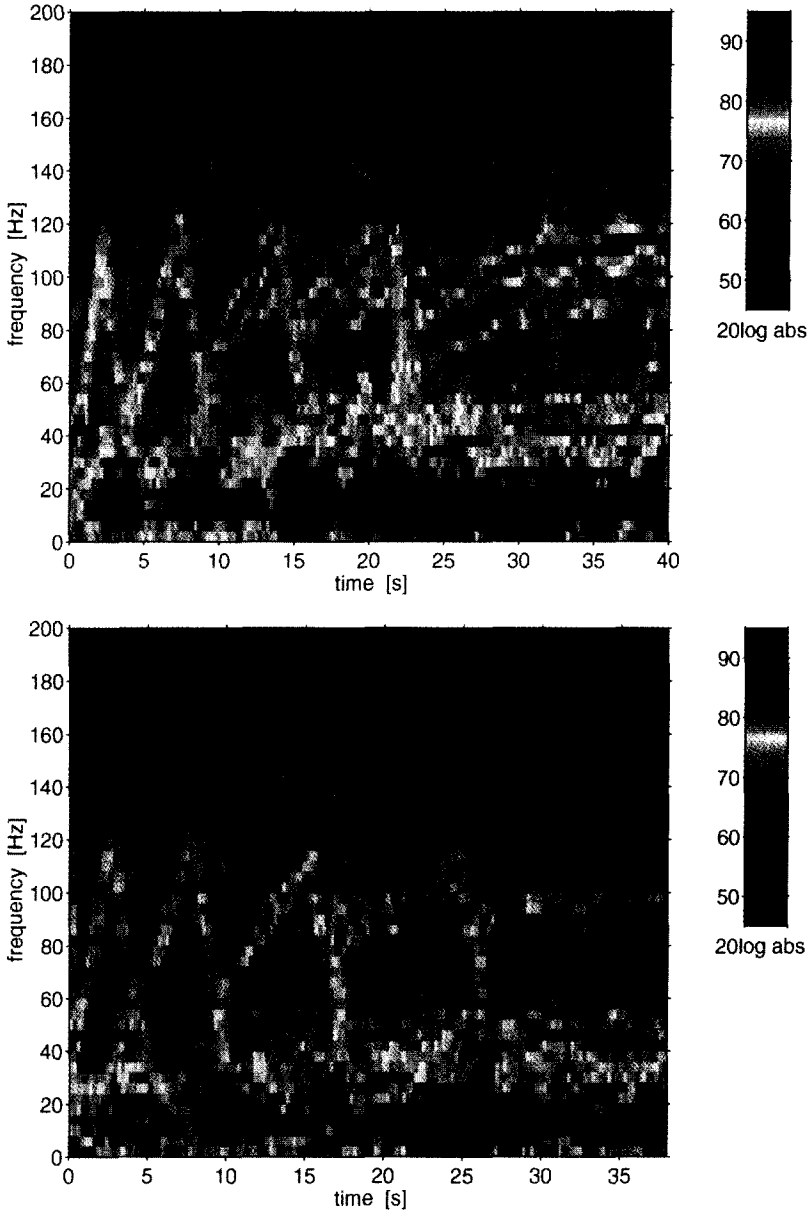

Figure 5.2.15 ; *The frequency spectra of 210 data blocks measured (gap-free) at the reference microphone during acceleration from 0 to 70 km/h with changing gears. In the upper figure the situation without anti-noise is plotted, in the lower figure the situation with anti-noise is shown*

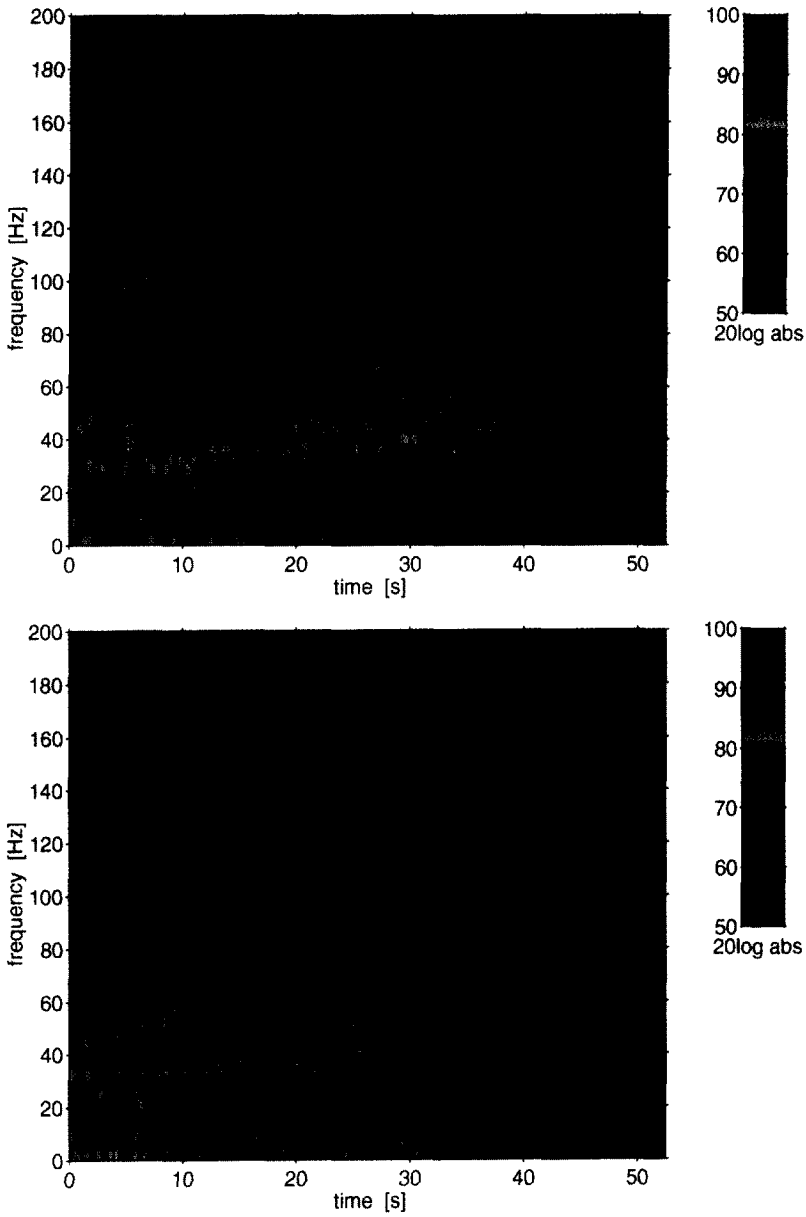

Figure 5.2.17 ; *The frequency spectra of 210 data blocks measured at the reference microphone during acceleration from 70 km/h to 110 km/h and deceleration from 110 km/h to70 km/h (5th gear). In the upper figure the situation without anti-noise is plotted, in the lower figure the situation with anti-noise is shown.*

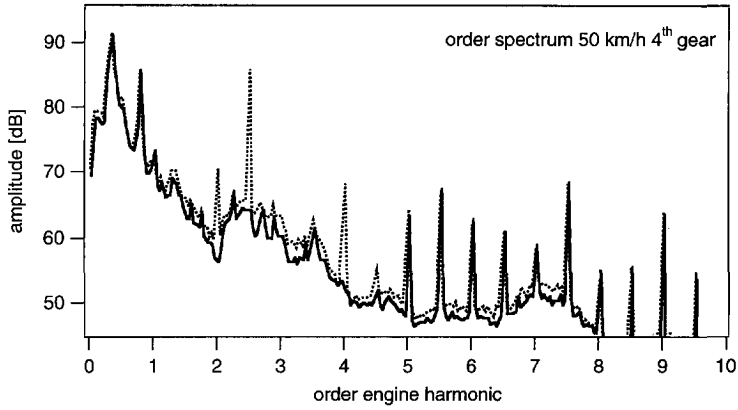

Figure 5.2.10 ; *The averaged level at the reference microphone with (solid line) and without (dotted line) active noise control at 50 km/h (2400 rpm).*

On another stretch of secondary road the pressure level is measured in the two situations (no ANC and ANC) at 70 km/h (5th gear). The revolution frequency at 70 km/h in the 5th gear is 43 Hz (2600 rpm), giving a firing frequency of 108 Hz. Active noise control is applied to the engine orders 2, 2.5 (firing frequency), and 4. In figure 5.2.11 the sequence of 157 order spectra without anti-noise is shown in the upper figure (already shown in figure 5.2.4) whereas in the lower figure the sequence of order spectra with anti-noise is depicted. Each sequence covers 87 seconds. During ANC the levels of the firing frequency and the level of the 4th harmonic are completely reduced to the noise level in all blocks. Apparently the 2nd harmonic is only partly reduced.

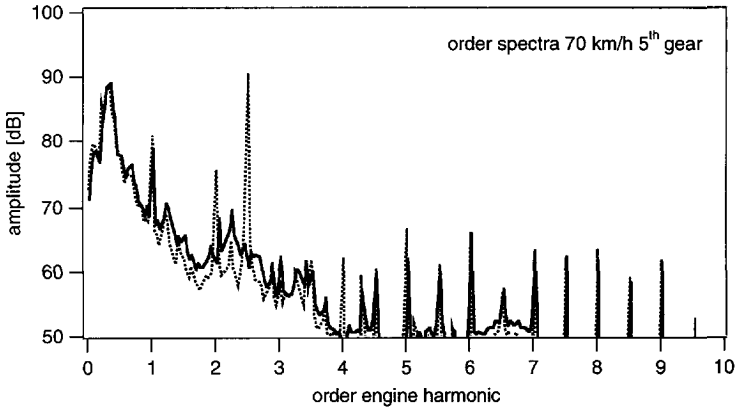

Figure 5.2.12 ; *The averaged level at the reference microphone with (solid line) and without (dotted line) active noise control at 70 km/h (2600 rpm).*

The two sequences of spectra are averaged and the result is shown in figure 5.2.12. Clearly the level at the frequencies around the second engine harmonic is higher during the ANC measurements. The level at the second harmonic itself is reduced by about 10 dB. The reduction of the pressure level at the firing frequency is nearly 30 dB.

The same type of figures are produced for the results of measurements at 110 km/h on a highway. At 110 km/h (5^{th} gear) the engine revolution frequency is 68 Hz, and in figure 5.2.13 the two sequences (averaged over 2 blocks) without and with anti-noise are depicted. Anti-noise is applied to the engine orders 1, 1.5, 2 and 2.5. In stead of the the level at the firing frequency at 170 Hz, the level at the second engine order at 136 Hz is prominent in the spectrum. The level at the firing frequency hardly rises above the noise level. During ANC the pressure levels at the engine revolution frequency and at the firing frequency are reduced to the level of the surrounding frequencies. The pressure level at the second engine harmonic is largely reduced, but not completely. Apparently, there are too many dominant eigenmodes. However, note that the ANC system reduces noise exactly at the harmonics and that the second engine harmonic is close to a strong resonance of the engine in its suspension. Resonances excited by a bump in the road (block 135 for example) ar not reduced by the system.
In this experiment ANC is applied deliberately to the engine harmonic 1.5, a harmonic which cannot be distinguished in the non periodic noise between the engine revolution frequency and the second harmonic. The algorithm is not bothered by the high noise level and there even seems to be a very slight reduction, as can be seen in figure 5.2.14, in which the pressure levels averaged over 157 blocks are drawn. The level of the second engine harmonic is reduced by more than 20 dB.

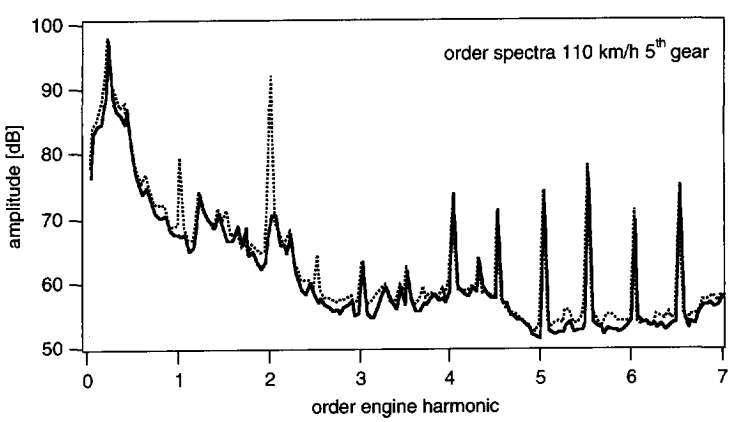

Figure 5.2.14 ; *The averaged level at the reference microphone with (solid line) and without (dotted line) active noise control at 110 km/h (4080 rpm).*

In appendix D results of measurements at 60 km/h, 80 km/h, 90 km/h and 95 km/h (all in the 5th gear) are shown.

5.2.5 The reduction at the reference microphone; acceleration and deceleration

In two series of measurements the van is accelerated. In both series the set-up described in section 5.2.3 is used, and ANC is applied to the engine orders 2, 2.5, 4 and 5 as long as they are within the frequency limits of the controller (from 38 Hz to 200 Hz).
In the first series the van is accelerated in 35 seconds from 0 to 70 km/h using all 5 gears. This series is carried out on a secondary asphalted road. In figure 5.2.15 the two sequences of frequency spectra, measured with a fixed sampling frequency of 1024 Hz are shown. The block length is 256 samples giving a frequency resolution of 4 Hz. In the upper figure (no ANC) the acceleration and the switching of the 5 gears is marked by the presence of the level of the firing frequency which is the prominent harmonic in all five gears. At the start of the sequence the firing frequency is about 30 Hz. In the first gear the firing frequency increases rapidly to 120 Hz, after which the gear is changed. In each ensuing gear the frequency increase takes more time. During acceleration in the 5th gear the second engine harmonic is visible too. In the lower sequence (with ANC) the level at the firing frequency is reduced considerably, but not completely. Due to the fast changes the algorithm cannot track the harmonic perfectly during the entire sequence. In the 5th gear the level of the 2nd harmonic is reduced completely. Taking the average over all *order* spectra, found with a synchronized sampling frequency (blocks of 840 samples), the (complete) reduction of not only the level of the 2nd harmonic but also the level of the 4th harmonic, hardly perceptible in the spectrum, is evident.
In figure 5.2.16 the average of all order spectra is shown. The averaged reduction of the level at the firing frequency during acceleration from 0 to 70 km/h is a little less than 15 dB.

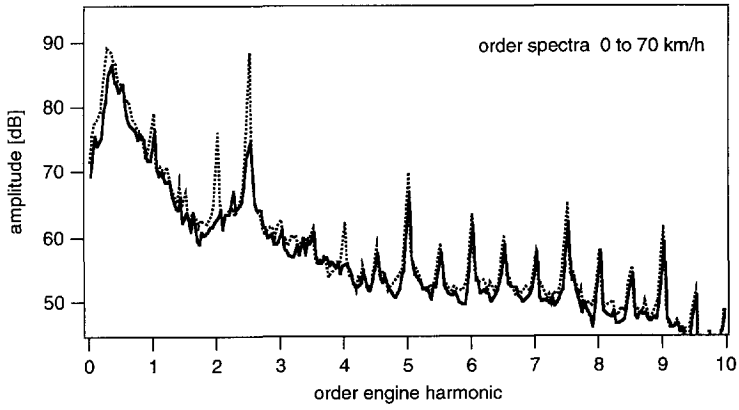

Figure 5.2.16 ; *The averaged level at the reference microphone with (solid line) and without (dotted line) active noise control during acceleration from 0 to 70 km/h.*

In the second series the van is accelerated (on a highway) from 70 km/h to 110 km/h in the 5th gear, after which the throttle pedal is released. In this series the frequency of the 4th and of the 5th harmonic is above 200 Hz in almost the entire sequence and so in fact ANC is only applied to the 2nd engine harmonic and the firing frequency (2.5). In figure 5.2.17 two sequences of 210 frequency spectra, measured with a fixed sampling frequency of 1024 Hz, are shown. The block length is 256 Hz (4 Hz resolution) and so each sequence covers 52.5 seconds. The left sequence without anti-noise was shown already in figure 5.2.6. In the right sequence the results of the measurement with anti-noise is shown. The level at the firing frequency is almost completely reduced to the level of the surrounding frequencies. Again, it appears that at 110 km/h the level of the second harmonic is not reduced completely (see section 5.2.4). In figure 5.2.18 the averaged levels are depicted. Both harmonics are reduced by more than 15 dB during the acceleration from 70 km/h to 110 km/h.

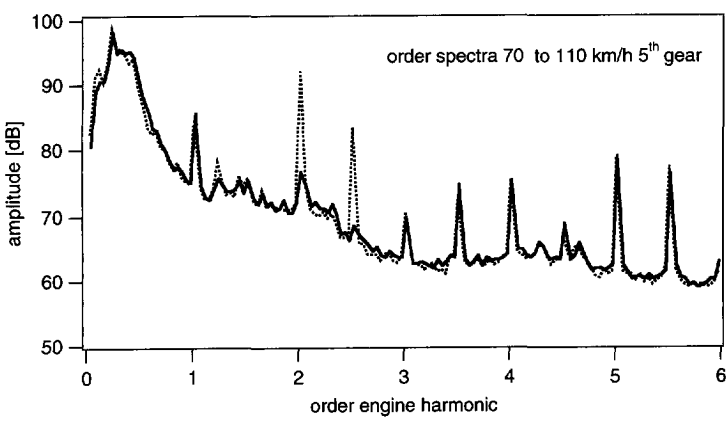

Figure 5.2.18 ; *The averaged level at the reference microphone with (solid line) and without (dotted line) active noise control during acceleration from 70 to 110 km/h.*

5.2.6 The reduction at the acoustic antenna

The wave fields are recorded in all driving conditions. However, the 64 microphone channels are stored in a sequence of 8 data blocks on 8 (parallel) channels of the recorder. Now a reasonable resolution in the engine order spectrum requires a block length for each block of 24 engine revolutions.
During acceleration (and deceleration) the engine revolution frequency shifts significantly in 192 revolutions and therefore only wave fields measured at constant driving speeds (± 2 %) are analysed. At a constant speed of 70 km/h (5th gear) the pressure level at the firing frequency (108 Hz) dominates the spectrum. At the reference microphone the level is 91 dB, and anti-noise reduces this level to about 62 dB, the level of the surrounding

frequencies (figure 5.2.12). In figures 5.19 the *wave fields* without ANC (left) and with ANC (right) at the firing frequency are shown. The position of the driver is near to the right hindmost corner, the head of the driver causes a visual dip in the left figure, which was shown already in figure 5.2.3. The steering wheel is near the right front corner of the figure. The position of the reference microphone is indicated in the figures 5.1 and 5.8a. The pressure at the firing frequency is averaged over the 64 microphones. Without anti-noise the level of the averaged pressure is 82 dB. With the 4 anti-noise loudspeakers it is reduced to 66 dB, close to the residual level on the reference microphone. This means that there are not more than 4 eigenmodes largely determining the pressure around 108 Hz, if the wave field is excited by the engine. The reduction of the averaged pressure is not as large as the reduction of the pressure at the reference microphone, mainly because the reference microphone is positioned at a pressure maximum where the difference with the general noise level is high (see figure 5.2.19). Note that the reduction of the pressure at the position of the driver is almost 30 dB, whereas the reduction at the position of the passenger is very small.

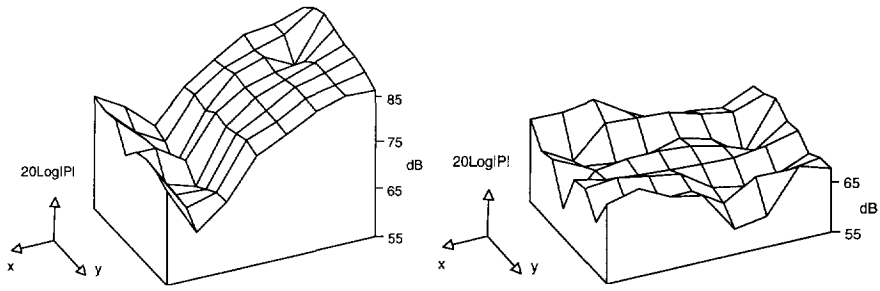

Figure 5.2.19 ; *The wave field at the firing frequency at 70 km/h; left: without ANC and right with ANC.*

The 2nd engine harmonic at 70 km/h has a frequency of approximately 88 Hz. In figure 5.20 the wave fields at this harmonic the are shown (on the left no ANC and on the right with ANC). The primary wave field (left) does not seem to be at resonance: no distinct maxima or minima are visual. The level of the averaged pressure without anti-noise is 74 dB and the difference with the level at the reference microphone (78 dB) is smaller than at the firing frequency. The level of the averaged pressure of the residual wave field (right) is 64 dB, which is about the residual level at the reference microphone. Note that in this case at the position of both the driver and the passenger the reduction is some 10 dB.

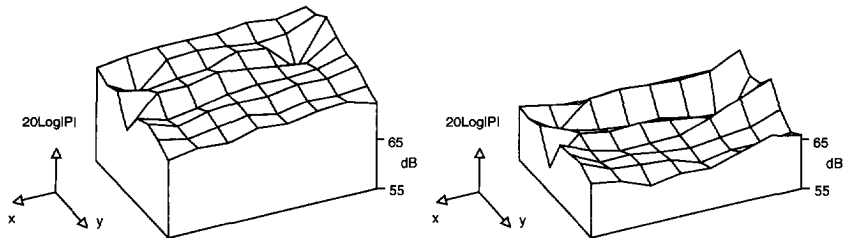

Figure 5.2.20 ; *The wave field at the second engine harmonic at 70 km/h: left: without ANC and right with ANC.*

The frequency of the 2nd engine harmonic at 110 km/h is 135 Hz which is not very close to an eigenfrequency. In figure 5.2.21 the wave fields are shown (on the left without ANC and on the right with ANC). Without ANC the level of the averaged pressure at the 2nd harmonic is 88 dB, while at the reference microphone a level of 92 dB is found (figure 5.2.14). The level of the averaged residual pressure is 81 dB, which is well over the residual level of 71 dB at the reference microphone. So, it seems that at 135 Hz the 4 anti-noise loudspeakers are not able to reduce the averaged pressure level of the wave field to the general noise level. Apparently there are more than 4 dominant eigenmodes determining wave field around 135 Hz.

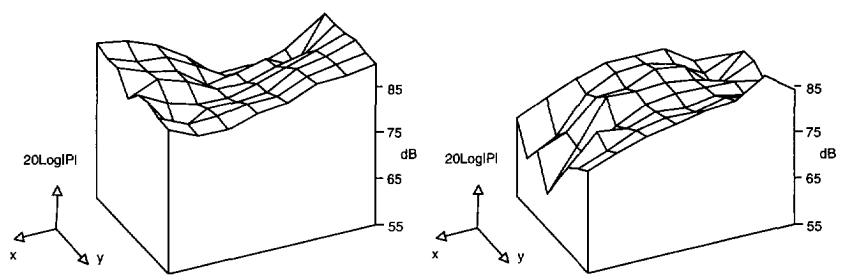

Figure 5.2.21 ; *The wave field at the second engine harmonic at 110 km/h: left: without ANC and right with ANC..*

According to figure 5.2.2 the wave field is in resonance at 142 Hz. This would mean that there is only one eigenmode that is largely determining the acoustic pressure. The firing frequency at a constant speed of 90 km/h is about 142 Hz. In figure 5.2.22 the wave field at the firing frequency, measured at 90 km/h, is shown. Clearly the wave field is almost in resonance. At the reference microphone the level at the firing frequency is just over 80 dB. The level of the averaged pressure is 77 dB. This level is reduced with anti-noise to 65 dB, which is again close to the residual level at the reference microphone (62 dB). So the averaged reduction is higher at 142 Hz than at 135 Hz which means that the number of dominant eigenmodes is smaller.

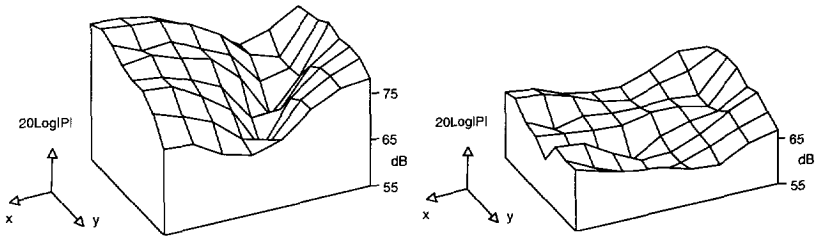

Figure 5.2.22 ; *The wave field at the firing frequency at 90 km/h: left: without ANC and right with ANC.*

5.3 Conclusions

The results of the experiments in the chemical plant show that the block based Fourier controller algorithms are capable to find the correct transfer functions and are able to calculate the proper anti-noise signal in the circumstances of the vacuum pump. Furthermore, the ANC system reduces the harmonics of acoustic pressure (apart from the 3rd harmonic of 4004) on the error microphone to the level of the surrounding frequencies.
In the initial situation, before the fall-pipes are modified, the periodic noise in the filter building is largely determined by the noise coming out of the outlets of the pumps. After the modification, in which the two outlets are connected to one fall-pipe, the periodic noise in the filter building is mainly caused by other sources (radiation of the pump itself and the ducts). So, in spite of the fact that the anti-noise system works properly, there is no considerable reduction in the building.

According to the derivations and experiments in chapter 4, an ANC system with a sample based Fourier controller is able to reduce several harmonics without instability problems whereas the eigenvalue spread is optimal. In the delivery van the primary signal is characterized by many harmonics and relatively fast changes in the fundamental frequency of the periodic noise. Moreover, the primary noise is corrupted by sudden increases of the extraneous noise due to bumps in the road on which the van is driven. The experiments in the delivery van show that the sample based Fourier controller gives a substantial reduction on several harmonic components in all driving conditions and is not bothered by those circumstances.
The results of the measurements with the acoustic antenna show that the reduction is not restricted to the error microphones but is achieved at other positions in the interior as well.

Appendix A

Section 2.1 Basic equations

Potential energy

The potential energy can be derived using the powerflow through a closed surface:

$$w = \oint_S p\vec{v}.\vec{n}dS. \tag{A.1}$$

Now the first theorem of Green reads

$$\int_V \left(f\nabla^2 g + \nabla f.\nabla g\right)dV = \oint_S f\nabla g.\vec{n}dS. \tag{A.2}$$

The pressure p is substituted in **f** and the velocity $\vec{v}$ is substituted in the divergence of **g**:

$$p = f, \quad \vec{v} = \nabla g, \tag{A.3}$$

so combination of (A.2), (A.3) and the basic equations (2.1.1) to (2.1.2) without sources (q=0 and $\vec{f} = \vec{0}$) yields

$$w = \oint_S p\vec{v}.\vec{n}dS = -\frac{\partial}{\partial t}\int_V \left[\frac{p^2}{2\rho_s c^2} + \frac{1}{2}\rho_s \vec{v}.\vec{v}\right]dV. \tag{A.4}$$

The time averaged potential energy of a periodic time function having period T can be written as a superposition of the fourier coefficients using a Fourier series:

$$p_p(\mathbf{x},t) = \frac{1}{T}\sum_{n=-\infty}^{\infty} P(\mathbf{x},n\Delta f)\exp(j2\pi n\Delta f t), \tag{A.5}$$

and $\Delta f = 1/T$. The time averaged quadratic time function can be written as

$$\frac{1}{T}\int_0^T p_p^2(\mathbf{x},t)dt = \frac{1}{T}\int_0^T \left[\frac{1}{T}\sum_{n=-\infty}^{\infty} P(\mathbf{x},n\Delta f)\exp(j2\pi n\Delta f t)\right]^2 dt. \tag{A.6}$$

Using orthogonality

$$\frac{1}{T}\int_0^T \exp(j2\pi n\Delta f t)\exp(-j2\pi m\Delta f t)dt = \begin{matrix} 1 \text{ if } n = m \\ 0 \text{ if } n \neq m \end{matrix}, \tag{A.7}$$

the right hand side of equation (A.5) reduces to

$$\frac{1}{T^2}\sum_{n=-\infty}^{+\infty}|P(\mathbf{x},n\Delta f)|^2. \qquad (A.8)$$

Section 2.2 One dimensional situation

Cutoff frequency

In a rigid walled duct of constant cross section only plane waves propagate in the x-direction at frequencies below the eigenfrequency of the first transverse eigenmode (y- or z-direction). Eigenmodes are discussed in section 3.1. Anticipating on section 3.1, the eigenvalue of the first transverse- or cross-mode in a rectangular duct is given by

$$k_{y,1}=\frac{\pi}{L_y} \quad \text{or} \quad k_{z,1}=\frac{\pi}{L_z},$$

so if $L_y < L_z$ the first cross-mode eigenfrequency, the *cutoff frequency, is* $f_c=\frac{c}{2L_z}$.

Extrapolation matrix

The extrapolation matrix derived in section 2.2 is used in the derivations of anti noise in the one dimensional situation. It has the following properties

$$\mathbf{M}(x_I-x_{III},f)=\mathbf{M}(x_I-x_{II},f)\mathbf{M}(x_{II}-x_{III},f), \qquad (A.9)$$

and

$$\mathbf{M}^*(x_I-x_{II},f)\mathbf{M}(x_I-x_{II},f)=\begin{pmatrix}1 & 0\\ 0 & 1\end{pmatrix}, \qquad (A.10)$$

and, as a consequence

$$\mathbf{M}^*(x_I-x_{II},f)=\mathbf{M}(x_{II}-x_I,f). \qquad (A.11)$$

Power flow

The power flow of frequency component f at position x is (equation (2.2.11)

$$W(x,f)=\frac{2A_d}{T^2}\mathrm{Re}\left[P^*(x,f)V(x,f)\right]=$$
$$=\frac{A_d}{T^2}\left[P^*(x,f)V(x,f)+V^*(x,f)P(x,f)\right]. \qquad (A.12)$$

The power flow can be written as a function of the power flow at a position x_o and the sources between the two position.With the help of equation (2.2.1)

$$\frac{\partial \vec{B}(x,f)}{\partial x} = \mathbf{A}\vec{B}(x,f) + \vec{S}(x,f). \qquad (A.13)$$

Now $P^*(x,f)V(x,f) + V^*(x,f)P(x,f) = \vec{B}^H(x,f)\mathbf{N}\vec{B}(x,f),$ (A.14)

in which $\mathbf{N} = \begin{pmatrix} 0 & 1 \\ 1 & 0 \end{pmatrix}$, so

$$\left[P^*(x_1,f)V(x_1,f) + V^*(x_1,f)P(x_1,f)\right] - \left[P^*(x_o,f)V(x_o,f) + V^*(x_o,f)P(x_o,f)\right] =$$

$$= \int_{x_o}^{x_1} \frac{\partial \vec{B}^H(x,f)\mathbf{N}\vec{B}(x,f)}{\partial x} dx =$$

$$= \int_{x_o}^{x_1} \left[\frac{\partial \vec{B}^H(x,f)}{\partial x}\mathbf{N}\vec{B}(x,f) + \vec{B}^H(x,f)\mathbf{N}\frac{\partial \vec{B}(x,f)}{\partial x}\right] dx \qquad (A.15)$$

Since $\mathbf{A}^H\mathbf{N} = -\mathbf{N}\mathbf{A}$, the right hand side of (A.15) can, with the help of (A.13), be rewritten to

$$\int_{x_o}^{x_1} \left[\vec{S}^H(x,f)\mathbf{N}\vec{B}(x,f) + \vec{B}^H(x,f)\mathbf{N}\vec{S}(x,f)\right] dx, \qquad (A.16)$$

and, if $\vec{S}(x,f) = \begin{bmatrix} 0 \\ Q(x,f) \end{bmatrix}$, to

$$\int_{x_o}^{x_1} \left[Q^*(x,f)P(x,f) + P^*(x,f)Q(x,f)\right] dx, \qquad (A.17)$$

so if there are only volume sources present between x and x_o

$$\mathrm{Re}\left[P^*(x,f)V(x,f)\right] = \mathrm{Re}\left[P^*(x_o,f)V(x_o,f)\right] + \int_{x_o}^{x} \mathrm{Re}\left[P^*(x',f)Q(x',f)\right] dx'. \qquad (A.18)$$

Appendix B

section 3.1

The acoustic pressure as a superposition of eigenmodes

Using Greens second theorem

$$\int_{\text{Volume}} (\Psi_m(\mathbf{x})\nabla^2\Psi_n(\mathbf{x}) - \Psi_n(\mathbf{x})\nabla^2\Psi_m(\mathbf{x}))dV =$$
$$= \oint_{\text{Surface}} (\Psi_m(\mathbf{x},f)\nabla\Psi_n(\mathbf{x},f) - \Psi_n(\mathbf{x},f)\nabla\Psi_m(\mathbf{x},f)).\vec{n}dS, \qquad \text{(B1)}$$

and Helmholtz equation (2.4.4) we find

$$\left(k_m^2 - k_n^2\right) \int_{\text{Volume}} (\Psi_m(\mathbf{x})\Psi_n(\mathbf{x}))dV =$$
$$= \oint_{\text{Surface}} (\Psi_m(\mathbf{x})\frac{\partial\Psi_n(\mathbf{x})}{\partial\vec{n}} - \Psi_n(\mathbf{x})\frac{\partial\Psi_m(\mathbf{x})}{\partial\vec{n}})dS. \qquad \text{(B2)}$$

If $\beta(\mathbf{x})$ does not depend on the eigenfunction number, the right side of equation B2 equals zero, and as a consequence

$$\int_{\text{Volume}} (\Psi_m(\mathbf{x})\Psi_n(\mathbf{x}))dV = 0, \qquad \text{(B3)}$$

if $n \neq m$.

Simple set of eigenfunctions

The eigenfunctions and eigenvalues can be found simply by considering the wave field to be a superposition of plane waves. Doing so the eigenfunctions and eigenvalues can be derived in several ways. Using a geometric presentation the mechanisms causing standing waves can be made clear. Eigenfunctions and eigenvalues are found by solving the wave equation.
Plane waves propagating in certain directions and reflecting to the walls create a standing wave if the wavelength 'fits' into the enclosure. In figure B1 an example of fitting waves is depicted in a two dimensional presentation (only the plane z=0 is shown). In this example the wave fronts are parallel to the diagonals of the plane z=0. Only two of the four possible wave fronts are drawn. The walls are supposed to be rigid (pressure reflection coefficient equals 1) causing reflection without loss or phase shift. In the example constructive interference takes place if the wavelength equals

$$\lambda = \frac{2L_xL_y}{\sqrt{L_x^2 + L_y^2}} \qquad \text{(B4)}$$

As a result a standing wave pattern will be formed in the enclosure. It can be derived that this particular standing wave has two nodal lines of the pressure at $x = \frac{1}{2}L_x$ and $y = \frac{1}{2}L_y$ (1-1-0 mode).

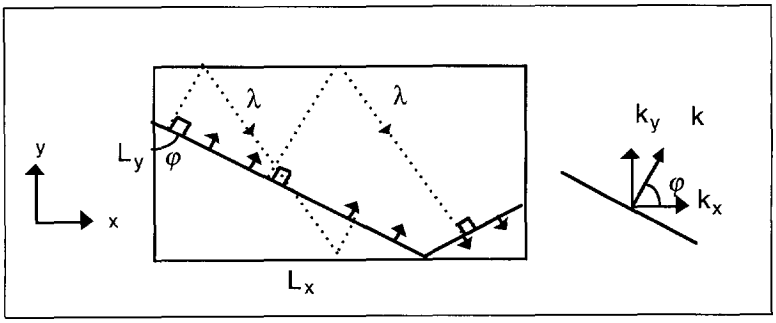

Figure B1 ; *An example of a plane wave direction causing a standing wave (parallel to a diagonal). If the wavelength equals the path-length of each of the the dashed lines (1-1-0 mode) a standing wave will be formed.*

Using the orthogonal basis x-y-z, a plane wave can be written as

$$\exp[jkr] = \exp[jk_x x]\exp[jk_y y]\exp[jk_z z], \qquad \text{(B5)}$$

where, using spherical coordinates

$$\begin{aligned} k_x &= k\sin(\theta)\cos(\varphi), \\ k_y &= k\sin(\theta)\sin(\varphi), \\ k_z &= k\cos(\theta). \end{aligned} \qquad \text{(B6)}$$

Since the wave length $\lambda = \frac{2\pi}{k}$. the values of k_x, k_y and k_z are in the 1-1-0 mode ($\theta = \frac{1}{2}\pi$, figure B1)

$$k_x = \frac{\pi}{L_x}, k_y = \frac{\pi}{L_y} \text{ and } k_z = 0$$

Obviously $k^2 = k_x^2 + k_y^2 + k_z^2$.
The total wave field describes the fourth eigenfunction, and is a superposition of the four plane waves :

$$\Psi_4(\mathbf{x}) = \exp(jk_x x)\exp(jk_y y) + \exp(-jk_x x)\exp(jk_y y) +$$
$$+\exp(jk_x x)\exp(-jk_y y) + \exp(-jk_x x)\exp(-jk_y y),$$

so

$$\Psi_4(\mathbf{x}) = 4\cos(k_x x)\cos(k_y y).$$

Of course there are many (in fact infinite) possible combinations of propagation direction and wavelength causing standing waves. They are found solving the three dimensional homogeneous wave equation. The solutions $\Psi_n(\mathbf{x})$ can be represented by a superposition of decomposed plane waves too:

$$\Psi_n(\mathbf{x}) = \Psi_{n_x}(x)\Psi_{n_y}(y)\Psi_{n_z}(z), \tag{B7}$$

where

$$\Psi_{n_x}(x) = \Psi_{n_x}^{+}\exp(-jk_{n_x}x) + \Psi_{n_x}^{-}\exp(jk_{n_x}x), \tag{B8}$$

and similar for the y and z direction.
If the pressure reflection coefficient at the walls of an enclosure is close to one, the boundary conditions reduce to

$$\frac{\partial \Psi_{n_x}(x_b)}{\partial n_b} \approx 0, \tag{B9}$$

so the particle velocity is zero at the walls. Since we assumed the box to be rectangular (dimensions L_x, L_y, L_z) a general solution of the three dimensional Helmholtz equation under the constraint of the boundary conditions is

$$\Psi_n(\mathbf{x}) = \alpha\cos(\frac{n_x\pi x}{L_x})\cos(\frac{n_y\pi y}{L_y})\cos(\frac{n_z\pi z}{L_z}). \tag{B10}$$

The normalized eigenfunctions are found using (2.4.7)

$$\Psi_n(\mathbf{x}) = \sqrt{\frac{\varepsilon_{n_x}\varepsilon_{n_y}\varepsilon_{n_z}}{L_x L_y L_z}}\cos(\frac{n_x\pi x}{L_x})\cos(\frac{n_y\pi y}{L_y})\cos(\frac{n_z\pi z}{L_z}). \tag{B11}$$

The eigenvalues of these eigenfunctions are

$$k_n = \sqrt{\left(\frac{n_x\pi}{L_x}\right)^2 + \left(\frac{n_y\pi}{L_y}\right)^2 + \left(\frac{n_z\pi}{L_z}\right)^2}. \tag{B12}$$

The eigenvalues can be visualized using the eigenvector space. The eigenvalues k_n (equation B12) are equal to the length of the vectors from O (x=0,y=0,z=0) to a grid

point, as depicted in figure B2. In figure B2 the eigenvalue of the 2-3-1 mode is drawn. The modal density as a function of the frequency (or the wave number) is defined as the number of eigenvalues in a given interval around a wave number. In the eigenvector space the wave number-interval is an interval of vector lengths so the modal density in eigenvector space is the number of eigenvectors in a spherical shell with a thickness equal to the interval. As will be obvious the modal density increases quadratically when the wave number increases.

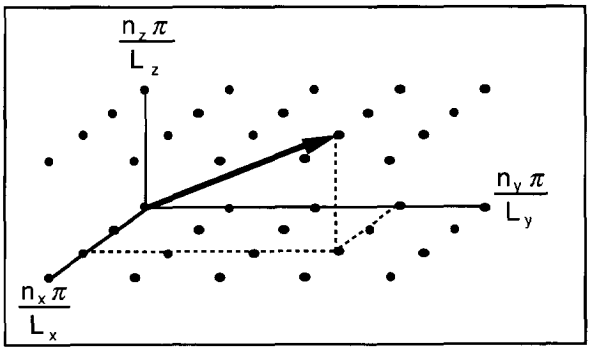

Figure B2 ; *The eigenvalue k_{342} in its vector-space (2-3-1 mode).*

The modal density can be visualized considering the occurrence of an eigenfrequency on the frequency axis. The occurrence of an eigenfrequency in an enclosure with dimensions 1.00m x 0,85m. x 0.33 m is calculated using B12 and depicted in figure B3. The density of eigenfrequencies increases with the frequency.

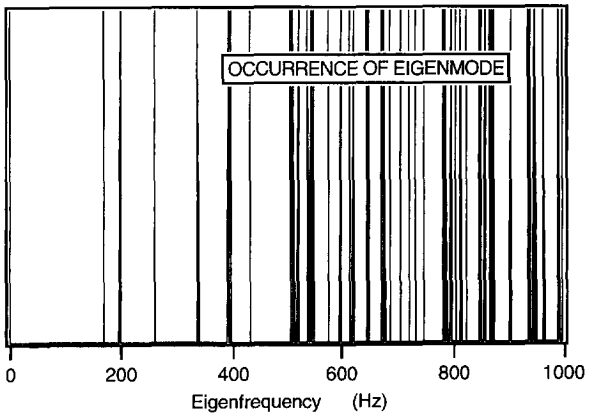

Figure B3 ; *The occurrence of eigenfrequencies in an enclosure with dimensions 1.00x0.85x0.33 m.*

Number of eigenmodes

The pressure reflection coefficient in the box of compressed wood is close to one, but not equal to one. As a result the measured eigenfrequencies will deviate from the theoretical derived eigenfrequencies. In Table I 10 synthetic eigenfrequencies, calculated with the help of equation B12 and 10 eigenfrequencies measured in the enclosure are collected in a table.

TABLE I

	n_x	n_y	n_z	theoretical	measured
1.	0	0	0	0 Hz	0 Hz
2.	1	0	0	170 Hz	179 Hz
3.	0	1	0	200 Hz	205 Hz
4.	1	1	0	263 Hz	269 Hz
5.	2	0	0	340 Hz	352 Hz
6.	2	1	0	395 Hz	413 Hz
7.	0	2	0	400 Hz	419 Hz
8.	1	2	0	435 Hz	454 Hz
9.	3	0	0	510 Hz	518 Hz
10.	0	0	1	515 Hz	530 Hz

Table B1 Theoretical and measured values of the eigenfrequencies.

section 3.2

Vector and matrix notation

The M pressures on the sensors are placed in a vector :

$$\vec{P}(f) = \left[P(\mathbf{x}_1, f) \quad \ldots \quad P(\mathbf{x}_M, f)\right]^T,$$

the M eigenfunctions are written in a matrix

$$\mathbf{\Psi} = \begin{bmatrix} \vec{\Psi}(\mathbf{x}_1)^T \\ \vdots \\ \vec{\Psi}(\mathbf{x}_M)^T \end{bmatrix},$$

so for finite vector lengths

$$\vec{P}(f) = \mathbf{\Psi}\vec{a}(f) + \vec{\varepsilon}. \qquad \text{(B13)}$$

The squared length of the error vector

$$\vec{\varepsilon}^{H}\vec{\varepsilon} = \left(\vec{P}(f) - \boldsymbol{\Psi}\vec{a}_{est}(f)\right)^{H}\left(\vec{P}(f) - \boldsymbol{\Psi}\vec{a}_{est}(f)\right), \tag{B14}$$

is minimzed for $\vec{a}_{est}(f) = \left[\boldsymbol{\Psi}^{T}\boldsymbol{\Psi}\right]^{-1}\boldsymbol{\Psi}^{T}\vec{P}(f)$.

Appendix C

section 4.1

Recursive Least Squares

The least squares error solution of the parameter vector (4.1.7) can written as

$$\vec{\theta}_{c,e}(n) = -\mathbf{P}(n)\mathbf{\Phi}^{H}(n)\bar{y}_{p,e}(n). \tag{C.1}$$

According to equation (4.1.11) the recursive relation for the inverse matrix is

$$\mathbf{P}^{-1}(n) = \mathbf{P}^{-1}(n-1) + \vec{\varphi}(n)\vec{\varphi}^{H}(n). \tag{C.2}$$

Now

$$\mathbf{\Phi}^{H}(n)\bar{y}_{p,e}(n) = \mathbf{\Phi}^{H}(n-1)\bar{y}_{p,e}(n-1) + \vec{\varphi}(n)y_{p,e}(n), \tag{C.3}$$

so

$$\vec{\theta}_{c,e}(n) = -\mathbf{P}(n)\left(-\mathbf{P}^{-1}(n-1)\vec{\theta}_{c,e}(n-1) + \vec{\varphi}(n)y_{p,e}(n)\right), \tag{C.4}$$

or

$$\vec{\theta}_{c,e}(n) = \vec{\theta}_{c,e}(n-1) - \mathbf{P}(n)\vec{\varphi}(n)\left(y_{p,e}(n) + \vec{\varphi}^{H}(n)\vec{\theta}_{c,e}(n-1)\right). \tag{C.5}$$

Using equation (C.5) the least squares error solution of the controller parameter vector is found recursively.

Projection algorithm, eigenvalue spread

Assume the two normalized input vectors are $\vec{\varphi}(1) = \begin{pmatrix} a \\ b \end{pmatrix}$ and $\vec{\varphi}(2) = \begin{pmatrix} c \\ d \end{pmatrix}$,

then the eigenvalues λ of the input correlation matrix are found if the determinant of the matrix

$$\begin{pmatrix} a^2 + c^2 - \lambda & ab + cd \\ ab + cd & b^2 + d^2 - \lambda \end{pmatrix} \tag{C.6}$$

equals zero. So, using $a^2 + b^2 = 1$ and $c^2 + d^2 = 1$,

$$\lambda^2 - 2\lambda + (ad - bc)^2 = 0. \tag{C.7}$$

The eigenvalue spread is found with the help of

$$\lambda_{1,2} = 1 \pm \sqrt{1 - (ad - bc)^2}, \tag{C.8}$$

(see figure C1).

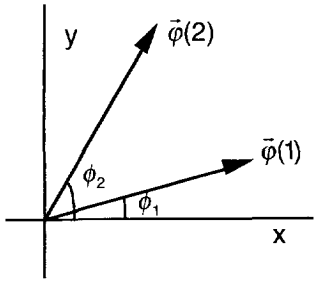

Figure C1 ; *The eigenvalue spread of the normalized correlation matrix of two vectors in 2 dimensional space is given by* $\lambda_{1,2} = 1 \pm \cos(\phi_2 - \phi_1)$.

Time-varying primary process parameters

With the help of $\Delta\vec{\theta}_c(k-1) = \vec{\theta}(k) + \vec{\theta}_c(k-1)$ the updating formula (4.1.15) can be written as

$$\Delta\vec{\theta}_c(n) = \Delta\vec{\theta}_c(n-1) - \gamma\frac{\vec{\varphi}(n)\varepsilon(n)}{\alpha + \vec{\varphi}^H(n)\vec{\varphi}(n)}, \tag{C.9}$$

so, if γ is real and $\vec{\theta}(n) \approx \vec{\theta}(n-1)$

$$\begin{aligned}\Delta\vec{\theta}_c{}^H(n)\Delta\vec{\theta}_c(n) &= \left|\Delta\vec{\theta}_c(n)\right|^2 \approx \\ &\approx \left|\Delta\vec{\theta}_c(n-1)\right|^2 + \frac{\varepsilon^2(n)}{\alpha + \vec{\varphi}^H(n)\vec{\varphi}(n)}\left[\frac{\gamma^2\vec{\varphi}^H(n)\vec{\varphi}(n)}{\alpha + \vec{\varphi}^H(n)\vec{\varphi}(n)} - 2\gamma\right].\end{aligned} \tag{C.10}$$

in which the relation $\varepsilon(n) \approx -\vec{\varphi}^H(n)\Delta\vec{\theta}_c(n-1)$ is used.
For values of $\alpha \geq 0$ and $0 < \gamma < 2$,

$$\left|\Delta\vec{\theta}_c(n)\right| - \left|\Delta\vec{\theta}_c(n-1)\right| \leq 0. \tag{C.11}$$

The minimum length of the convolution filter

Assume that the primary process can be described by a FIR filter having J elements h_j, and that the input signal is

$$\varphi(k) = \sum_{v=1}^{N} \exp(j2\pi f_v k\Delta t), \tag{C.12}$$

then

$$y_p(k) = \sum_{j=0}^{J-1} h_j \sum_{v=1}^{N} \exp(-j2\pi f_v k\Delta t). \tag{C.13}$$

Now if $J>N$

$$\varphi(k-L) = \sum_{v=1}^{N} \exp(j2\pi f_v (k-L)\Delta t)) =$$
$$= \sum_{v=1}^{N} \alpha_v \exp(j2\pi f_v (k-L+1)\Delta t)) = ... \tag{C.14}$$

in which $\alpha_v = \exp(-j2\pi f_v \Delta t)$.
So, since there are N independent variables

$$\varphi(k-N) = \sum_{i=0}^{N-1} \beta_i \varphi(k-i), \tag{C.15}$$

in which β_i is a function of $\alpha_1 \cdots \alpha_N$ which means that the process can be written as

$$y_p(k) = \sum_{j=0}^{N-1} h'_j \varphi(k-j). \tag{C.16}$$

Eigenvalue for a convolution filter length of one period

Consider the input signal (C.12), having N frequency components and a period of p samples. Since the Nyquist criterion is fulfilled, $p > 2N$. The sequential input vector has a length p, so

$$\vec{\varphi}^*(k) = \left[\varphi(k) \quad \varphi(k-1) \quad \cdots \quad \varphi(k-p+1)\right]^H$$

Using the vector

$$\Psi_v = \left[1 \quad ... \quad \exp(j2\pi f_v(-p+1)\Delta t)\right]^T, \tag{C.17}$$

the input correlation matrix after one period can be written as

$$\sum_{k=0}^{p-1} \vec{\varphi}(k)\vec{\varphi}^{H}(k) = p\sum_{v=1}^{N} \Psi_v \Psi_v^{H}. \qquad (C.18)$$

The vectors (C.17) are eigenvectors of the matrix (C.18) having an eigenvalue p^2:

$$p\left[\sum_{v=1}^{N} \Psi_v \Psi_v^{H}\right]\Psi_\kappa = p\sum_{v=1}^{N} \Psi_v \Psi_v^{H}\Psi_\kappa = p^2\Psi_\kappa$$

The other eigenvalues of the matrix are determined by the noise in the reference signal and are in general very small.

section 4.3

Single channel ANC, the projection algorithm for real signals

It can be derived simply that in spite of the fact that the process ouput $y_s(k)$ and the controller input $\varepsilon(k)$ are real, the projection algorithm as derived for complex signals can be used. Consider for convenience only one complex parameter θ which has to estimated adaptively. In that case the real error (equation (4.3.1)) can be written as

$$\varepsilon(k) = \begin{pmatrix} \mathrm{Re}[\varphi(k)] \\ \mathrm{Im}[\varphi(k)] \end{pmatrix}^{T} \begin{pmatrix} \mathrm{Re}[\theta] \\ \mathrm{Im}[\theta] \end{pmatrix} + \begin{pmatrix} \mathrm{Re}[r(k)] \\ \mathrm{Im}[r(k)] \end{pmatrix}^{T} \begin{pmatrix} \mathrm{Re}[\theta_c(k-1)] \\ \mathrm{Im}[\theta_c(k-1)] \end{pmatrix}. \qquad (C.19)$$

This ia an error equation in which the two parameters $\mathrm{Re}[\theta_c(k)]$ and $\mathrm{Im}[\theta_c(k)]$ have to be estimated. Using the projection algorithm, the updating algorithm becomes

$$\begin{pmatrix} \mathrm{Re}[\theta_c(k)] \\ \mathrm{Im}[\theta_c(k)] \end{pmatrix} = \begin{pmatrix} \mathrm{Re}[\theta_c(k-1)] \\ \mathrm{Im}[\theta_c(k-1)] \end{pmatrix} - \gamma \frac{\begin{pmatrix} \mathrm{Re}[r(k)] \\ \mathrm{Im}[r(k)] \end{pmatrix}\varepsilon(k)}{\alpha + \mathrm{Re}[r(k)]^2 + \mathrm{Im}[r(k)]^2}, \qquad (C.20)$$

which can be written in a complex form as $\theta_c(k) = \theta_c(k-1) - \gamma \dfrac{r(k)\varepsilon(k)}{\alpha + r^{*}(k)r(k)}$.

Appendix D

Additional measurements have been carried out at a constant speed of 60 km/h, 80 km/h, 90 km/h and 95 km/h (all in the 5th gear). The order spectra, averaged over 157 blocks will be presented in this appendix. In figure D.1 the speed is 60 km/h (2300 rpm), and ANC is applied to the engine orders 2, 2.5, 4 and 4.5.

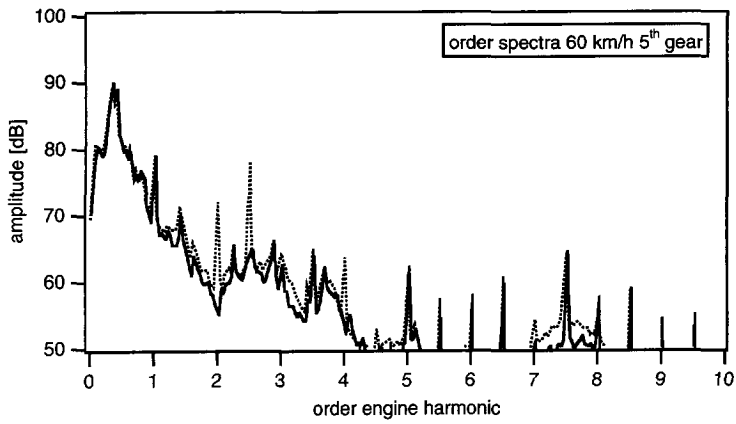

Figure D.1 ; *The averaged level at the reference microphone with (solid line) and without (dotted line) active noise control at 60 km/h (2300 rpm).*

In figure D.2 the speed is 80 km/h (3000 rpm), and ANC is applied to the engine orders 2 and 2.5.

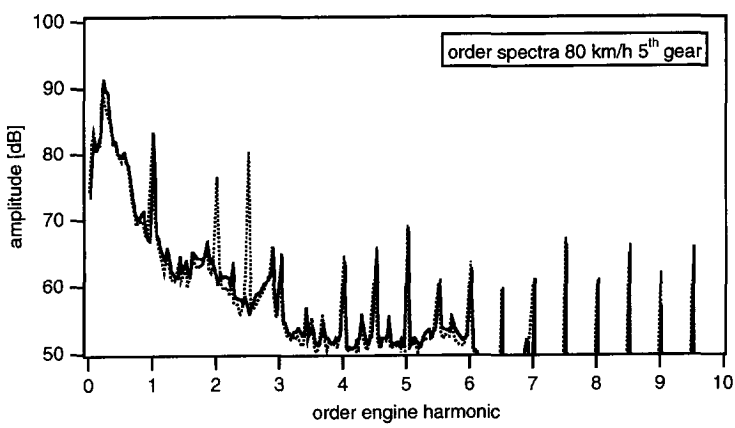

Figure D.2 ; *The averaged level at the reference microphone with (solid line) and without (dotted line) active noise control at 80 km/h (3000 rpm).*

In figure D.3 the speed is 90 km/h (3420 rpm), and ANC is applied to the engine orders 2, 2.5 and 3..

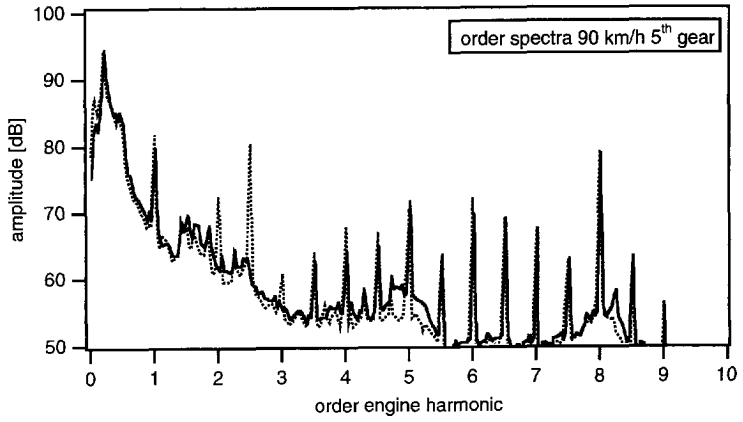

Figure D.3 ; *The averaged level at the reference microphone with (solid line) and without (dotted line) active noise control at 90 km/h (3420 rpm).*

In figure D.4 the speed is 95 km/h (3660 rpm), and ANC is applied to the engine orders 2, 2.5 and 3..

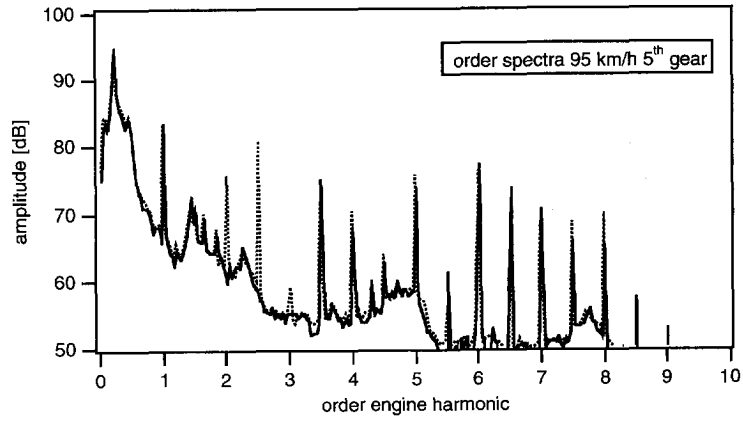

Figure D.4 ; *The averaged level at the reference microphone with (solid line) and without (dotted line) active noise control at 95 km/h (3660 rpm).*

References

[1] Rayleigh, J.W.S. [1945]. *The theory of sound, volume II* [282] (second revised and enlarged version of 1896), Dover Publications, Inc.

[2] Nelson P.A. and S.J. Elliott [1992]. *Active control of sound*, Academic press London

[3] Berkhout, A.J. [1987]. *Applied seismic wave theory,* Elsevier Science Publishers B.V. Amsterdam.

[4] Skudrzyk, E. [1954]. *Die Grundlagen der Akustik*, Springer Verlag Wien.

[5] Wapenaar, C.P.A. and A.J. Berkhout [1989]. *Elastic wave field extrapolation*, Elsevier Science Publishers B.V. Amsterdam.

[6] Morse, P.M. [1948]. *Vibration and sound*, McGraw-Hill New York

[7] Nelson, P.A., A.R.D. Curtis, S.J. Elliott and A.J. Bullmore [1987]. *The active minimization of harmonic enclosed sound fields, Part I: Theory.*Journal of Sound and Vibration **117** (1), 1-13.

[8] Bullmore, A.J., P.A. Nelson, A.R.D. Curtis and S.J.Elliott [1987]. *The active minimization of harmonic enclosed sound fields, Part II: A computer simulation.*Journal of Sound and Vibration **117** (1), 15-33.

[9] Elliott, S.J., A.R.D Curtis, A.J. Bullmore and P.A. Nelson [1987]. *The active minimization of harmonic enclosed sound fields, Part III: Experimental verification.*Journal of Sound and Vibration **117** (1), 35-58.

[10] Widrow, B. et al. [1975]. *Adaptive noise cancelling: Principles and Application.* Proc. IEEE, **63** , 1672-1716.

[11] Glover, J.R. Jr. [1975].*Adaptive noise cancelling of sinusoidal interferences.* Ph.D. dissertation Stanford University, Stanford California

[12] Elliott, S.J., I.M. Stithers and P.A Nelson [1985]. *A multiple error LMS algorithm and its application to the active control of sound and vibration.* IEEE Transactions on Acoustics, Speech, and Signal Processing **35** (10), 1423-1434

[13] Sievers, L.A and A.H. Flotow [1992]. *Comparison and extensions of control*

methods for narrow-band disturbance rejection. IEEE Transactions on Signal Processing **40** (10), 2377-2391.

[14] Widrow, B. and S.D.Stearns [1985]. *Adaptive signal processing,* Prentice-Hall, Inc. Englewood Cliffs, N.J.

[15] Astrom, K.J. and B. Wittenmark [1989]. *Adaptive control,* Adddison-Wesley Publishing Company

[16] Haykin, S. [1986]. *Adaptive filter theory,* Prentice-Hall, Inc. Englewood Cliffs, N.J.

[17] Noble, B. and J.W.Daniel [1988]. *Applied linear algebra,* Prentice-Hall, Inc. Englewood Cliffs, N.J.

[18] Eriksson, L.J. and M.C. Allie. [1989]. *The use of random noise for on-line transducer modeling in an adaptive attenuation system.* Journal of the Acoustical Society of America, **85**, 797-802

[19] van Overbeek, M.W.R.M. [1991]. *A method to identify the secondary path in active noise control systems.*Proc. Recent Advances in Active Control of Sound and Vibration, Virginia Polytechnic Institute and State University, Blacksburg Virginia

[20] Elliott, S.J. et al. [1988]. *The active control of engine noise inside cars.* Proc. Internoise 1988 (2), 987-990

[21] van Overbeek, M.W.R.M. and N.J. Doelman [1991]. *Active reduction of low frequency noise in a car interior using feedforward and feedback control.* Controle Actif Vibro-acoustique et Dynamique Stochastique, Publication du L.M.A. 127 Marseille

[22] van Overbeek, M.W.R.M.[1992]. *Active reduction of low frequency noise in vehicles.* 2nd International Conference Vehicle Comfort, Bologna Italy

[23] Hoogenboom, E. [1993]. *Parametric inversion of enclosed sound fields application to active noise control.* Thesis Lab. of Seismics and Acoustics, Delft University

Summary

Unwanted noise emitted by machinery, exhausts or whatever sources can be reduced with the help of loudspeakers radiating 'anti noise'. This way of noise reduction is called Active Noise Control (ANC) because the original, primary wave field is influenced actively. ANC is contrary to the passive ways of controlling noise for which tuned resonators, barriers and absorbing materials are used. Especially in case the noise is periodic, ANC is an excellent complement to the existing passive noise control measures. There are three principal fields of research involved in ANC: acoustics, adaptive control and hardware development. This thesis comprises the results of a research project aiming at the first two fields: acoustics and adaptive control for periodic noise.

The basic acoustics underlying anti noise are reviewed and a one-dimensional system (a duct) and a three dimensional system (an enclosure) are considered. The optimal source strength of the anti noise source in a one-dimensional situation is derived using the extrapolation matrix. The theoretical derivations are illustrated with experiments in the laboratory. The mechanisms of anti noise in a three dimensional situation (an enclosure) are described with the help of eigenmodes. The modal amplitudes of these eigenmodes are estimated, without and with anti noise, using a backward transformation on the measured acoustic pressure on 64 microphones mounted in the enclosure.

It is proposed to use adaptive control in ANC that is based on parameter estimation techniques. A comparison is made between a controller based on a polynomial model and a controller based on Fourier coefficients. Two types of 'Fourier' controllers are studied: the well known block oriented controller in which (fast) Fourier transforms are performed on blocks of data and a so-called myopic controller in which the Fourier coefficients are updated sample by sample. Both Fourier controllers are scaled in a way that the eigenvalue spread of the input correlation matrix is optimal, thus guaranteeing an optimal convergence speed. Results of experiments with the controllers in the one dimensional situation and in the three dimensional situation show that if there are several harmonic components to be reduced, the myopic controller converges much faster than the controller based on a polynomial model.

It is the aim of this research to design complete active noise control systems to be used in practice. Therefore much attention has been paid to laboratory experiments and the use of anti noise in practical applications. The applicability of anti noise in practice is successfully tested in two situations. A one dimensional ANC system comprising the block based Fourier controller is applied to periodic noise generated by a 100 kWatt vacuum pump installed in a chemical plant. Furthermore, a three dimensional ANC system comprising the sample based Fourier controller is applied to periodic noise in the cabin of a delivery van.

Samenvatting

Lawaai wat geproduceerd wordt door machines, uitlaten of wat voor bronnen dan ook, kan worden gereduceerd met behulp van luidsprekers die 'anti geluid' genereren. Deze wijze van geluidreduktie wordt wel aktieve geluidreduktie genoemd omdat het originele, primaire golfveld aktief wordt beinvloedt. Aktieve geluidreduktie is wat dat betreft tegengesteld aan passieve geluidbeheersing, waarbij $\frac{1}{4}\lambda$ dempers, geluidwallen en absorberende materialen wordt gebruikt. Anti geluid is speciaal voor periodiek lawaai een uitstekende aanvulling voor passieve lawaaibeheersing. Er zijn drie hoofdrichtingen in anti geluid onderzoek aan te geven: akoestiek, adaptieve regeltechniek en systeemontwikkeling. Deze dissertatie bevat de resultaten van een onderzoeksproject gericht op de eerste twee gebieden: akoestiek en adaptieve regeltechniek.

Er wordt een kort overzicht gegeven van de grondbeginselen van de akoestiek en een één dimensionaal systeem (een pijp) en een drie dimensionaal systeem (een omsloten ruimte) worden besproken. De optimale bronsterkte van de anti geluidbron in het één dimensionaal systeem is afgeleid met gebruikmaking van de extrapolatie matrix. De theoretische afleidingen worden geillustreerd met experimenten in het laboratorium. De mechanismen van anti geluid in het drie dimensionale systeem (een omsloten ruimte) worden beschreven met behulp van eigenmodes. De modale amplitudes van de eigenmodes zijn geschat, met en zonder anti geluid, uitgaande van de geluiddruk gemeten op 64 microfoons in de omsloten ruimte.

De adapieve regeltechniek die wordt toegepast, is gebaseerd op een parameter schattings methode. Een regelaar gebaseerd op een polynoommodel en een regelaar gebaseerd op Fourier coefficienten worden vergeleken. Twee soorten 'Fourier'regelaars zijn bestudeerd: een welbekende regelaar waarin een Fourier transformatie wordt toegepast op blokken data en een regelaar waarin de Fourier coefficienten bemonsterpunt voor bemonsterpunt worden aangepast. Beide Fourier regelaars worden zodanig geschaald dat de convergentiesnelheid van het algorithme optimaal is.

Het was de bedoeling dat het onderzoek een compleet anti geluid systeem op zou leveren. Daarom is er veel aandacht besteed aan laboratorium- en praktijkexperimenten. De toepasbaarheid van anti geluid is met goed resultaat getest in twee situaties. Een één dimensionaal anti geluid systeem, waarvan het algorithme is gebaseerd op een Fourier transformatie voor blokken data, is toegepast op periodiek lawaai afkomstig van een vacuum pomp in een chemische fabriek. Een drie dimensionaal systeem, waarin het algorithme is gebaseerd op de Fourier regelaar die punt voor punt de componenten aanpast, is toegepast op periodiek lawaai in een bestelbus.